X-ray study of the boundary layer of dwarf novae in optical quiescent state

by

Nozomi Nakaniwa

Department of Physics, Tokyo Metropolitan University
1-1 Minami-Osawa, Hachioji-shi, Tokyo, Japan 192-0397

ABSTRACT

This study aims to elucidate the physical state of the boundary layer by systematically analyzing X-ray data of dwarf novae in optical quiescent states. The dwarf nova is a semi-detached binary system consisting of the non-magnetic white dwarf and a late-type main-sequence star (secondary). Around the white dwarf is formed an accretion disk composed of the gas transferred from the secondary. When thermal instability occurs in the disk, the gas accretes rapidly to the white dwarf and an optical outburst occurs. If the white dwarf rotates much more slowly than the Keplerian velocity on its surface, the accreting matter is heated by high friction between the inner accretion disk and the white dwarf surface. This region is referred to as the boundary layer and emits X-rays. We analyzed the X-ray spectra of 19 dwarf novae in the optical quiescent state observed by the *XMM-Newton* satellite. The X-ray spectra of quiescent dwarf nova are moderately well represented by the multi-temperature thermal plasma emission model. We evaluated the spectra by adding the reflection component of the plasma from the disk and white dwarf surface and a 6.4 keV fluorescent iron emission line to this model. As a result, we discovered a clear correlation between the mass accretion rate through the boundary layer and the orbital period. The boundary layer mass accretion rate was found smaller than that in the accretion disk roughly by an order of magnitude. We also discovered a clear correlation between the maximum temperature of the plasma and the white dwarf mass. The maximum temperature is about 60% of that expected from the radial flow strong shock on the white dwarf surface.

To understand the time evolution of the boundary layer X-ray emission mechanism in the optically-quiescent phase, we used data from the SU UMa-type dwarf nova VW Hyi observed by the X-ray astronomy satellites *XMM-Newton* and *Suzaku*. The SU UMa-type dwarf nova shows not only the normal outburst but also a super-outburst, which is brighter in the optical band than the normal outburst by ~ 1 mag at its peak, and lasts about 5 times longer than the normal outburst. We evaluated the behavior of the boundary layer in terms of the number of days elapsed since the last super-outburst or the last outburst. As a result, although there was no clear trend as a function of time since the last super-outburst, the mass accretion rate showed a clear declining trend with time since the last outburst. The rate of decline is about -2.2% d^{-1}. A similar analysis on SS Cyg observed by *XMM-Newton*, *Suzaku*, and *NICER* results in a similar declining rate of the mass accretion rate of -2.6 to -1.2% d^{-1}. A number of numerical

simulations of on the dwarf nova outburst predict that the accretion rate to the white dwarf during quiescence will increase with the growth of the disk. However, our observations show that mass accretion to the white dwarf decreases over time while the accretion disk accumulates gas to the outburst. We need further observation and theoretical consideration to resolve this discrepancy.

CONTENTS

LIST OF FIGURES

LIST OF TABLES

CHAPTER 1

Introduction

A Star evolves from a cloud of gas through a protostar to a main-sequence star that burns hydrogen in a stable manner. In the interior of the main-sequence star, exothermic nuclear reaction occurs to convert hydrogen to helium, forming a central core of helium and an outer shell of burning hydrogen. When the helium core undergoes gravitational contraction and releases energy, the outside of the hydrogen-burning shell expands with energy from both the core and the shell. As the gas continues to expand, the bare core of carbon and oxygen becomes a white dwarf. The white dwarf does not glow brightly because thermonuclear reaction does not occur in it. However, in a close binary system, where the main-sequence star orbits very close to the white dwarf, the gas on the surface of the main-sequence star is extracted by the gravity of the white dwarf and accretes on it. This phenomenon is called mass accretion, and this process makes the white dwarf shine brightly. The mass accretion increases the mass of the white dwarf, and when it reaches 1.4 solar masses, a Type Ia supernova explosion occurs. In most cases, the mass accretion occurs via an accretion disk that extends around the white dwarf. The gas in the accretion disk rotates around the white dwarf at the local Keplerian velocity. Since they rotate at different speeds at different radii, they are heated by the friction between neighboring gases in the radial direction and radiate blackbody emission at the local temperature. However, the accretion process, especially from the inner edge of the accretion disk to the white dwarf, is not understood completely. In this thesis, we focus on a dwarf nova, a type of cataclysmic variables, in order to understand the mass accretion process from the disk to the white dwarf.

A cataclysmic variable is characterized by large variation in brightness on a time scale of seconds to years. The variation in brightness is due to the rate of mass accretion varying with time. The dwarf nova is one of the most populated types of the cataclysmic variable. The dwarf novae are close binary systems consisting of a low magnetic white dwarf and a late-type main-sequence star. In the dwarf novae, outbursts that last from a few days to a few weeks are regularly recurring on time scales of about 10 days to decades. The enhancement of brightening is 2 to 5 magnitudes in the V-band, which is much smaller than that of a nova explosion. Since the first discovery of the dwarf nova ”U Gem” by J. R. Hind in 1855, more than 400 dwarf novae are known to the present day. However, the cause of the outburst of the dwarf novae has remained unknown for more than 100 years since the first discovery. After a long debate

since the 1970s, it is now widely accepted that the outburst is caused by the thermo-viscous instability in the outer region of the accretion disk. According to this model, there are two stable states at the outer edge of the disk: a neutral hydrogen state at a temperature of $\sim 10^3$ K and an ionized hydrogen state at a temperature of $\sim 10^4$ K. When the state of the disk shifts from a low temperature to a high temperature, the viscosity of the gas filling the disk increases and the mass accretion rate onto the white dwarf increases rapidly, which is the cause of the outburst (Smak 1984*c*, Osaki 1996, Lasota 2001).

In dwarf novae, the accretion disk reaches near the white dwarf. The rotation velocity of a white dwarf is observationally found not more than 1/3 of the Keplerian velocity on the white dwarf's surface. Therefore, there formed a boundary layer between the inner edge of the accretion disk and the surface of the white dwarf, where the gas in the disk is decelerated from the local Keplerian velocity to the rotation velocity of the white dwarf. When the Keplerian-rotating gas collides with the surface of a white dwarf, it causes much stronger frictional forces than in the disk. The temperature of the boundary layer in quiescence is 10^8 K, and the optically thin thermal plasma that emits X-rays of about 10 keV. During outburst, on the other hand, the mass accretion rate to the white dwarf increases, and the boundary layer with increased density becomes optically thick. Since the cooling efficiency is proportional to the square of the particle density, the temperature of the boundary layer decreases to 10^5 K, emitting soft X-rays and EUV bands (Pringle 1977). The first suggestion of this phase transition was obtained from a series of observations by the EXOSAT satellite (Jones and Watson 1992), and was finally established by the simultaneous optical, EUV, and X-ray observations of Wheatley et al. (2003).

The structure of the disk has been studied in visible light for many years, and there is a vast accumulation of results. On the other hand, X-rays, which are mainly emitted during quiescent state, are difficult to observe because they are absorbed by the Earth's atmosphere. Hence, the boundary layer has been less understood than in optical.. In this study, we attempted to reveal the physical condition of the boundary layer, such as the geometric structure, temperature distribution, and gas supply to the WD, using X-ray observation data of dwarf novae in the quiescent state. For this purpose, we analyze the data of dwarf novae observed by the three X-ray astronomy satellites, *XMM-Newton*, *Suzaku* and *NICER*. *XMM-Newton* has observed 19 dwarf novae with a total of 25 data in the quiescent state. By analyzing 0.5-10.0 keV X-ray data, the structure of the boundary layer is explored in a unified approach. *Suzaku* and *NICER* have observed several times the two dwarf novae VW Hyi and SS Cyg. Therefore, it is expected to make it clear the time evolution of the boundary layer during quiescence.

This thesis is organized as follows. In Chapter 2, we review the mass transfer process of binary systems and the radiative mechanisms of the dwarf novae. In Chapter 3, we introduce the X-ray emission mechanism of optically thin thermal plasmas and the models used to evaluate the X-ray spectra in order to understand the X-ray spectra observed from dwarf novae. In Chapter 4, we characterize the scientific instruments onboard the three X-ray astronomy satel-

lites. In Chapter 5, we describe the observation log of each satellite and the data reduction procedures we applied. In Chapter 6, we present the results of our analysis. In Chapter 7, we discuss correlation of physical parameters of the quiescent boundary layer based on the results of X-ray spectra evaluation, and the time variation of mass accretion rate in the boundary layer. Finally, Chapter 8 summarizes conclusions of this thesis and describes future prospects.

CHAPTER 2

Review of Dwarf Nova

Dwarf nova (DN) is a type of non-magnetic cataclysmic variables (CVs). CV is a close binary system composed of a white dwarf (primary star) and a late-type main sequence star (secondary star) (Warner 2003). When the secondary fills up its Roche lobe, matter is transferred from the secondary to the white dwarf by the strong gravitational field. Mass accretion onto the white dwarf releases a large amounts of gravitational energy. Utilizing this energy, , CVs emit electromagnetic waves ranging from infrared to X-ray wavelengths. In this chapter, we describe the mass transfer of binary systems and the radiative mechanisms of DN.

2.1 Close binary system

2.1.1 Roche Lobe geometry

In a close binary system, the primary and secondary stars orbit each other around a common center of gravity. From Kepler's third law, the orbital period is given by

$$P_{\rm orb} = \sqrt{\frac{4\pi^2 a^3}{G\,(M_1 + M_2)}} \tag{2.1a}$$

or

$$a = 3.53 \times 10^{10} \left(\frac{M_1}{M_\odot}\right) (1+q)^{1/3} P_{\rm orb}^{2/3}({\rm h}) \quad {\rm cm} \tag{2.1b}$$

where a is the length of the semi-major axis of the binary stars and M_1 and M_2 are the masses of the primary and secondary stars, respectively, q is the mass ratio M_2/M_1. Then the centrifugal force due to the rotational motion affects the gravitational field around the stars. Figure 2.1 shows the Cartesian coordinate system (x, y ,z) rotating with the binary system, with origin at the primary star, where the x-axis lies along the line connecting the two star centres, the y-axis is in the direction of orbital motion of the primary and the z-axis is perpendicular to the orbital plane. The effective potential, that is the sum of the gravitational potentials of the two stars and that of the centrifugal force, is given by Kruszewski (1966), Pringle and Wade (1985), Frank

et al. (2002) as

$$\Phi_R = -\frac{GM_1}{(x^2+y^2+z^2)^{1/2}} - \frac{GM_2}{[(x-a)^2+y^2+z^2]^{1/2}} - \frac{1}{2}\Omega_{\rm orb}^2\left[\left(x - \frac{M_2}{M_1+M_2}a\right)^2 + y^2\right], \tag{2.2}$$

where $\Omega_{\rm orb} = 2\pi/P_{\rm orb}$. From eq.2.1 and 2.2,

$$\Phi_R = \frac{GM_1}{a} F\left(\frac{x}{a}, \frac{y}{a}, \frac{z}{a}, q\right). \tag{2.3}$$

The effective equipotentials Φ_R are known as the Roche potentials. Their shape is a function only of q and their scale is determined by a. Figure 2.1 shows the shape of the equipotential contours on the orbital plane for $q = 0.4$. There are five points where the gravitational and centrifugal forces of the main star and its companion are balanced. These equilibrium positions are called Lagrangian points. The Lagrange point L_{1-3} is on the same straight line, with L_1 between the two stars, L_2 behind the less massive star, and L_3 behind the other star. Note that the L_1 is different from the center of gravity of the binary system. $L_{4,5}$ is the local maximum of Φ_R, and is in a position to form an equilateral triangle with the centers of gravity of both stars. The three dimensional equipotential surface that passes through L_1 is known as Roche lobe.

A binary system is categorized according to relative sizes of the two stars and their Roche lobes: a detached binary when both stars are within the Roche lobe, a semi-detached binary when only one of the stars contacts to its Roche lobe, and a contact binary when both stars contact and even spill out of their Roche lobes. If the secondary expands and its surface fills the Roche lobe, the mass transfer occurs to the primary via L_1. An empirical law of the radius of the lobe-filling secondary is established by Eggleton (1983) as

$$\frac{R_2}{a} = \frac{0.49q^{2/3}}{0.6q^{2/3} + \ln(1+q^{1/3})}. \tag{2.4}$$

From eq. 2.1 and 2.4, the mean density of secondary ($\bar{\rho}_2$) is given by

$$\bar{\rho}_2 = \frac{M_2}{\frac{4}{3}\pi R_2^3} = 107\ P_{\rm orb}^{-2}({\rm h}) \quad [{\rm g\cdot cm^{-3}}] \tag{2.5}$$

For $1 < P_{\rm orb} < 10$ h, Eq.2.5 shows that a typical low-density main sequence stars ($\rho \sim 1$–100 g cm^{-3} : Allen (1976)) can fill their Roche lobes. Any system with $P_{\rm orb} > 10$ h must contain an evolved secondary.

If the secondary is a low-mass main sequence star, we can use the empirical mass-radius relation by Patterson (1984),

$$\frac{R_2}{R_\odot} = 0.98\left(\frac{M_2}{M_\odot}\right) \quad 0.8 \le \frac{M_2}{M_\odot} \le 1.4 \tag{2.6a}$$

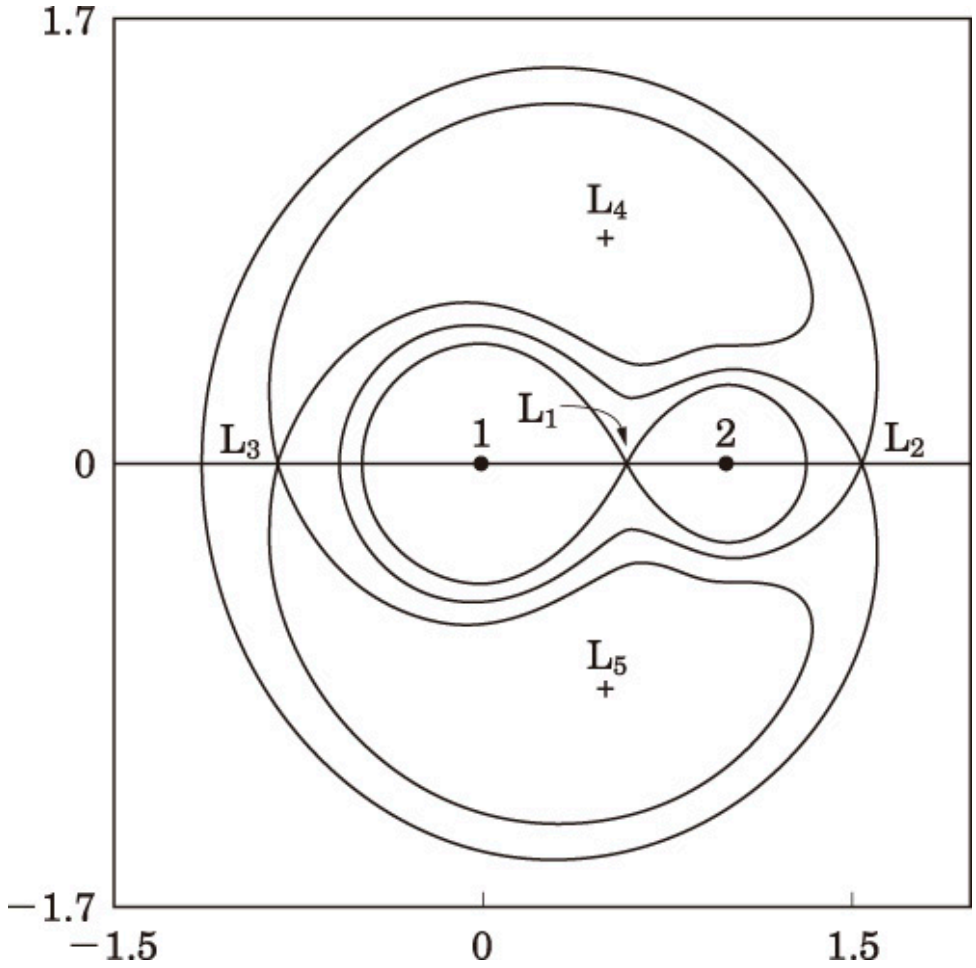

Fig. 2.1 Sections in orbital plane of Roche equipotentials for binary system with mass ratio $q = 0.4$. L_{1-5} is Lagrange points (野本 et al. 2009).

$$\frac{R_2}{R_\odot} = \left(\frac{M_2}{M_\odot}\right)^{0.88} \quad 0.1 \leq \frac{M_2}{M_\odot} \leq 0.8. \tag{2.6b}$$

Assuming that $q = 0.4$ and $M_1 = 1\ M_\odot$, eq.2.6 gives the mass and radius of the secondary as

$$M_2 = 0.07\ P_{\rm orb}^{1.22}\ M_\odot \tag{2.7}$$

$$R_2 = 0.10\ P_{\rm orb}^{1.07}\ R_\odot. \tag{2.8}$$

2.1.2 Mass-radius relation of the White Dwarf

Because the white dwarf have exhausted of nuclear fuel, its own gravity is supported by the degenerate pressure of electrons instead of thermal pressure. Until some degree of compression, the white dwarf remains stable due to non-relativistic degenerate pressure. The radius in this state can be obtained from the pressures estimated by the equation of state for non-relativistic degenerate matter and the equation of hydrostatic equilibrium, respectively (Hale 2008). The former is the pressure provided by the electrons of a certain density ρ, given by

$$P_e = \frac{1}{20}\left(\frac{3}{\pi}\right)^{2/3}\frac{h^2}{m_e}\left(\frac{\rho}{\mu_e m_p}\right)^{5/3} = 9.92\times10^6\left(\frac{\rho}{\mu_e}\right)^{5/3} \quad [\mathrm{N/m^2}]. \tag{2.9}$$

The latter provides the central pressure which is essential for the star to stabilize against gravity

$$P_c = G\frac{M^2}{R^4}. \tag{2.10}$$

If P_e and P_c are balanced, ρ is approximated to M/R^3, and $\mu_e = 2$, then

$$\frac{R}{R_\odot} \approx 0.01\left(\frac{M}{M_\odot}\right)^{-1/3}. \tag{2.11}$$

Therefore, the radius of the white dwarf is proportional to the -1/3 power of its mass. In DN, the mass gradually increases as matter accretes from the secondary star to the white dwarf. As the radius decreases according to eq.2.11, the density increases and the Fermi momentum increases, so that the degenerate electrons are finally driven to a relativistic velocity. At this point, the degenerate pressure of the relativistic degenerate material is

$$P_e = \frac{1}{8}\left(\frac{3}{\pi}\right)^{1/3} ch\left(\frac{\rho}{\mu_e m_p}\right)^{4/3} = 1.232\times10^{10}\left(\frac{\rho}{\mu_e}\right)^{4/3} \quad [\mathrm{N/m^2}]. \tag{2.12}$$

Since the index changes from 5/3 to 4/3, the increase in electron degeneracy pressure slows down and it becomes impossible to support itself. The mass at which the white dwarf collapses

is known as the Chandrasekhar mass limit, is represented,

$$M_{\rm ch} = 1.46 \left(\frac{2}{\mu_e}\right)^2 M_\odot \xrightarrow[\mu_e=2]{} 1.46 M_\odot. \tag{2.13}$$

2.1.3 Mass transfer

In a semi-detached compact binary system, which contains a compact star such as a black hole, a neutron star, or a white dwarf, the secondary usually fills the Roche lobe. Since the net force working to the matter at L_1 is zero ($\partial \Phi_R / \partial x = 0$), the gas is pushed out to the primary side through L_1 by the pressure of the secondary. The flow resembles the gas stream from the nozzle to the vacuum. Details of the stream lines in L_1 are given by Lubow and Shu (1975).

Since the binary system is rotating, the gas stream feels Coriolis effect and has angular momentum with respect to the primary, thus rotating around it (Fig.2.2). The ring formed by the gas has a finite radius and rotates differentially according to the local Keplerian velocity,

$$v_{\rm K}(r) = \left(\frac{GM_1}{r}\right)^{\frac{1}{2}}. \tag{2.14}$$

This shearing flow generates heat from the viscous process of the gas. As the heat energy is released through radiation, the drained energy is complimented by the particles moving deeper into the gravitational potential of the primary. At the same time some particles must move outwards to conserve angular momentum. Thus the ring spreads and the disk is formed. With the disk fully established, a shock-heated area called a bright spot is created when the gas stream impacts the outer edge and shines brightly in the optical wavelength.

2.1.4 Accretion Disk

We derive equations of motion of the gas in the accretion disk. As the momentum of the gas from the secondary is initially confined in the orbital plane in this section we will assume a geometrically thin disk. As the gas in the disk approaches the primary, the gravitational field of the secondary may be ignored. When the gas is in a circular motion, the angular velocity of particles is given the local Keplerian value

$$\Omega_{\rm K}(r) = \left(\frac{GM_1}{r^3}\right)^{\frac{1}{2}}, \tag{2.15}$$

and has a local Keplerian velocity $v_{\rm K}(r) = r\Omega_{\rm K}(r)$. Due to viscous shear between adjacent annuli, the inner annulus transfers its angular momentum to the outer annulus, which raises the radial drift velocity $v_{\rm rad}(r,t)$ (Pringle 1981). We then define a surface density $\Sigma(r,t)$, which is the mass per unit area integrated in the z direction through the disk. The disk structure is determined by the time-dependent equations obtained from conservation of the mass ($2\pi r \cdot \delta r \cdot$

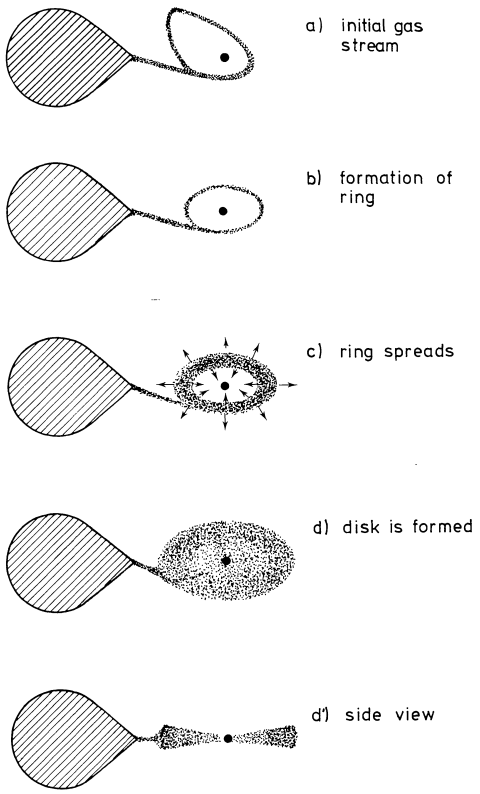

Fig. 2.2 Schematic illustration of formation of accretion disk (Verbunt 1982).

Σ) and the angular momentum ($2\pi r \cdot \delta r \cdot \Sigma \cdot r^2\Omega$), these are given,

$$\frac{\partial \Sigma}{\partial t} = \frac{1}{r}\frac{\partial}{\partial r}(r\Sigma v_{\rm rad}) \tag{2.16}$$

and

$$\frac{\partial}{\partial t}(\Sigma r^2\Omega) + \frac{1}{r}\frac{\partial}{\partial r}(r\Sigma v_{\rm rad} r^2\Omega) = \frac{1\partial}{r\partial r}\left(r^3 \nu_{\rm k}\Sigma\frac{d\Omega}{dr}\right), \tag{2.17}$$

where $\nu_{\rm k}$ is the coefficient of effective kinetic viscosity of the gas. By eliminating $v_{\rm rad}$ from eq.2.16 and 2.17, the equation for the surface density as a function of time is given

$$\frac{\partial \Sigma}{\partial t} = -\frac{1}{r}\frac{\partial}{\partial r}\left(\frac{1}{d(r^2\Omega)/dr}\frac{\partial}{\partial r}\left(\nu_{\rm k}\Sigma r^3\frac{d\Omega}{dr}\right)\right). \tag{2.18}$$

If the disc is in a circular Kepler orbit, $\Omega \propto r^{-3/2}$, eq.2.18 is simplified

$$\frac{\partial \Sigma}{\partial t} = \frac{3}{r}\frac{\partial}{\partial r}\left(r^{1/2}\frac{\partial}{\partial r}\left(\nu_{\rm k}\Sigma r^{1/2}\right)\right). \tag{2.19}$$

This is the basic equation for the time evolution of surface density in a Keplerian disk. Eq.2.19 can be solved Pringle (1981) to show how the ring spreads out into a disk (Fig.2.3). Most of the matter moves inwards to the primary by losing energy and angular momentum, while some

matters move out to larger radii according to the conservation law of the angular momentum of the disk. It results in Σ being able to change only on the viscous time scale $t_\nu(r) \sim r^2/\nu_{\rm k}$.

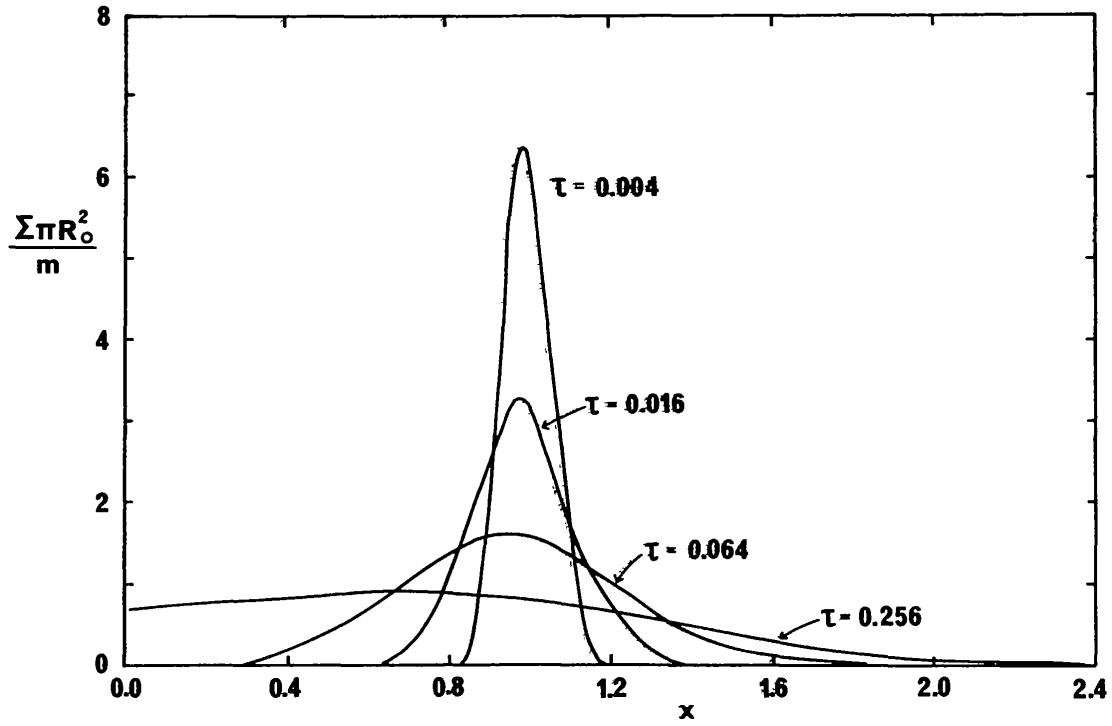

Fig. 2.3 Viscous revolution of ring of mass m. Surface density Σ is shown as a function of $x = r/R_0$, where R_0 is initial radius of ring, and dimensionless time $\tau = 12\nu_{\rm k} t R_0^{-2}$. (Pringle 1981).

If the mass transfer rate from the secondary to the disk changes on a time scale much longer than t_ν, the disk settles in a steady state ($\partial\Sigma/\partial t = 0$). The mass conservation equation (2.16) is then integrated to give the obvious result

$$\dot{M}(d) = 2\pi r(-v_{\rm rad})\Sigma \quad (v_{\rm rad} < 0) \tag{2.20}$$

To integrate eq.2.18 or 2.19, it is necessary to set boundary conditions at the inner and outer edges of the disk. If the magnetic field is weak and does not affect the flow near the primary, the disk extends to the surface of the white dwarf ($r = R_1$). As the primary rotates with an angular velocity $\Omega_1 < \Omega_{\rm K}(R_1)$, there must exist a boundary layer that decelerates matter with the local Keplerian velocity to match the rotation speed of the primary. Since the radial extent of the boundary layer is expected to be very thin ($\ll R_1$), the state of $d\Omega/dr = 0$ occurs near $r = R_1$, where $\Omega = \Omega_{\rm K}(R_1)$. The inner boundary layer condition is given using eq.2.19 and

2.20 by,

$$\nu_{\rm k}\Sigma = \frac{\dot{M}(d)}{3\pi}\left(1-\left[\frac{R_1}{r}\right]^{1/2}\right), \tag{2.21}$$

see Koen (1988) and Duschl and Tscharnuter (1991) for details. On the other hand, at the outer boundary, it is assumed that tidal interaction drains the outward flow of the angular momentum. The energy generation rate of viscous shear is

$$\begin{aligned} D(r) &= \nu_{\rm k}\Sigma\left(r\frac{d\Omega}{dr}\right)^2 \\ &= \frac{3GM_1\dot{M}(d)}{4\pi r^3}\left(1-\left[\frac{R_1}{r}\right]^{1/2}\right) \end{aligned} \tag{2.22}$$

from eq.(2.15) and (2.21). This energy is radiated from both sides of the disk with a blackbody radiation, $2\sigma T_{\rm eff}^4(r)$, where $T_{\rm eff}$ is the effective temperature and σ is the Stefan-Boltzmann constant. Hence the radial temperature of the disk is given in

$$T_{\rm eff}(r) = \left[\frac{3GM_1\dot{M}(d)}{8\pi\sigma r^3}\left(1-\left[\frac{R_1}{r}\right]^{1/2}\right)\right]^{\frac{1}{4}} \tag{2.23}$$

This equation shows that the surface temperature of a steady state accretion disk increases from its outer edge to a maximum near the primary. If the disk has a typical $\dot{M}(d)(10^{16}-10^{18}$ g $\rm s^{-1})$, it is expected to emit ultraviolet light at $\sim 10^4$ K at the inner edge near the white dwarf and infrared light at $\sim 10^3$ K at the outer edge of the disk.

Using Eq.(2.22), the total disk luminosity is

$$L_{\rm disk} = \int_{R_1}^{\infty} D(r)\cdot 2\pi r dr = \frac{1}{2}\frac{GM_1\dot{M}(d)}{R_1}. \tag{2.24}$$

This is only one half of the total available accretion energy, since the total potential drop from infinity to radius R_1 is GM/R_1. Thus, the rest of the accretion luminosity is emitted from the boundary layer.

Optical thickness of the disk is related with its vertical structure. In the vertical (z) direction of the disk, there is a hydrostatic equilibrium between the pressure gradient and the z-direction component of the gravitational force of the primary star:

$$\frac{\partial P}{\partial z} = \rho\frac{\partial}{\partial z}\left(\frac{GM_1}{(r^2+z^2)^{1/2}}\right). \tag{2.25}$$

For a thin disk ($z \ll r$), and this becomes

$$\frac{\partial P}{\partial z} = -\rho\frac{GM_1 z}{r^3}. \tag{2.26}$$

If the typical scale height of the disk in the z-direction is H, we can set $\partial P/\partial z \sim P/H$ and $z \sim H$. From $P \sim \rho c_s^2$, where c_s is the sound speed. Consequently, eq.2.26 gives

$$\begin{aligned} H &= \left(\frac{r^3}{GM_1}\right)^{1/2} c_s \\ &= \frac{c_s}{\Omega_{\rm K}(r)} \end{aligned} \tag{2.27}$$

or

$$\frac{H}{r} = \frac{c_s}{v_{\rm K}(r)}. \tag{2.28}$$

Since the disk is geometrically thin ($H \ll r$), the local Keplerian velocity is highly supersonic. For an isothermal z-structure, the hydrostatic equation 2.26 would give

$$\rho(r,z) = \rho_c(r) \exp\left(\frac{-z^2}{2H^2}\right), \tag{2.29}$$

where $\rho_c(r)$ is the density in the central plane (z = 0) of the disk. Thus the density falls off rapidly with height above the plane.

If the disk is optically thick in the z direction, as in the case of stellar atmospheres, eq. 2.26 must be solved simultaneously with the radiative transfer equation for the radiative flux $F(z)$ through the surface of the disk:

$$F(z) = \frac{-16\sigma T^3(z)}{3\kappa_{\rm R}\rho}\frac{\partial T}{\partial z} \ , \tag{2.30}$$

where $\kappa_{\rm R}$ is the Rosseland mean absorption coefficient. It is implicitly assumed in eq. 2.30 that the disc is optically thick in the sense that

$$\tau = \rho H \kappa_{\rm R} = \Sigma \kappa_{\rm R} \gg 1, \tag{2.31}$$

so that the radiation field is locally very close to the blackbody emission. However, if $\tau \leq 1$, although the radiation escapes more easily from the central plane region of the disk, the emissivity of the gas is lower than that of a blackbody. Hence the gas temperature must be higher than in the optically thick case.

The spectrum emitted by each element of area of the disk is approximated as follows

$$I_\nu = B_\nu(T(r)) = \frac{2h\nu^3}{c^2}\frac{1}{\exp(h\nu/kT(r)) - 1}. \tag{2.32}$$

The observed flux distribution of the disk as seen by an observer at a distance d is

$$F_\nu = \frac{2\pi\cos i}{d^2}\int_{R_1}^{r_d} I_\nu r dr, \tag{2.33}$$

where i is the inclination of the disk and r_d is the radius of the disk, since a ring between radii r and $r + dr$ subtends solid angle $2\pi r dr \cos i / d^2$. With the blackbody assumption, we get

$$F_\nu = \frac{4\pi h\nu^3 \cos i}{c^2 d^2} \int_{R_1}^{r_d} \frac{r}{\exp(h\nu/kT(r)) - 1} dr. \tag{2.34}$$

The flux given by eq. 2.34 is independent of the disk viscosity. This is a consequence of both the steady state and blackbody assumptions. Conversely, observations of the steady state disks cannot be used to investigate the nature of their viscosity. Shakura and Sunyaev (1973) approach, which is still commonly in use, is to parameterize $\nu_{\rm k}$ as

$$\nu_{\rm k} = \alpha c_s H, \tag{2.35a}$$

$$= \alpha H^2 \Omega_{\rm K}(r) \tag{2.35b}$$

which may be thought of as the viscosity generated by turbulent eddies of size H and turnover speed αc_s. For subsonic turbulence $\alpha < 1$. The radial drift velocity is given by

$$v_{\rm rad} \sim \frac{\nu_{\rm k}}{r} = \alpha \left(\frac{H}{r}\right) c_s, \tag{2.36}$$

which shows that the radial drift velocity is highly subsonic, and, from eq. 2.20

$$\dot{M}(d) \sim 2\pi\alpha\Omega_{\rm K}(r) H^2 \Sigma \tag{2.37}$$

More realistic values of α (~ 0.1) lead to optically thick disks except at low temperatures ($T \lesssim 4000$ K) in the inner regions (Tylenda 1981, Smak 1984*a*, 1992). With low $\dot{M}(d)$ and $\alpha \sim$0.02, as in DN at quiescence, only the region $r < 1 \times 10^{10}$ cm is optically thin.

2.1.5 Boundary layer

From the conservation laws of energy and angular momentum it can be shown (Kley 1991) that the luminosity released in the boundary layer (BL) is

$$L_{\rm BL} = L_{\rm disk} \left(1 - \frac{\Omega_1}{\Omega_{\rm K}(R_1)}\right)^2. \tag{2.38}$$

When the primary rotates slowly ($\Omega_1 \ll \Omega_{\rm K}(R_1)$), it becomes difficult to distinguish the luminosity between the disk and BL. Therefore, it can be expected that the luminosity characteristics of BL depend on its optical thickness.

A schematic picture of the BL is show in Fig.2.4. If the BL is optically thick, the luminosity is considered as a blackbody radiated in the region $\sim 2\pi R_1 2H$ and diffused through a distance

$\sim H$. The effective temperature of the BL for a non-rotating primary is then given by

$$4\pi R_1 H \sigma T_{\rm BL}^4 \approx \frac{1}{2}\frac{GM_1\dot{M}(d)}{R_1}, \tag{2.39}$$

assuming radiation pressure can be neglected. Therefore, the bulk of the radiation from the optically thick BL appears in by the soft X-ray and EUV regions at $\sim 10^5$ K.

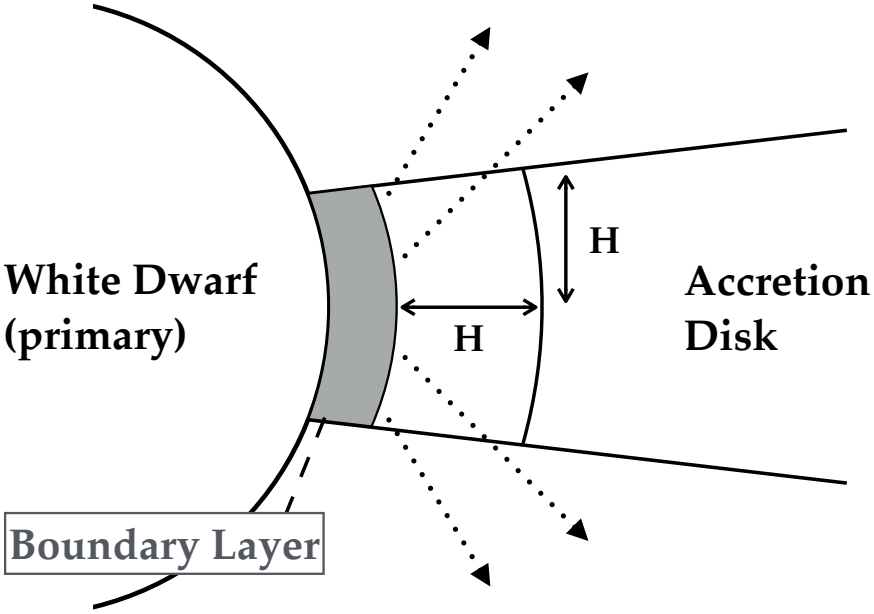

Fig. 2.4 Schematic view of optically thick boundary layer (in plane perpendicular to plane of disk).

If the BL is optically thin, the radiation is emitted directly from the shock front that formed as the rotating gas collides with the surface of the primary. The temperature of the post-shock gas is (e.g., Frank et al. (2002))

$$T_{\rm sh} = \frac{3}{16}\frac{\mu_{\rm m} m_{\rm H}}{k} v_{\rm p}^2$$

as long as the shock is strong enough, where $v_{\rm p}$ is the pre-shock velocity, and when it collides with the primary in a circular orbit,

$$\begin{aligned} T_{\rm sh} &= \frac{3}{16}\frac{\mu_{\rm m} m_{\rm H}}{k}\frac{GM_1}{R_1} \\ &= 1.85\times 10^8 \left(\frac{M_1}{M_\odot}\right)\left(\frac{R_1}{10^9}\right)^{-1} \quad \text{K}. \end{aligned} \tag{2.40}$$

Thus an optically thin BL should radiate in hard X-rays, with energies $= 20$ keV. In an optically thin gas at a temperature of 10^8 K, cooling occurs through bremsstrahlung. If the cooling time $t_{\rm cool}$ is longer than the adiabatic expansion time scale $t_{\rm ad}$ then the BL will expand to form a hot, X-ray emitting corona (Pringle and Savonije 1979, King and Shaviv 1984, King 1986, Narayan

and Popham 1993).

2.2 Dwarf Nova

A dwarf nova (DN) is a subclass of CV. The DN shows an optical outburst with a recurrence time of 10 days to decades (Fig.2.5). During the outburst, the DN becomes brighter than in quiescence by a few to several magnitudes in the V-band. DN is classified into three major subclasses based on the characteristics of the light curve during an outburst.

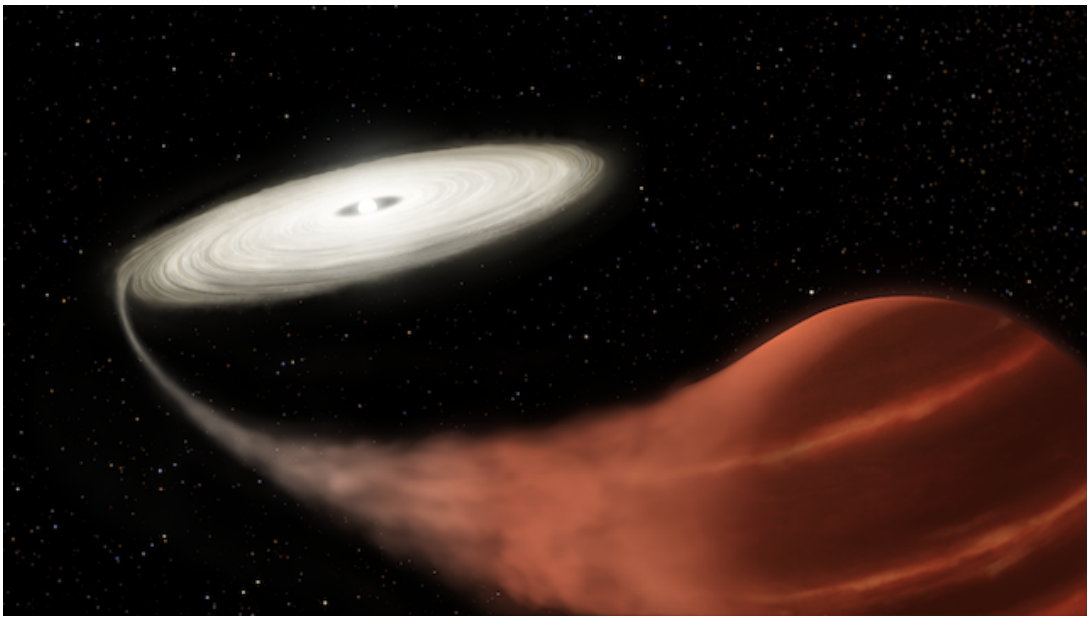

Fig. 2.5 Schematic view of Dwarf Nova. (Foreground) Secondary star. (Back) Accretion disk and white dwarf in at center.
`https://hubblesite.org/image/4622`

U Gem type

In 1855, J.R. Hind discovered the first dwarf nova "U Gem", which is so famous and typical that it becomes a subclass name of dwarf novae. U Gem-type shows only a normal outburst.

Z Cam type

Z Cam-type DN causes occasional standstills about 0.7 magnitude below the maximum brightness at the end of an outburst, in addition to the normal outburst. The standstill keeps its brightness for tens of days to years.

SU UMa type

SU UMa-type DN shows not only the normal outburst but also a superoutburst. The superoutburst is brighter in the optical band than the normal outburst by ~ 1 mag at its peak, and lasts for $\sim 7 - 10$ days, longer than the normal outburst (a few days). During

the super outburst, periodic photometric humps with an amplitude of 0.2–0.3 mag are observed, called superhumps.

2.2.1 Thermal Instability

The accretion disc of the DN is bi-stable. One stable state corresponds to a low accretion-rate state in which the temperature of the outer part of the disc is low (of order 10^3 K) and hydrogen there is neutral. The other is a high accretion-rate state in which the outer part temperature exceeds 10^4 K and the hydrogen is ionized. The former and the latter correspond to an optically-quiescent state and an outburst state, respectively. Since the mass accretion rate from the secondary is intermediate, the DN shows switching behavior between the two states due to thermal instability associated with hydrogen ionization/recombination (Osaki 1974, Hōshi 1979, Meyer and Meyer-Hofmeister 1981). The thermal limit cycle of accretion disk is shown in Fig.2.6. First, suppose that the accretion disk is in a low density and a low temperature state A. At this state, the mass accretion rate from the disk to the primary is smaller than the mass transfer rate from the secondary to the disk. As the gas is transferred from the secondary, the density of the disk increases and is slowly heated. When the state of the disk reaches near point B, the hydrogen begins to ionize at a certain temperature. Since the partially ionized state is unstable, the hydrogen transitions to the fully ionized stable state C. At high temperatures, the accretion disk becomes more viscous, and the matter in the disk accretes rapidly to the primary, resulting in a gradual decrease in density. (section CD) When the density is sufficiently small, the disk returns to quiescence (section DA).

2.2.2 Tidal Instability

The superoutburst that is observed in SU UMa type DN is caused by the tidal instability in addition to the thermal instability of the accretion disk (Whitehurst 1988, Osaki 1989, Hirose and Osaki 1990, Osaki 1996). Figure 2.7 illustrates the time evolution of the accretion disk of SU UMa type DN. During the normal outburst, the disk mass continues to decline due to accretion onto the white dwarf, but the total mass loss per outburst is smaller than the gain of mass between the two outbursts. Hence the disk gradually gets heavier and extends outward. In the normal outburst due only to the thermal instability, some matter accretes to the primary, while the remaining matter moves to the outer edge to preserve the angular momentum of the disk. When the radius of the disk reaches 0.47 times the distance between the binary (a), so-called the 3:1 resonance is triggered in the disk and the orbiting secondary. The disk deforms into an eccentric elliptical shape, causing tidal instability. The angular momentum in the disk is transported to the orbital angular momentum of the binary system due to increased viscosity caused by the thermal instability and the tidal friction caused by the tidal instability. The matter accumulated in the disk collectively rushes to the primary and shows a large and long brightening. This condition is met only for a low mass secondary with the mass ratio

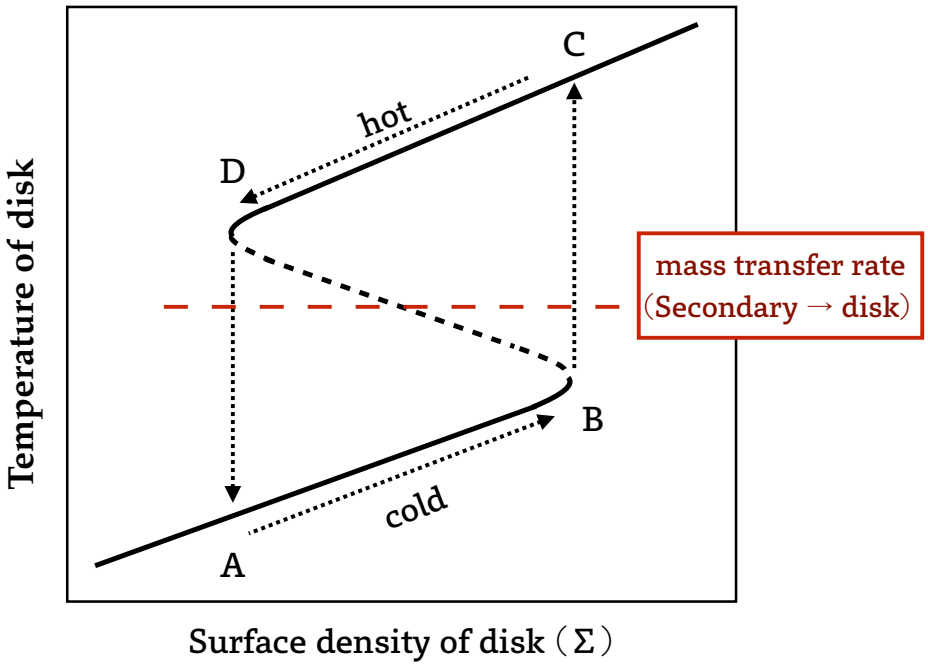

Fig. 2.6 Schematic diagram showing thermal limit cycle of disk.

$q = M_2/M_1 < 0.25$.

Figure 2.8 illustrates locations of each DN subtype in the plane between the orbital period and the mass transfer rate from the secondary to the disk. CVs that cause thermal instability are bounded by broken lines that divide Fig.2.8 into upper and lower parts. There are extremely few CVs with orbital periods of 2.2 to 2.8 hours, which is called the periodic gap. On the other hand, CVs are also known to have a correlation between the orbital period of the binary system and the mass of the secondary. For CVs with orbital periods of less than 2 hours, the secondary mass is estimated to be less than about 0.2 $M_\odot$. Since the typical mass of a white dwarf is 0.8–1 $M_\odot$, the observed SU UMa DN have orbital periods below the period gap is in good agreement with the theoretical prediction.

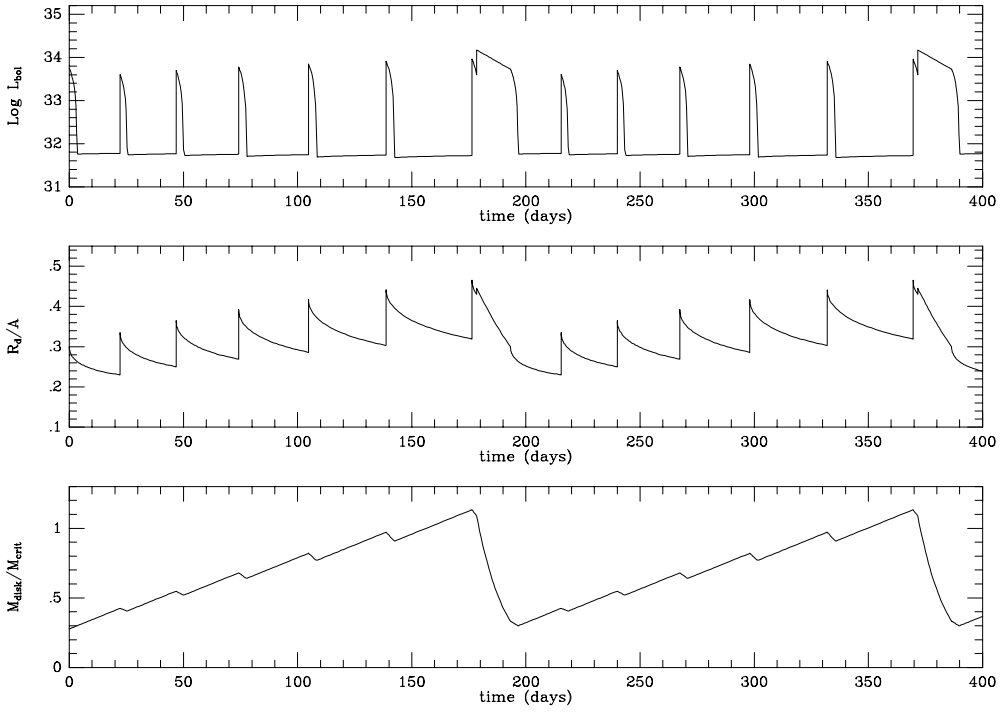

Fig. 2.7 Time evolution of accretion disk of SU UMa type DN by a numerical simulation (Osaki 2005). Top panel is bolometric light curve. Middle panel is disk radius R_d in units of binary separation A. Bottom panel is total disk mass M_{disk} normalized by critical mass M_{crit} above which disk can be tidally unstable.

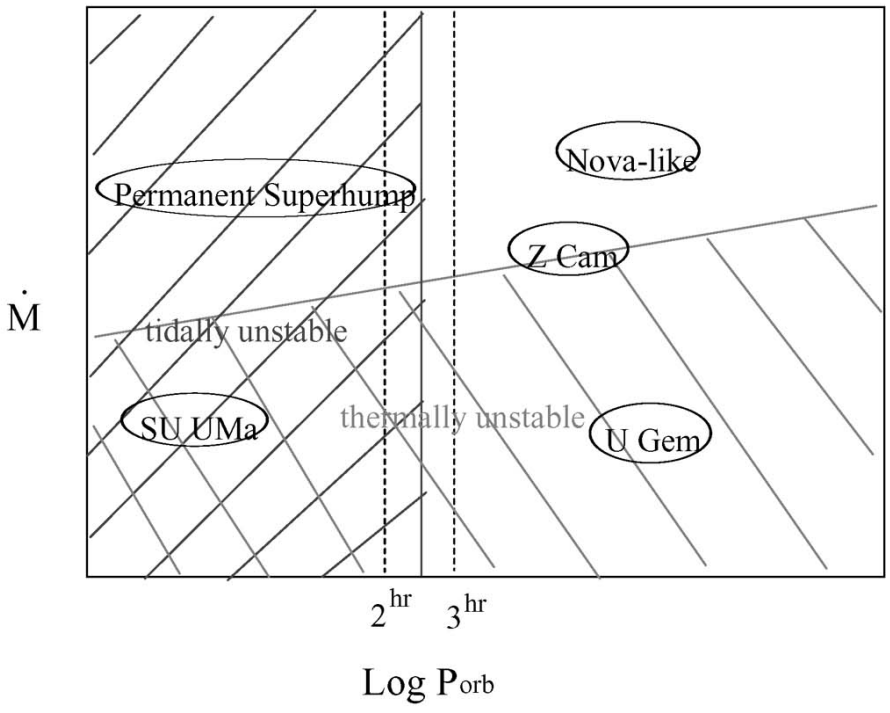

Fig. 2.8 Diagram of CVs between orbital period and mass transfer rate from secondary to disk (Osaki 2005).

CHAPTER 3

X-ray emission from optically thin thermal plasma

Dwarf novae in quiescent state, where the mass accretion rate is low, emit X-rays from plasma with temperatures higher than 10^8 K. The hot plasma is located in the "boundary layer", defined as a region between the innermost edge of the accretion disk and the white dwarf surface. In this chapter, we describe the mechanism of X-ray emission from optically thin thermal plasmas to understand the X-ray spectra observed from dwarf novae.

3.1 Collisional plasma

Plasma in which the inner core electrons of an atom are ionized or excited by collisions of free electrons is called as collisional ionization plasma. There are four major atomic processes in plasmas: ionizaion, recombination, excitation, and de-excitaion. In the collisional ionization plasma, there are four types of ionization processes and their reverse processes, i.e., recombination processes. These four types are as follows:

- collisional ionization / three-body recombination,
- photoionization / radiative recombination,
- collisional excitation auto-ionization / dielectronic-recombination collisional de-excitation,
- photo-excitation auto-ionization / dielectronic recombination.

When the plasma density is sufficiently high and the plasma is in collisional ionization equilibrium, the above ionization and recombination processes are perfectly balanced. However, this balance does not hold for optically thin plasmas with electron density lower than 10^{14-16} cm^{-3}. These cases are called coronal plasmas.

3.2 Coronal plasma

Coronal plasma is a sort of thermal plasma that satisfies all five characteristics described below.

1. The plasma is optically thin. Therefore, the radiation generated in the plasma is not attenuated by itself and does not affect the energy level distribution of the atoms.

2. The density of the plasma is sufficiently low, and the probability that atoms exist in excited states is negligible compared to the ground state.

3. The energy lost from the plasma due to radiation is provided by non-radiative mechanical heating (mainly by electron impact).

4. The energy distribution of electrons and ions in the plasma is represented by the Maxwell distribution of common temperatures (kinetic thermal equilibrium).

5. The ionization distribution (i.e., the abundance ratio of each ionic species) for each element is in a steady state and is determined by the balance between ionization and recombination (ionization equilibrium).

3.3 Ionization distribution

Time development of the ionization distribution of any given species in a collisional ionization plasma for the ion density $N_{Z,z}$, where Z is the atomic number and z is the charge number, is given by

$$\frac{1}{n_e}\frac{dN_{Z,z}}{dt} = N_{Z,z-1}S_{Z,z-1} - N_{Z,z}\left(S_{Z,z} + \alpha_{Z,z}\right) + N_{Z,z+1}\alpha_{Z,z+1}, \tag{3.1}$$

where $S_{Z,z}$ is the ionization rate coefficient ($\mathrm{cm^3 s^{-1}}$) for the process of $Z^z \rightarrow Z^{z+1}$, and $\alpha_{Z,z}$ is the recombination rate coefficient ($\mathrm{cm^3 s^{-1}}$) for the process of $Z^z \rightarrow Z^{z-1}$. Both $S_{Z,z}$ and $\alpha_{Z,z}$ are functions of the electron temperature T_e only.

According to the condition 2 in section 3.2, in coronal plasma, all ions are in their ground state. Equation 3.1 is therefore a $z+1$-dimensional vector equation that is much easier to handle than in the general case, where the excitation state must also be considered (Masai 1984). Under ionization equilibrium (condition 5 in section 3.2), the ionization distribution of the coronal plasma can be determined by setting zero on the left-hand side of eq. 3.1. Then the relation between the neighboring ions can be described by the following equation,

$$\frac{N_{Z,z+1}}{N_{Z,z}} = \frac{S_{Z,z}(T_e)}{\alpha_{Z,z+1}(T_e)}, \tag{3.2}$$

and thus we derive

$$N_{Z,0} = N_Z\left[1 + \sum_{k=1}^{Z}\prod_{j=0}^{k-1}\left(\frac{S_{Z,j}}{\alpha_{Z,j+1}}\right)\right]^{-1}, \quad N_{Z,k} = N_{Z,0}\prod_{j=0}^{k-1}\left(\frac{S_{Z,j}}{\alpha_{Z,j+1}}\right) \quad (k \geq 1), \tag{3.3}$$

where N_Z is the atomic density of the atomic number Z independent of the ion state ($N_Z = \sum_{z=0}^{z=Z} N_{Z,z}$).

3.4 Ionization and recombination process of coronal plasma

To obtain the ionization distribution of coronal plasmas, we need to know the elementary processes that should be included in $S_{Z,z}(T_e)$ and $\alpha_{Z,z}(T_e)$. According to condition 1 (namely, optically thin) in section 3.2, we can neglect the processes in which emitted photons are re-absorbed, e.g., photo-ionization and photo-excitation auto-ionization. Also, since the plasma is optically thin, there is no need to consider the effects of three-body collisions ("three-body recombination" and "dielectronic-recombination collisional de-excitation"). A more detailed description is given in references (Masai 1984, Arnaud and Rothenflug 1985, Mewe et al. 1985, Arnaud and Raymond 1992, Porquet et al. 2001) and the references cited therein.

Two types of ionization and recombination processes contribute to the collisional ionization rate coefficient ($S_{Z,z}(T_e)$) and the recombination rate coefficient ($\alpha_{Z,z}(T_e)$). They are summarized below and Table 3.1.

Collisional ionization

It is a process in which a bound electron of the ion Z^z is ejected by a free electron impact and the ionization degree is raised to Z^{z+1}.

Collisional-excitation auto-ionization

Collisional-excitation is the process in which a bound electron of the ion Z^z is excited to a higher level by an electron collision. The asterisk in the Table 3.1 indicates that the ion is in an more excited state. When the excitation energy exceeds the ionization energy of other bound electrons, the excited electron can transfer its energy to one of those electrons, which is emitted from the ion.

Radiative recombination

It is a process by which ion captures a free electron and releases excess energy as a photon.

Dielectronic recombination

When an ion captures a free electron, the energy originally retained by the free electron can excite one of the bound electrons and results in a doubly excited state. Then, the ion is stabilized by either emitting one of the excited electrons (auto ionization) or radiative decay. The latter is called dielectronic recombination. The emission line from this process is called dielectron recombination satellite lines of $Z^{(z-1)^*}$ and appears near the long-wavelength (or low-energy) side of the Z^{z*} resonance line.

The ionization distributions of oxygen, silicon, sulfur (Mazzotta et al. 1998), and iron (Bryans et al. 2006) obtained by substituting $S_{Z,z}(T_e)$ and $\alpha_{Z,z}(T_e)$ into eq.3.3 are shown in Fig. 3.1 as a function of electron temperature. As the temperature of the plasma increases, ionization proceeds. Neutral atoms are distributed at the lowest temperature, while fully ionized ions are distributed at the highest temperature.

Table 3.1 Ionization and recombination process

Atomic process	Ionization state
Collisional ionization	$Z^z + e^- \rightarrow Z^{(z+1)} + 2e^-$
Auto ionization	$Z^z + e^- \rightarrow Z^{z^*} + e^- \rightarrow Z^{z+1} + 2e^-$
radiative recombination	$Z^{(z+1)} + e^- \rightarrow Z^z + h\nu$
Dielectronic recombination	$Z^{(z+1)} + e^- \rightarrow Z^{z^*} \rightarrow Z^z + h\nu$

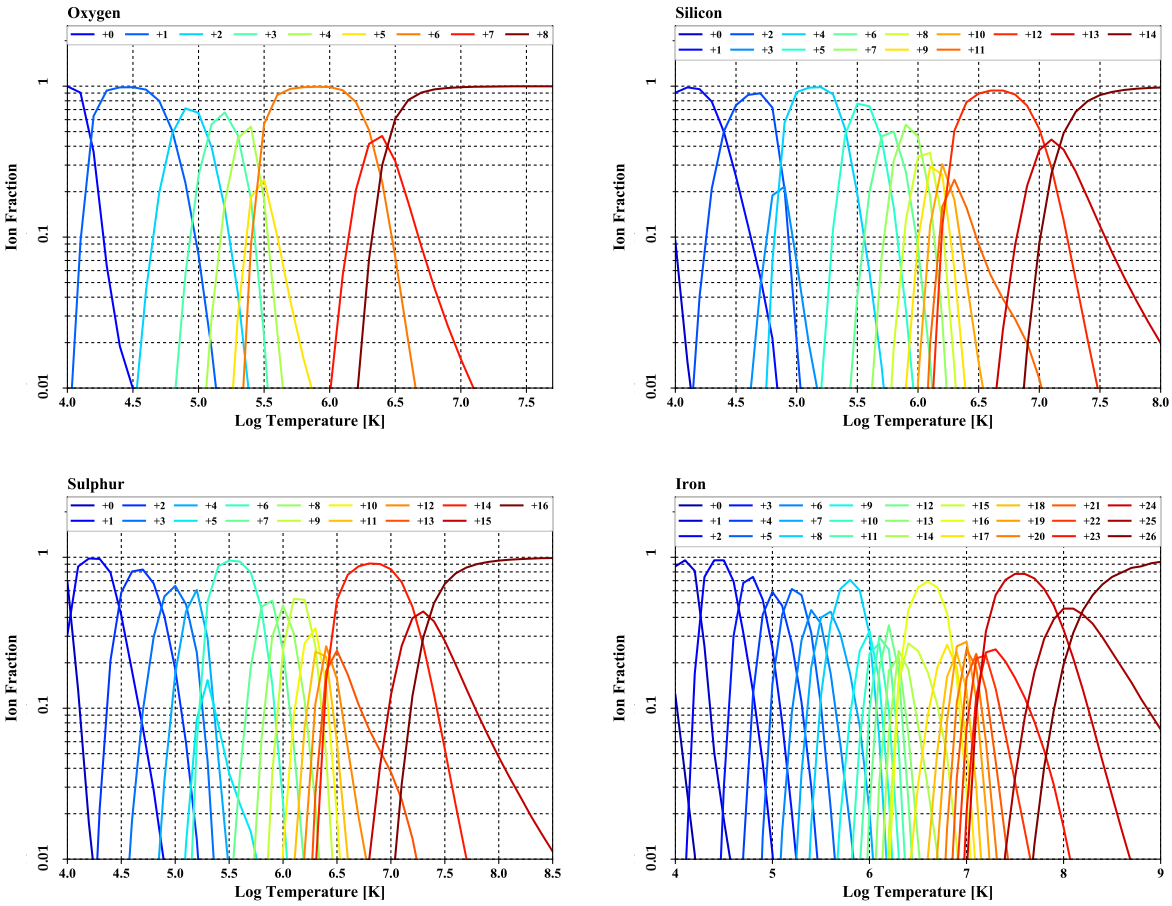

Fig. 3.1 Ionization distributions of oxygen, silicon, sulfur, and iron ions as function of temperature.

3.5 Line emission

3.5.1 Volume emissivity

The line emission is caused by atomic processes such as inner-shell ionization (II), (direct) excitation (E), inner-shell excitation (IE), radiative recombination to excited states (RR), and dielectronic recombination (DR). The volume emissivity $j_{Z,z}$ of the emission line associated with a state transition occurring in an optically thin thermal plasma is given by (Mewe et al. 1985)

$$j_{Z,z} = \left(\frac{N_H}{n_e}\right)\left(\frac{N_Z}{N_H}\right) n_e^2 \left[S_{z-1}^{\mathrm{II}}\eta_{z-1} + \left(S_z^{\mathrm{E\ or\ IE}} + \alpha_z^{\mathrm{DRS}}\right)\eta_z + \left(\alpha_{z+1}^{\mathrm{RR}} + \alpha_{z+1}^{\mathrm{DR}}\right)\eta_{z+1}\right], \tag{3.4}$$

where N_H and N_Z are the densities of hydrogen and the element of atomic number Z, respectively. (N_Z/N_H) is the ratio of the element's abundance relative to hydrogen. $\eta_{Z,z} = N_{Z,z}/N_Z$ is the ionization distribution obtained in section 3.3. S_z^{II}, $S_z^{\mathrm{E\ or\ IE}}$, α_z^{RR} and α_z^{DR} are the reaction rate coefficients for inner-shell ionization of ion Z^{z-1}, excitation or inner-shell excitation of Z^z, and radiative and two-electron recombination of Z^{z+1}, respectively. α_z^{DRS} is the reaction rate coefficient of recombination generating satellite lines that have small energy separation from the ion Z^{+z} emission lines.

3.5.2 Hydrogen-like and Helium-like Lines

The line emission is monochromatic radiation caused by the bound-bound transition of an electron between two different energy levels of an atom. The most common emission lines seen in X-ray astronomy are characteristic X-rays from hydrogen-like (i.e. ions with a single electron) and helium-like (i.e. with two electron) elements with even atomic numbers from carbon to nickel. Note that the use of the phrase "hydrogenic" when describing an ion with a single electron should be avoided, as it can mean an ion modeled using the hydrogenic wave function. According to atomic theory, the electrons in an atom or ion are bound to a "shell" whose principal quantum number n starts from 1 and increases infinitely. Shells with quantum numbers $n = 1, 2, 3$, and 4 are commonly referred to as K, L, M, and N shells, respectively. The Greek letters are then used to indicate the difference of the principal quantum number of the transition, so that $\alpha, \beta,$ and γ refer to $\Delta n = 1, 2,$ and 3, respectively. Thus, the emission lines from hydrogen-like ions are described as Kα ($n = 2 \rightarrow 1$), Lγ ($n = 5 \rightarrow 2$), and Mβ ($n = 5 \rightarrow 3$), respectively.[1]

The relationship between the ground state of the helium-like ion and the energy levels for one electron at $n = 2$ is summarized in the Fig. 3.2. Here, the emission line due to the transition from $^1P_1$ and $^3S_1$ to the ground state $^1S_0$ are called a resonance line (w) and a forbidden line (z),

[1] For a hydrogen atom, transitions ending on the $n = 1, 2,$ and 3 shells are described as Lyman, Balmer, and Paschen series (usually shortened as Ly, H, and Pa). Therefore, the transitions are described as Lyα ($n = 2 \rightarrow 1$), Hγ ($n = 5 \rightarrow 2$), and Paβ ($n = 5 \rightarrow 3$), respectively.

respectively, and the transitions from $^3P_2$ and $^3P_1$ to $^1S_0$ are intercombination transition lines, denoted by x and y, respectively (Gabriel and Jordan 1969, Gabriel 1972). However, since it is difficult to clearly separate these four lines with the X-ray instrument used in this study, we collectively refer to the emission lines from the $n = 2 \rightarrow 1$ bound-bound transition as Kα lines.

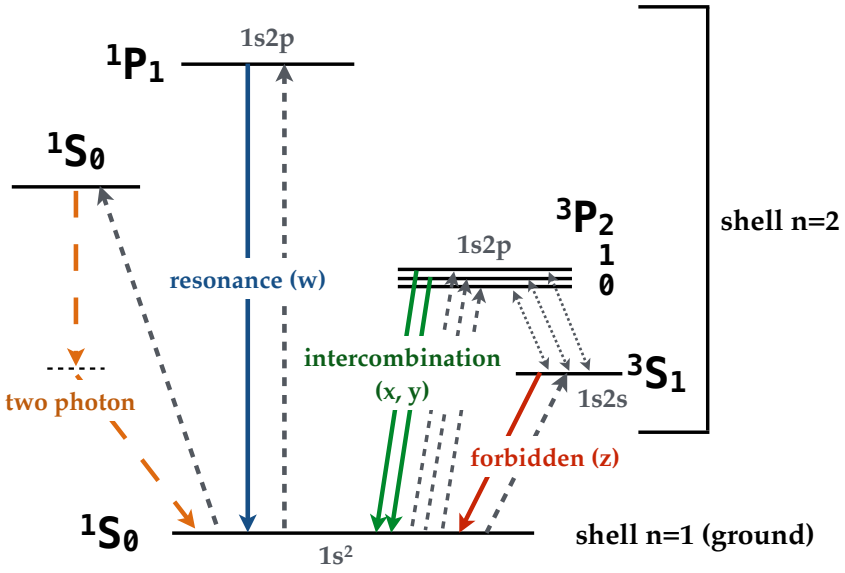

Fig. 3.2 Schematic diagram of energy level of helium-like ion. Solid downward arrow : radiative transition, broken arrow : collision excitation.

The line-energy E of a photon absorbed or emitted in the transition between two energy levels of principal quantum numbers n and n' is given by,

$$E \sim R_y \cdot (Z - b)^2 \left(\frac{1}{n^2} - \frac{1}{n'^2} \right). \tag{3.5}$$

This is called Moseley's law, where R_y is the Rydberg constant (= 13.60 eV), Z is the atomic number of the element. b is a correction term representing the screening of nucleus charge by the electrons that have nothing to do with the transition in question, which is 0 for hydrogen-like, ~ 0.4 for helium-like, and ~ 1 for neutral emission lines.

3.6 Continuum emission

The continuum emissivity from optically thin thermal X-ray sources is given by Mewe et al. (1986),

$$P_c(\lambda, T) = 2.051 \times 10^{-22} n_e^2 G_c \lambda^{-2} T^{-\frac{1}{2}} e^{\frac{-143.9}{\lambda T}} \quad [\mathrm{erg\ cm^{-3}\ s^{-1}\ \AA^{-1}}] \tag{3.6}$$

where n_e is the electron density [cm^{-3}], T the temperature [MK], λ is given in Å. G_c is the average total Gaunt factor, including contributions from thermal bremsstrahlung (free-free emission), radiative recombination continuum (free-bound emission), and the two-photon decay. It is written as the sum of the Gaunt factors of these three processes :

$$G_c = G_{ff} + G_{fb} + G_{2\gamma}. \tag{3.7}$$

Detailed calculations of the each Gaunt factor are given in Gronenschild and Mewe (1978).

Thermal bremsstrahlung (free-free emission)

Thermal bremsstrahlung occurs when free electrons are accelerated by the Coulomb force as they move through the electric field created by ions and transition to different free electron energy states. At $T \geq 10^8$ K, most of the atoms are ionized, so the thermal bremsstrahlung is dominant in the optically thin plasma emission.

Radiative recombination continuum (free-bound emission)

The radiative recombination continuum is emitted when a free electron is captured into a vacant level of an ion. The energy of the emitted photon is the sum of the kinetic energy of the free electron and the binding energy of the electron, and since the kinetic energy of the free electrons is continuously distributed, the energy of the emitted photons is also continuous. Also, the spectrum shows an edge at the energy corresponding to the binding energy of the captured level.

Two-photon decay

If the angular momentum term of an excited state is the same as that of the ground state, the excited state is relaxed via the two-photon decay. This is because the photon has an angular momentum, and hence any transition that has no angular momentum change is prohibited. One of the examples is the transition from 1s2s $\left(^1S_0\right)$ to $(1s)^2$ $\left(^1S_0\right)$ in the He-like ion (Fig. 3.2). Normally, the electrons are transferred to the ground state (1s) after transition from the 2s orbit to higher orbits by a further collisional excitation. However, in the low-density limit, the probability of the second collision is small, so that the transition is made by emitting two photons from the 2s orbit to the 1s orbit (orange arrow in Fig.3.2). The sum of the energies of the two photons is equal to the energy difference between the 2s and 1s orbits, but the energy of each photon is not uniquely determined and thus a continuum spectrum is resulted.

3.7 Spectral model of X-ray emission

Given the elemental abundance and the rate of ionization, the expected emission spectrum can be calculated by summing the spectral emissivity of the various radiative processes. Many calculations have been performed on the expected radiation from such plasmas (Cox and Tucker

1969, Tucker and Koren 1971, Raymond et al. 1976, Raymond and Smith 1977, Summers and McWhirter 1979, Gaetz and Salpeter 1983, Mewe et al. 1985). The total cooling function from the optically thin thermal plasma is shown in Fig 3.3. The plasma is assumed to be in steady collisional ionization equilibrium with radiative cooling that balances the radiation-independent heating sources. It is also assumed to have cosmic elemental abundances (Allen 1973). The plotted quantity is the cooling function, which is calculated by the volume emissivity divided by the electron and proton densities, $\Lambda(T) \equiv \epsilon(T)/(n_e \cdot n_{\rm H})$. Below 2×10^7 K ($kT \lesssim$ 1.7 keV), the main cooling mechanism is line emission, with a peak around 10^5 K due to strong cooling from carbon and oxygen. Above 2×10^7 K, most ions are highly or fully ionized, and the thermal bremsstrahlung primarily determines the cooling rate of the plasma. At this temperature, heavy metals such as magnesium, silicon, sulfur, and iron are not fully ionized, and Kα lines from the helium-like and hydrogen-like ions of these elements can be seen clearly. Therefore, in this thesis, we look into the contribution of both thermal bremsstrahlung and line emission from plasmas with a temperature range from 0.1 keV to a few tens of keV.

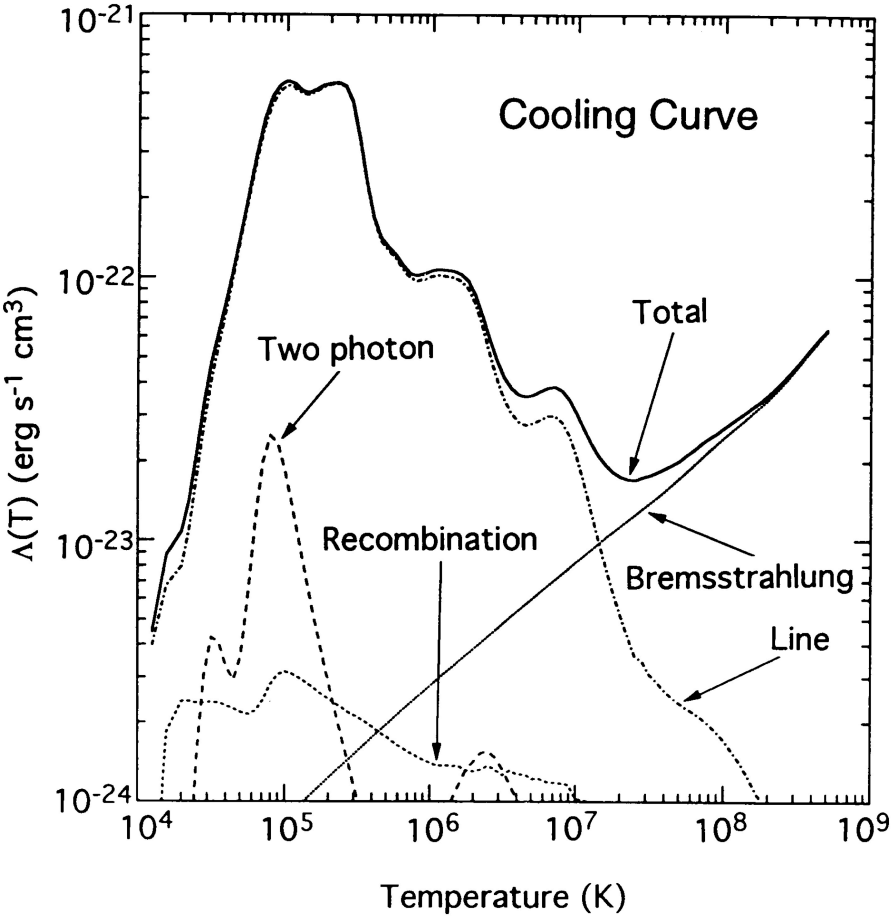

Fig. 3.3 Temperature dependence of cooling coefficient and its components for optically thin plasma of cosmic abundances (Gehrels and Williams 1993).

3.7.1 Multiple temperature plasma emission models

In dwarf novae, frictional heating of the disk matter forms a hot plasma in the boundary layer. The matter is cooled via optically thin thermal plasma emission and eventually settled onto the surface of the white dwarf. The appropriate model to describe such a plasma is the isobaric cooling flow model. This model was originally developed in order to model the X-ray spectra of cooling flows which was thought to operate in the central region of clusters of galaxies (Mushotzky and Szymkowiak 1988). The cooling flow spectrum is obtained by summing the isothermal plasma emission, described by the MEKAL model (Mewe et al. 1985, 1986, Kaastra 1992, Liedahl et al. 1995), weighted inversely by the cooling function at that temperature (Fabian 1994). The inverse weight indicates that the temperature with strong emissivity would have relatively short duration in the temperature excursion of the cooling process. As the gas with temperature T undergoes cooling under a constant pressure to $(T - dT)$ by the X-ray emission, the bolometric luminosity is given by,

$$dL_{cool} = n_e n_{\rm H} \Lambda(T) dT = \frac{5}{2} \frac{\dot{M}}{\mu m_H} k dT. \tag{3.8}$$

Here, $\dot{M}$ is the accretion rate, μ is the mean molecular weight whose value in the ionized gas is $\sim$ 0.62, and k is the Boltzmann constant. However, since $dL_{cool}(\nu) = n_e n_{\rm H} \epsilon_\nu(T) dV$, (where $\epsilon_\nu(T)$ is the spectral emissivity of the gas), the cooling spectrum is

$$L_{cool}(\nu) = \frac{5}{2} \frac{\dot{M}}{\mu m_{\rm H}} \int_0^{T_{max}} \frac{\epsilon_\nu(T) k dT}{\Lambda(T)}. \tag{3.9}$$

This model is commonly used as VMCFLOW in XSPEC (Arnaud 1996).

The other multiple temperature plasma model is CEVMKL. In the CEVMKL model, the differential emission measure is represented by a power-law function of temperature for the MEKAL model. The emission measure is often defined as

$$EM = \int n_e n_{\rm H} dV. \tag{3.10}$$

The spectrum is given by

$$d\,(EM) \propto \left(\frac{T}{T_{max}}\right)^{\alpha} d\,(\log T) \propto \left(\frac{T}{T_{max}}\right)^{\alpha-1} dT, \tag{3.11}$$

where α is a power-law index that represents the deviation from the isobaric flow.

The VMCFLOW and CEVMKL models include emission lines from 13 different elements: C, N, O, Ne, Na, Mg, Al, Si, S, Ar, Ca, Fe and Ni. These lines are produced by the excitation processes: electron impact, two-electron recombination, and inner-shell excitation. The intensity of the line determines the abundance of the corresponding element. Figure 3.4 shows two

examples of CEVMKL model with the maximum temperature of 1 keV and 20 keV. As the temperature of the plasma increases, light elements such as C, and N are completely ionized and are unable to emit lines. We can determine the plasma temperature both by the shape of the continuum emission and by the relative intensity of the emission lines from each element.

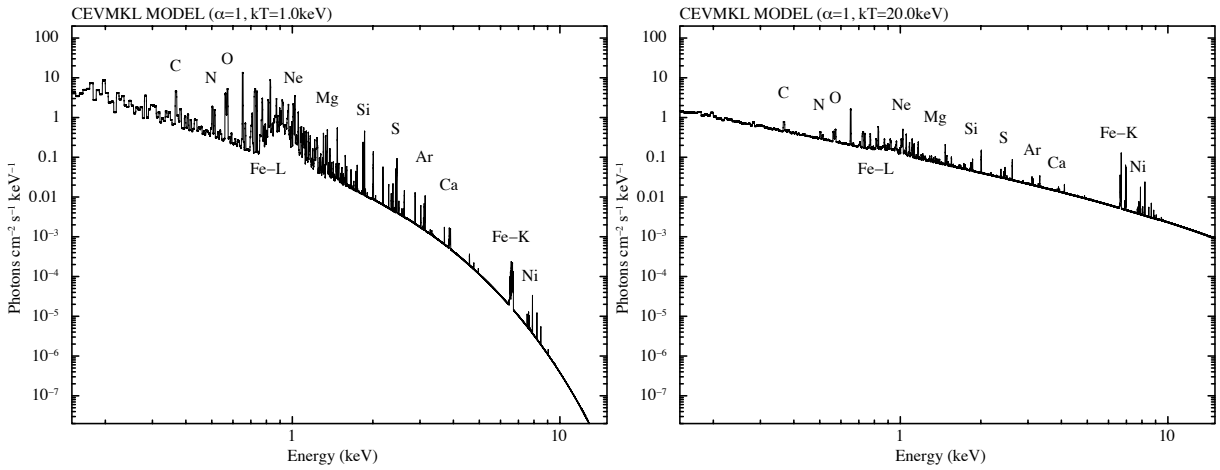

Fig. 3.4 Spectra of multiple temperature model (CEVMKL) with maximum temperature of 1.0 keV (left) and 20.0 keV (right).

3.7.2 Reflection of the Plasma emission

Since the boundary layer plasma is formed in contact with the white dwarf surface, a significant fraction of its X-rays irradiates cool material, such as the accretion disk and the white dwarf surface, and some of these X-rays are reflected off into space. The reflection rate is energy-dependent: in the low energy side, the scattering probability decreases with decreasing energy due to photoelectric absorption by the cold matter. In the high energy side, on the other hand, the number of reflected photons decreases due to Compton down-scattering and a decrease in the scattering cross-section. The reflection spectra thus produced have a broad "bump" structure centered at around 30 keV. In addition, the reflection spectra below 10 keV show significant features of iron K-edge absorption and associated Fe Kα fluorescence lines whose energy and intensity are a function of the ionization state and iron abundance of the reflecting matter (Lightman and White 1988, George and Fabian 1991, Matt et al. 1991). George and Fabian (1991) theoretically calculated the equivalent width of the fluorescent iron Kα line, assuming the point source to be on an infinite slab ($\Omega = 2\pi$). The equivalent width depends on the following parameters: inclination angle i, between the normal of the reflector and the observer's line of sight, photon index of the spectrum of the illuminating point source, and iron abundance of the reflecting surface. For the model spectrum, we adopt the XSPEC model REFLECT (Magdziarz and Zdziarski 1995). Figure 3.5 shows an example of the spectrum of a dwarf nova. It consists of three main components: (1) a multi-temperature plasma component

with a maximum temperature of 20 keV and $\alpha = 0$, (2) its reflection from the white dwarf (and the accretion disk) with a solid angle 2π and an inclination angle 60°, and (3) the fluorescent iron emission line at 6.4 keV.

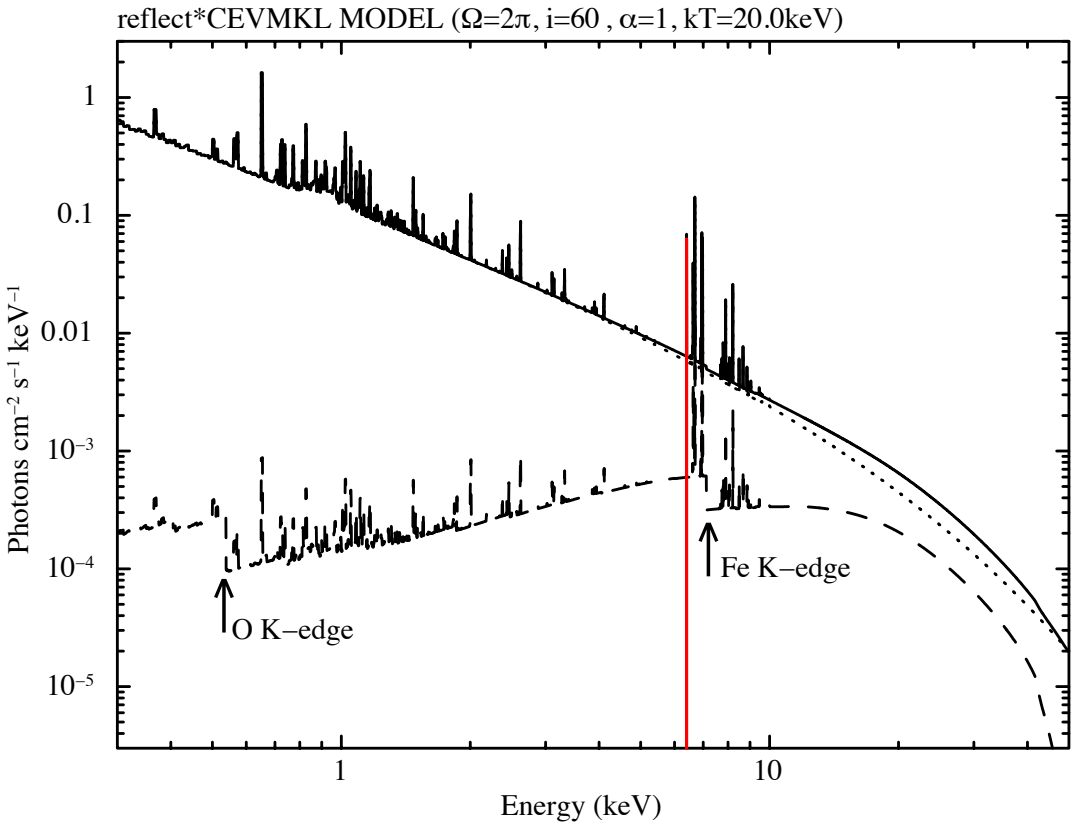

Fig. 3.5 Example of the energy spectra of dwarf novae (black solid line). Dotted line shows the plasma emission. Dashed line shows the reflection, and red solid line indicates the iron fluorescence line at 6.4 keV.

3.7.3 Definition of Solar Abundances

The XSPEC package has some sets of solar abundance tables ready for use along with the plasma emission and photoelectric absorption models. Here we adopt Anders and Grevesse (1989) values for the solar abundances of the elements throughout this thesis. Anders and Grevesse (1989) compiled the abundance table based on the C1-type chondrites and solar photosphere with critical examination of the differences between them. The solar abundance values are shown in Table. 3.2.

Table 3.2 Definition of solar abundance in relative to hydrogen number at Anders and Grevesse (1989).
https://heasarc.gsfc.nasa.gov/xanadu/xspec/manual/node117.html

Element	Relative abundance [$/Z_{\rm H}$]
H	1.00
He	9.77×10^{-2}
C	3.63×10^{-4}
N	1.12×10^{-4}
O	8.51×10^{-4}
Ne	1.23×10^{-4}
Na	2.14×10^{-6}
Mg	3.80×10^{-5}
Al	2.95×10^{-6}
Si	3.55×10^{-5}
S	1.62×10^{-5}
Ar	3.63×10^{-6}
Ca	2.29×10^{-6}
Fe	4.68×10^{-5}
Ni	1.78×10^{-6}

CHAPTER 4

Instrument

In this thesis, we utilized three different X-ray satellites, *XMM-Newton*, *Suzaku* and *NICER*. We introduce the basic properties and performance of these satellites.

4.1 *XMM-Newton*

X-ray Multi-Mirror Mission "*XMM-Newton*" (Jansen et al. 2001) was launched by the European Space Agency (ESA) on December 10th 1999. The satellite was thrown into the highly elliptical orbit, with a perigee of 6,000 km and an apogee of 115,000 km with a period of 47.88 hours (Fig.4.1). In this orbit, the satellite can observe any given target continuously for a long time because the time that the target is hardly eclipsed by the earth. Also, the minimum satellite elevation that *XMM-Newton* can observe is 46,000 km, but only if the radiation background is low enough. To make observation in the X-ray band of 0.1–15 keV, *XMM-Newton* has three X-ray mirrors and X-ray CCD cameras. In addition to the CCD cameras, *XMM-Newton* is equipped with a grating spectrometer (Reflective Grating Spectrometer: RGS). However, we do not explain the RGS because we do not use any data taken with the RGS.

4.1.1 X-ray mirror

X-rays are totally reflected when incident on the reflector surface at a grazing angle smaller than the critical angle ($\sim 1^\circ$). X-ray mirrors of *XMM-Newton* have adopted the Wolter type-I optic, in which the primary and secondary mirrors are a paraboloid and a hyperboloid, respectively (Wolter 1952) (see Fig.4.2). The optic collects the X-rays by the total reflection once on each mirror stage. In this mirror, 58 reflectors in total, whose substrates are as thin as 0.47–1.07 mm, are nested confocally and coaxially. The reflector uses a nickel substrate coated with gold. The weight and diameter of one mirror module are 440 kg and 70 cm, respectively. There are three identical X-ray mirrors with a focal length of 7.5 m. The ground calibrations of X-ray mirrors were made at the PANTER test facility of the Max-Plank-Institut für extraterrestrische Physik (Gondoin et al. 1998*a*,*b*). The angular resolution estimated from half energy width of the Point-Spread Function (PSF)s is $\sim$ 15 arc seconds. The effective areas are typically 1475 cm^2 at 1.5 keV and 940 cm^2 at 6.0 keV.

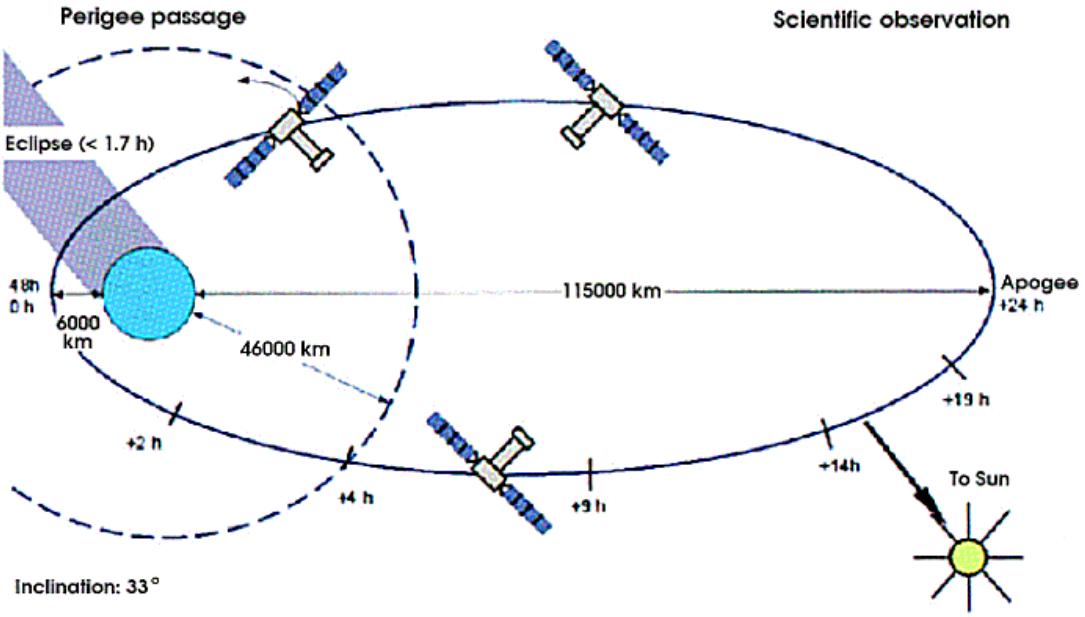

Fig. 4.1 Elliptical orbit of *XMM-Newton*.
`https://xmm-tools.cosmos.esa.int/external/xmm_user_support/documentation/uhb/orbit.html`

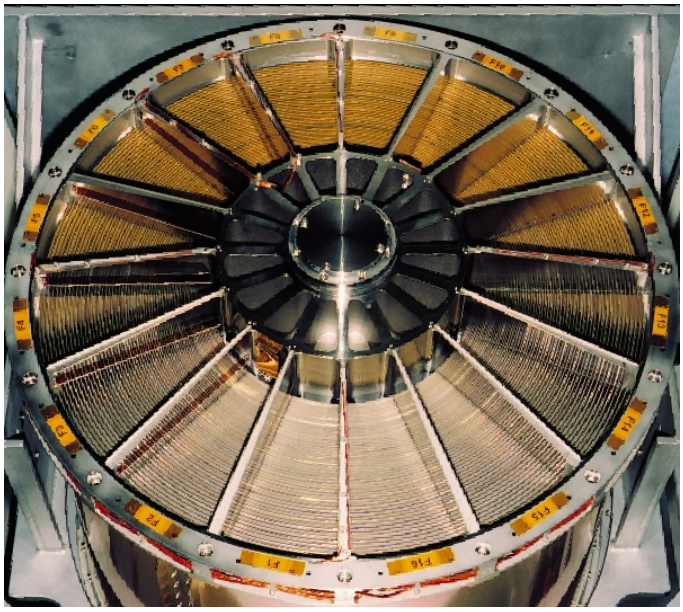

Fig. 4.2 X-ray mirror of *XMM-Newton*.
`https://www.cosmos.esa.int/web/xmm-newton/technical-details-mirrors`

4.1.2 European Photon Imaging Camera (EPIC)

XMM-Newton has three X-ray CCD cameras, which are called European Photon Imaging Camera (EPIC). All EPIC CCDs operate in the photon counting mode with a field of view of 30 arc min in an energy range from 0.2 to 12 keV. The intrinsic energy resolution of the pixels allows for simultaneous imaging and non-dispersive spectroscopy.

EPIC are composed of two different type CCD cameras: Metal Oxide Semiconductor (MOS) CCD arrays (Turner et al. 2001) and CCD camera called pn (Strüder et al. 2001). EPIC-MOS consists of 7 front-illuminated CCDs (Fig. 4.3). The central chip (CCD1) is at the focal point on the optical axis of the mirror. *XMM-Newton* is equipped with two MOS cameras, called MOS1 and MOS2. Each CCD has a format of 600 $\times$ 600 pixels with a size of 40 μm. To minimize the dead space, adjacent CCDs are stepped by about 1 mm to overlap by 300 μm (see Fig.4.3). In *XMM-Newton*, the part of focused X-ray from the mirror to the MOS is intercepted by the Reflection Grating Assembly (RGA). Thus, MOS receives 44 % of the light collected by the mirror, and the rest is collected by the RGS.

EPIC-pn consists of 12 back-illuminated CCDs (Fig.4.4). Three pn-CCDs are combined to form quadrants. Each CCD has a format of 200 $\times$ 64 pixels with a size of 150 μm. However, the first 12 rows at the readout-node are not transmitted to ground, the total imaging area of EPIC-pn is 376 $\times$ 384 pixels.

4.1.3 Operating mode of EPIC

The EPIC-MOS and pn allow several modes of data acquisition depending on the brightness of the celestial body and the purpose of the observation. The characteristics of the modes are summarized in Table 4.1. Note that in the case of MOS the outer 6 CCDs remain in the standard full-frame imaging mode while the central MOS CCD1 can be operated separately. Thus all CCDs are gathering data all the time, independent of the choice of the operating mode. The pn camera CCDs can be operated in common modes in all quadrants for Full Frame, Extended Full Frame and Large Window mode, while just one single CCD (CCD number 4 in Fig. 4.4) is operated for Small Window, Timing and Burst mode. In timing mode, imaging is made only in one dimension, along the column axis. Along the row direction, data from a predefined area on the CCD chip are collapsed into a one-dimensional row to be read out at high speed.

4.1.4 Filters and effective area

Because the EPIC cameras are sensitive to infrared, visible, and ultraviolet light as well as X-ray, the cameras have an aluminized optical blocking filter in front of the cameras. To reduce the contamination, each EPIC camera is equipped with three separate sets of filters: thick, medium, and thin. The thick filter is made of polypropylene with a thickness of 3300 Å with 1100 Å of aluminum and 450 Å of tin deposited on the film. This filter is used when the expected contaminant flux from the target affects the energy scale and energy resolution of the

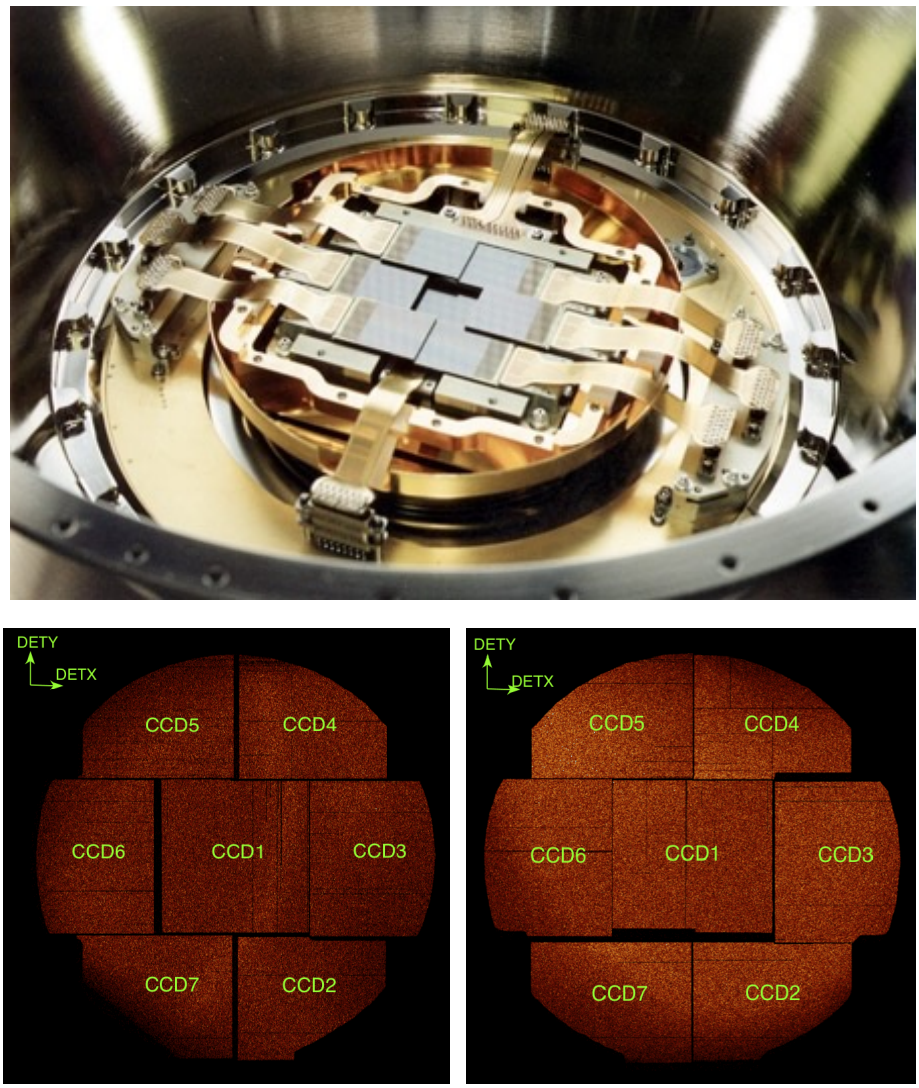

Fig. 4.3 (Top) Photo of EPIC-MOS camera.
`https://www.cosmos.esa.int/web/xmm-newton/technical-details-epic`
(Bottom) Layout of EPIC-MOS camera for MOS1 (left) and MOS2 (right).
`https://xmm-tools.cosmos.esa.int/external/xmm_user_support/documentation/uhb/moschipgeom.html`

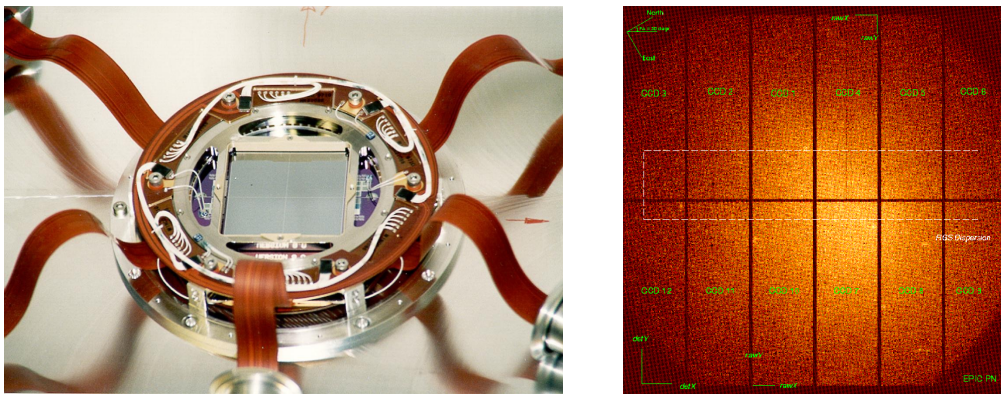

Fig. 4.4 (Left) Photo of EPIC-pn camera.
`https://www.cosmos.esa.int/web/xmm-newton/technical-details-epic`
(Right) Layout of EPIC-pn camera.
`https://xmm-tools.cosmos.esa.int/external/xmm_user_support/documentation/uhb/pnchipgeom.html`

Table 4.1 Chastaristics of EPIC operating modes.

EPIC-MOS (one CCD) 1 pixel = 1.1”	Time resolution	Live time † [%]	Max count-rate at point source [s^{-1}]
Full Frame (600 × 600)	2.6 s	100.0	0.50
Large Window (300 × 300)	0.9 s	99.5	1.5
Small Window (100 × 100)	0.3 s	97.5	4.5
Timing (100 × 600)	1.75 ms	100.0	100
EPIC-pn **1 pixel = 4.1”**	**Time resolution**	**Live time †** **[%]**	**Max count-rate** **at point source [s^{-1}]**
Full Frame (376 × 384)	73.4 ms	99.9	2
Extended Full Frame (376 × 384)	199.1 ms	100.0	0.3
Large Window (198 × 384)	47.7 ms	94.9	3
Small Window (63 × 64)	5.7 ms	71.0	25
Timing (64 × 200)	0.03 ms	99.5	800
Burst (64 × 180)	7 μs	3.0	60000

† Ratio between the time interval during which the CCD is collecting X-ray events (integration time, including time needed to shift events towards the readout) and the frame time (which in addition includes time needed for the readout of the events).

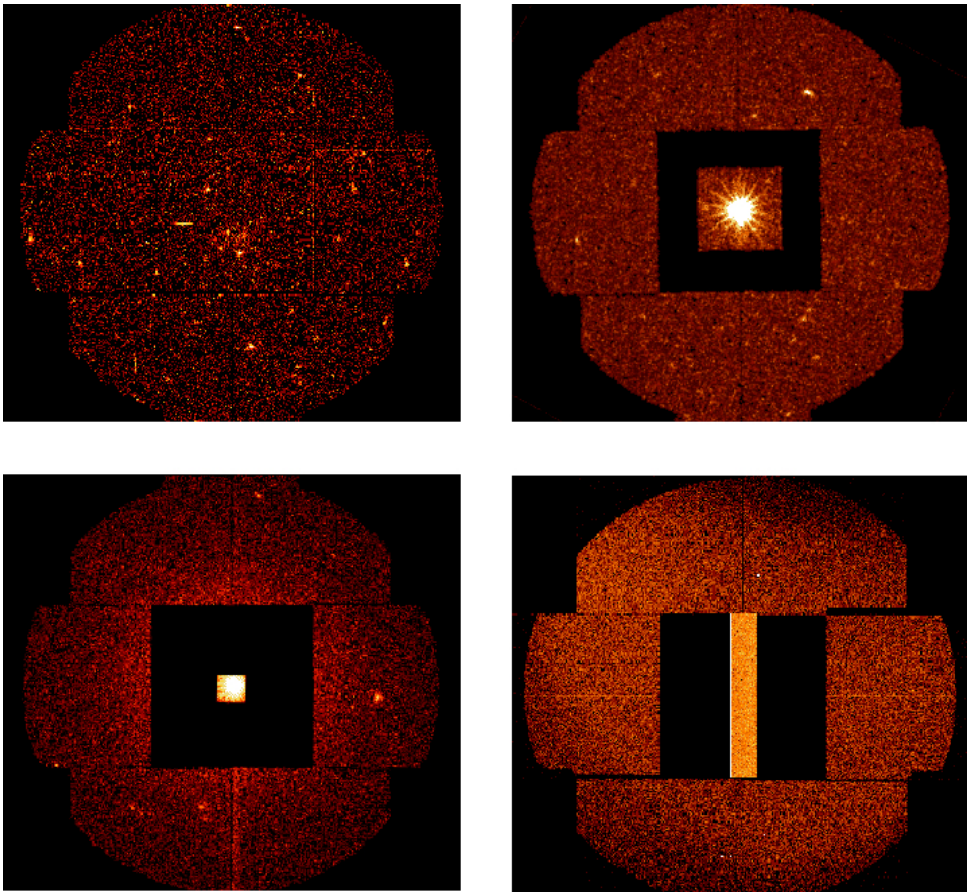

Fig. 4.5 Images with different operating modes for EPIC-MOS. Top left: Full Frame mode; top right: Large Window mode; bottom left: Small Window mode, and bottom right: Timing mode. (SOC 2020)

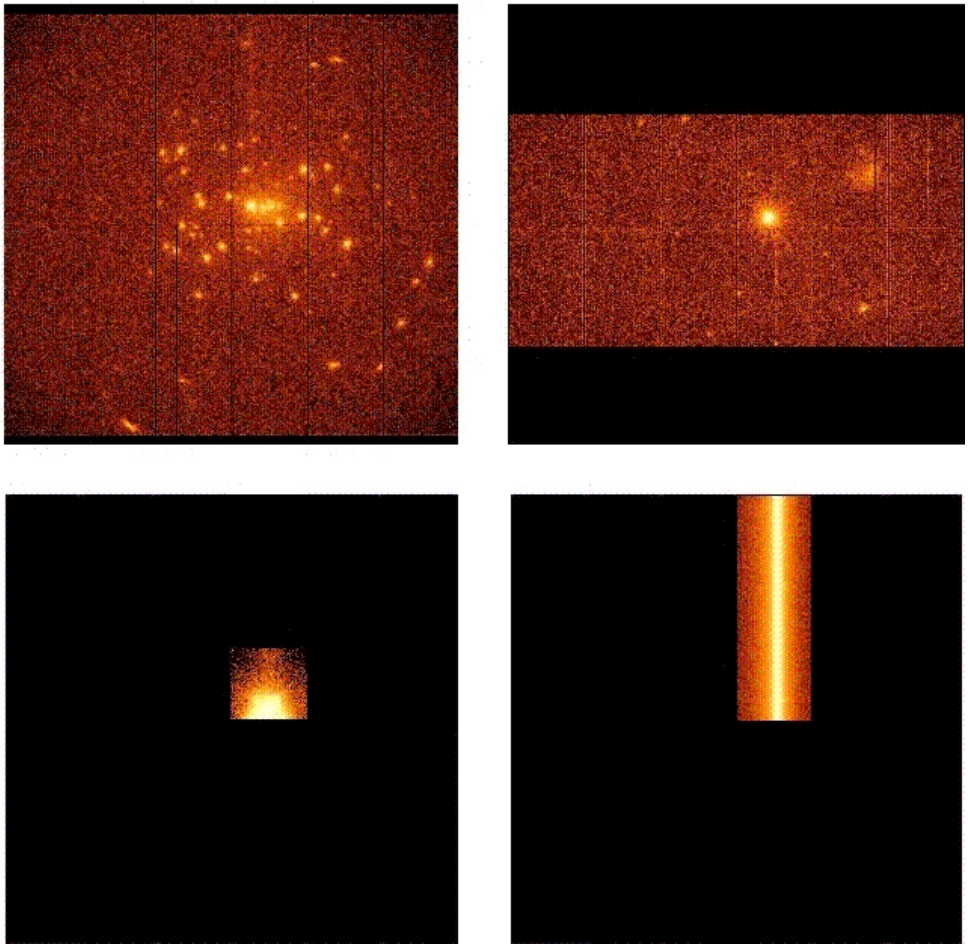

Fig. 4.6 Images with different operating modes for EPIC-pn. Top left: Full Frame and Extended Full Frame mode; top right: Large Window mode; bottom left: Small Window mode, and bottom right: Timing mode. (SOC 2020)

EPIC. It is recommended to use this filter if the apparent optical magnitude m_V of the target is in the range +1 to +4 for the MOS and -2 to +1 for the pn. Medium filter is made of polyimide film with a thickness of 1600 Å with 800 Å aluminum deposit of one side. This is necessary to prevent optical contamination from bright point sources whose m_V is in the range +6 to +9. Thin filter is made of the same material as medium filter, but has an aluminum deposit of 400 Å. This is limited to be used for point sources whose optical brightness is about 12 magnitude darker than the target to be observed through the thick filter. Figure 4.7 shows the effective area of both types of EPIC camera using the different filters. The observer need to select the filter which maximizes the scientific return from the target of interest.

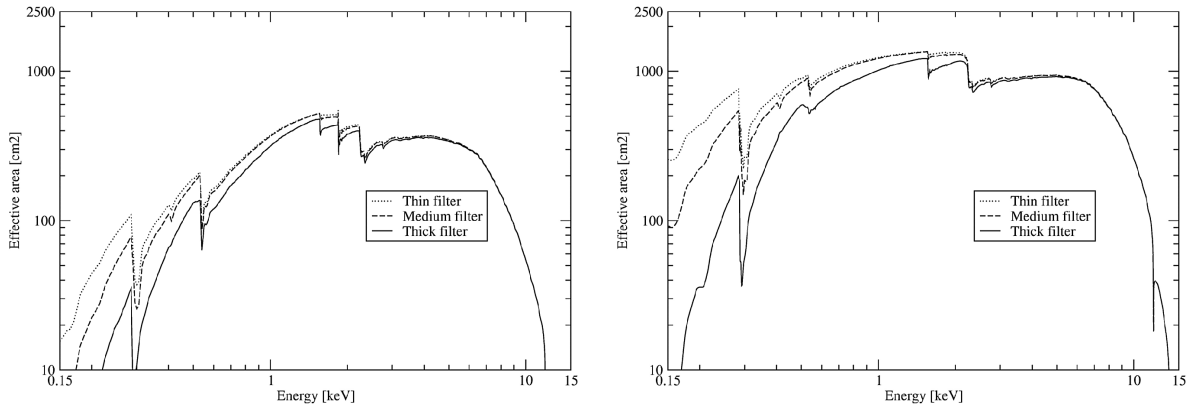

Fig. 4.7 EPIC effective area when applying different filters (Left : MOS, Right : pn). `https://www.cosmos.esa.int/web/xmm-newton/technical-details-epic`

4.2 *Suzaku*

The Japanese 5th X-ray astronomy satellite "*Suzaku*" (Mitsuda et al. 2007) was launched by the Institute of Space and Astronautical Science of Japan Aerospace Exploration Agency (ISAS/JAXA) on July 10th, 2005. The satellite was thrown into a circular orbit with an altitude of 568 km, an inclination of 31.9 degrees for with a period of 96 minutes. Compared to *XMM-Newton*, one of the major features is that the orbit is enveloped by the earth's magnetosphere, and hence the detector noise caused by cosmic rays can be kept low. *Suzaku* covers a wide energy band (0.2–700 keV) with high sensitivity. The soft X-ray band of 0.2–12 keV is covered with four soft X-ray mirrors and X-ray imaging spectrometers. The hard X-ray band (10–600 keV) is observed with a hard X-ray scintillating instrument. The science operation of *Suzaku* is terminated on August 26, 2015.

4.2.1 X-ray Telescope (XRT)

The X-ray Telescope (XRT) (Serlemitsos et al. 2007) onboard *Suzaku* is an X-ray mirror with an aperture of 40 cm and a weight of 19.5 kg (see Fig.4.8). There are four X-ray mirrors with a focal length of 4.75 m. The XRT is of the Wolter type-I optic and consists of 175 pairs of reflectors being nested confocally and coaxially. The reflector uses an aluminum substrate with a mirrored surface formed by the replica method. The substrate thickness is 155 μm. The angular resolution of the XRTs ranges from 1.8 to 2.3 arc min expressed in half power diameter. The effective areas are typically 440 cm^2 at 1.5 keV and 250 cm^2 at 8.0 keV.

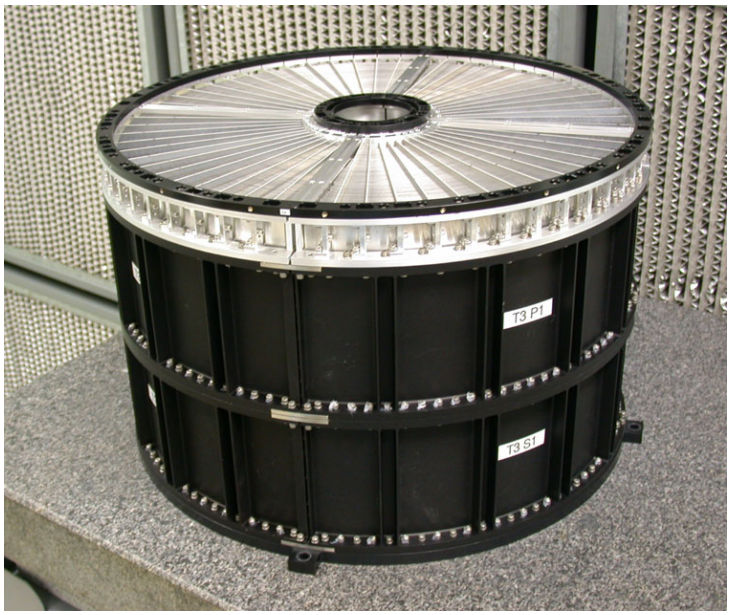

Fig. 4.8 XRT : X-ray mirror of *Suzaku*.
`https://heasarc.gsfc.nasa.gov/docs/suzaku/gallery/instruments/xrt.html`

4.2.2 X-ray Imaging Spectrometer (XIS)

Suzaku has four X-ray CCD cameras which are called the X-ray imaging spectrometer (XIS) (Koyama et al. 2007). Each CCD has a format of 1024$\times$1024 pixels with a size of 24 μm, and covers a square area with 17.8 arc min on a side. The four XISs are called XIS0, 1, 2, and 3, respectively, with XIS1 being a back-illuminated CCD and the others being front-illuminated CCDs. The effective area of the XRT+XIS system is 340 cm^2 (FI) and 390 cm^2 (BI) at 1.5 keV and 350 cm^2 (FI) and 100 cm^2 (BI) at 8.0 keV (Fig.4.9). Due to an apparent micrometeorite impact, the observation of XIS2 had been impossible since November 9, 2006 (Dotani and Suzaku Team 2008). For the same reason, a part of XIS0 had become unusable since June 23, 2009 (Fig.4.10).

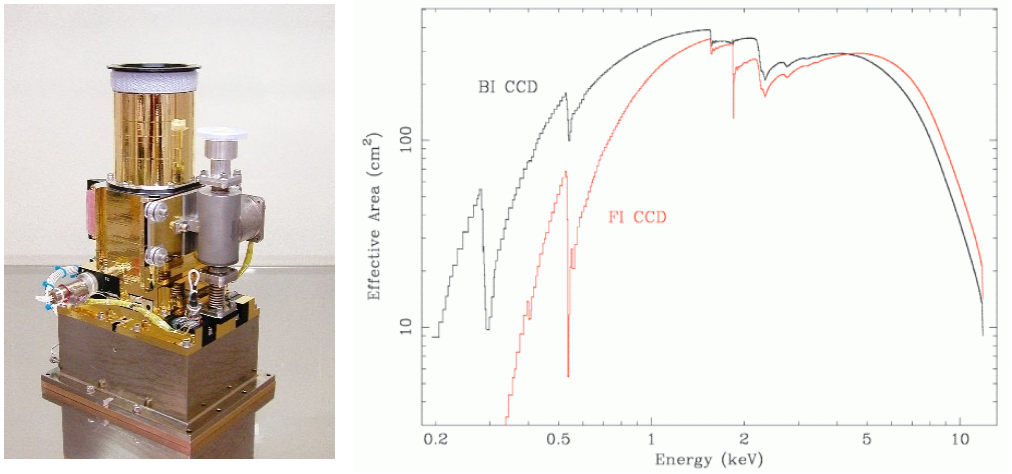

Fig. 4.9 (Left) Photo of X-ray imaging spectrometers (XIS).
`https://heasarc.gsfc.nasa.gov/docs/suzaku/gallery/instruments/xis.html`
(Right) Effective area of XRT+XIS system.
`https://heasarc.gsfc.nasa.gov/docs/suzaku/gallery/performance/xis_area.html`

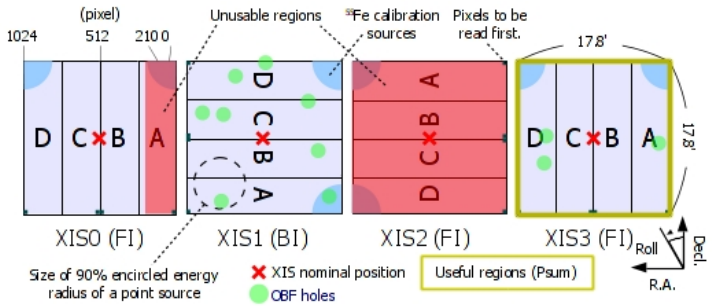

Fig. 4.10 Field of view of XIS.
`https://heasarc.gsfc.nasa.gov/docs/suzaku/prop_tools/suzaku_td/node10.html`

4.2.3 Hard X-ray Detector (HXD)

The *Suzaku* is equipped with the non-imaging hard X-ray detector (HXD) (Takahashi et al. 2007). The background from cosmic rays and that intrinsic to the detector are larger in the hard X-ray band, and it is very important to reduce these backgrounds. The structure of the HXD is shown in Fig.4.11. There are 16 well-type phoswich counters (Well Unit) surrounded by 20 Bismuth Germanate (BGO) crystal anti-counters (Anti Unit). The main detector of the Well Unit consists of a PIN silicon diodes (2mm thick) and a Gadolinium Silicate (GSO) scintillator (5mm thick) overlaid. X-rays with the energy of 10–50 keV are detected in a PIN diode, while X-rays with the energy range of 40–700 keV are detected in the underlying GSO, which penetrate the PIN. A deep well-shaped BGO crystal scintillator is used for the shield around the main detector. Background (γ-rays and charged particles) and X-rays incident from outside the field of view are efficiently removed by anti-coincidence measurements of the main detector and BGO.

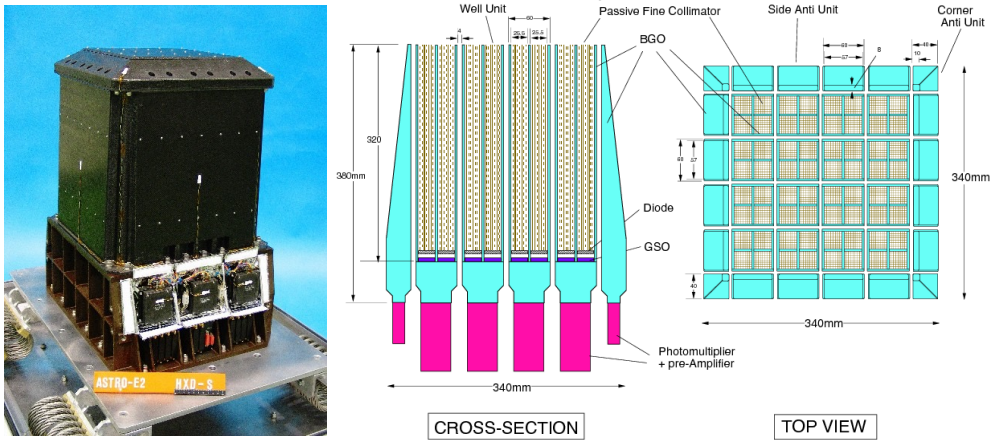

Fig. 4.11 (Left) Photo of hard X-ray detector (HXD).
`https://heasarc.gsfc.nasa.gov/docs/suzaku/gallery/instruments/hxd.html`
(Right) Schematic picture of HXD.
`https://heasarc.gsfc.nasa.gov/docs/suzaku/analysis/abc/node10.html`

4.3 *NICER*

The Neutron star Interior Composition Exploler "*NICER*" (Arzoumanian et al. 2014) was launched by NASA the on June 3rd, 2017, and mounted on International Space Station (ISS) on June 16th, 2017. Major characteristic of *NICER* is high-precision time-resolved spectrometry in the 0.2–12 keV X-ray band.

4.3.1 X-ray Timing Instrument (XTI)

The X-ray timing instrument (XTI) of *NICER* is a non-imaging soft X-ray telescope. The schematic view is shown in Fig.4.12. It consists of 56 pairs of X-ray concentrators optics (XRC) (Okajima et al. 2016) and Focal Plane Module (FPM) (Gendreau et al. 2016). The XRCs focus X-rays from a cosmic ray source onto the FPM with a single reflection. Each XRC consists of 24 nested, gold-coated, parabolic thin foil mirrors, and the weigh of each XRC is 325 g. Its focal length is 1.085m and the diameter is 105 mm. Grazing incident angles to individual shells range from 0.4 to 1.4 deg.

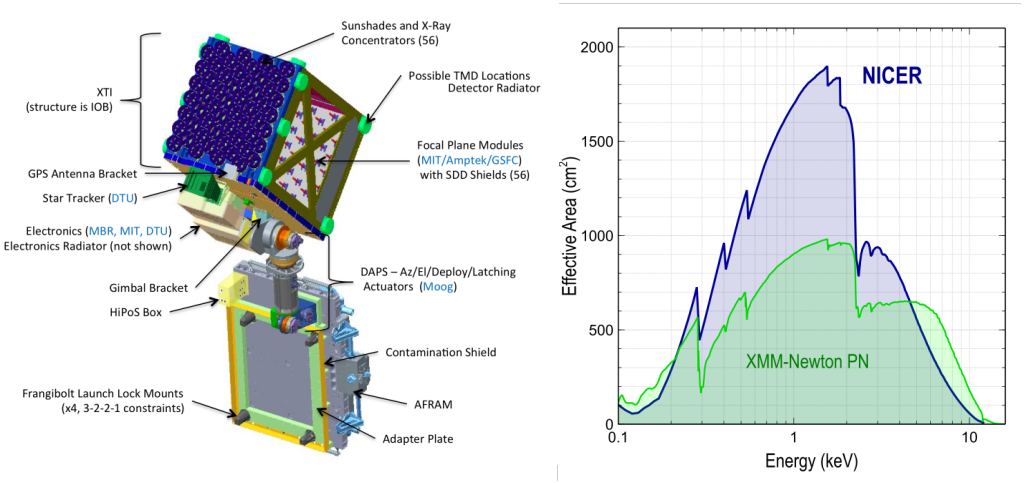

Fig. 4.12 (Left) Schematic picture of NICER.
`https://heasarc.gsfc.nasa.gov/docs/nicer/mission_guide/`
(Right) Effective area of XTI.
`https://heasarc.gsfc.nasa.gov/docs/nicer/nicer_tech_desc.html`

Each FPM consists of a 500 micron thick Amptek Silicon Drift Detectors (SDD) and a Thermo Electric Cooler (TEC) mounted underneath it (Prigozhin et al. 2012). The SDD is a soft X-ray spectroscopy sensor. The active area of each FPM has an aperture of 2mm in diameter. This was achieved by minimizing diffuse-sky background and source confusion, while improving the timing performance of the SDD. The instrument is capable of providing spectral information in addition to the exact timing of each photon detected. The absolute time resolution is less than 300 nano sec and the spectral resolution is 85 eV at 1 keV, and 137 eV at 6 keV. The arrangement of the FPMs at the XTI backplane is shown in Fig 4.13. The 8 FPMs are controlled by one Measurement and Power Unit (MPU), and are labeled 0-7. In addition, the 7 MPUs are labeled 0-6, and each module is given a science detector ID (DET_ID) that combines the MPU number at the tens place and the FPM number at the ones place. Note that 4 FPMs (DET_IDs are 11, 20, 22, and 60) out of 56 have been inactive since launch.

The effective area of the XTI system is $\sim$1900 cm^2 at 1.5 keV and 600 cm^2 and at 6.0 keV.

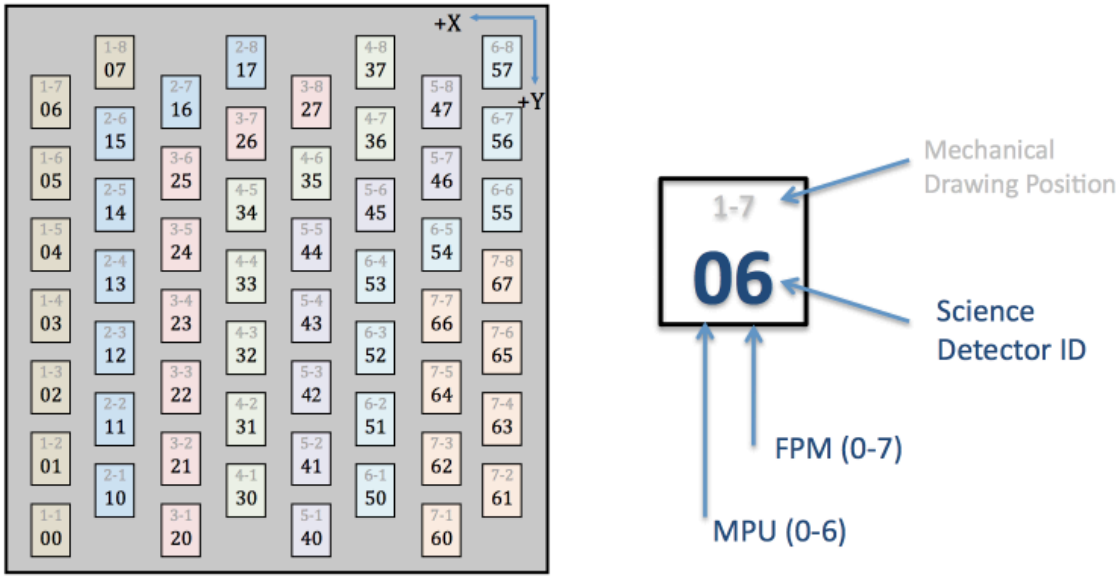

Fig. 4.13 Arrangement of FPMs on XTI backplane.
`https://heasarc.gsfc.nasa.gov/docs/nicer/mission_guide/`

CHAPTER 5

Observation and Data Reduction

We have utilized data of the dwarf novae during quiescence taken with *XMM-Newton*, *Suzaku*, and *NICER*. In this chapter, we describe the observation log of each satellite and the data reduction procedures we applied.

5.1 *XMM-Newton* observations of DNe in quiescence

The data observed by *XMM-Newton* are summarized in the XMM-Newton Science Archive (XSA).[1] Of all the DN data available from the XSA by September 2020, we selected the objects listed in the Ritter and Kolb (2003) Edition 7.24, which is a catalog of cataclysmic binaries, low-mass X-ray binaries, and related objects. We then confirmed the optical state of each observation through inspection of American Association of Variable Star Observers (AAVSO)[2] visible light curves and identified the quiescent DN data to be analyzed in this study. Summary of the observations is shown in Table 5.1. The distance to each object was calculated from the parallax obtained by the *Gaia* collaboration (Gaia Collaboration et al. 2018).

We have used EPIC-MOS and pn data and have screened them with `evselect` (version 3.68), which is included in the Science Analysis Software (SAS) XMMSAS_20190531_1155-18.0.0 provided by ESA[3]. In determining the region with the highest signal-to-noise ratio (S/N), we used data above the 5 keV energy band, where Fe emission lines dominate. The methods of determining a photon-collecting region are different, depending on the operating mode. First, we describe the data in Full Frame and Large Window mode. An observation example is shown in Fig. 5.1. We set a circular region centered on the image brightness peak and checked all counts contained in the region every 5 arc seconds in radius over a radius of 20-75 arc seconds. Background event was extracted in annulus and the total counts in the region were checked by varying the inner and outer radii from the source integration region radius to 150 arc seconds in every 5 arc seconds in radius. To improve the statistics of the data, we used the results when the area of the background is more than three times as large as that of the source integration region.

[1] `http://nxsa.esac.esa.int/nxsa-web/`
[2] `https://www.aavso.org`
[3] `https://www.cosmos.esa.int/web/xmm-newton/sas`

Table 5.1 System parameter of dwarf novae observed by *XMM-Newton*.

Object	$M_{\rm WD}$ ($M_\odot$)	$P_{\rm orb}$ (hr)	Inclination (deg)	$D^\dagger$ (pc)
U Gem type				
EY Cyg	1.10 ± 0.09	11.02	14 ± 1	647.49 ± 8.56
RU Peg	1.06 ± 0.04	8.99	43	276.52 ± 3.40
SS Cyg	1.19 ± 0.02[a]	6.60	51 ± 5	114.62 ± 0.64
SS Aur	1.08 ± 0.40	4.39	38 ± 16	259.80 ± 2.78
U Gem	1.20 ± 0.05	4.25	69.7 ± 0.7	93.35 ± 0.26
AB Dra	1.03[b]	3.65	81[b]	409.48 ± 4.45
Z Cam type				
WW Cet	0.83 ± 0.16	4.22	54 ± 4	217.98 ± 2.22
SU UMa type				
YZ Cnc	0.82 ± 0.08	2.08	38 ± 3	239.54 ± 2.66
TY PsA	–	2.02	65[b]	184.14 ± 2.22
SU UMa	0.8[b]	1.83	44[c]	220.52 ± 1.39
VW Hyi	0.63 ± 0.15[d]	1.78	60 ± 10	53.96 ± 0.06
V1504 Cyg	–	1.67	$40 \sim 60$[e]	527.08 ± 13.30
QZ Vir	0.35[b]	1.45	65 ± 19	127.97 ± 1.12
WZ Sge	0.85 ± 0.04	1.36	77 ± 2	45.13 ± 0.08
GW Lib	0.84 ± 0.02	1.28	11.2 ± 0.4	112.79 ± 1.05
V893 Sco	0.89	1.82	74.2[f]	124.13 ± 0.80
Z Cha	0.59[b]	1.79	81.8 ± 0.1	115.44 ± 1.65
HT Cas	0.61 ± 0.04	1.77	81 ± 1	141.40 ± 1.25
OY Car	0.64 ± 0.04	1.51	83.3 ± 0.2	90.79 ± 0.25

Unless noted otherwise, the parameters are from "Catalogue of Cataclysmic Binaries, Low-Mass X-Ray Binaries, and Related Objects Edition 7.24" (Ritter and Kolb 2003).

† Gaia Collaboration Data release 2 (Gaia Collaboration et al. 2018).

[a] From Friend et al. (1990)

[b] From Urban and Sion (2006)

[c] From Warner (1987)

[d] From Schoembs and Vogt (1981)

[e] From Howell et al. (2013)

[f] From Mukai et al. (2009)

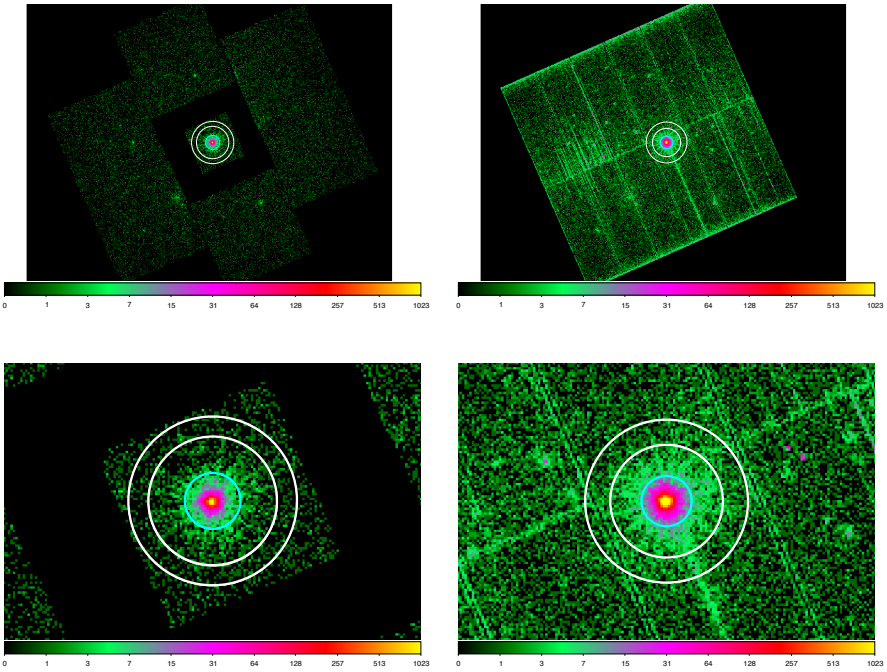

Fig. 5.1 Image of QZ Vir obtained with EPIC-MOS1 in Large Window mode (left panel) and EPIC-pn in Full Frame mode (right panel). Upper panels show overall view, and lower panels show enlarged view centered on image brightness peak. Cyan circles show source area, and white annuli show background area.

Next, we described the data in Small Window mode (Fig. 5.2). In the EPIC-MOS data, we used only CCD1 (see the bottom panel of Fig. 4.3). Source events was extracted in a circular region and total counts were checked in every 2.5 arc seconds from a radius of 10 arc seconds until it reaches the edge of the window. The background events were extracted from the area out of the source integration region but within the window. To improve the statistics of the data, the area of the background is set more than twice as large as that of the source. The source integration region of the EPIC-pn was checked in every 2.5 arc seconds in radius from 15 arc seconds until it reaches the edge of the window. The background event was extracted from a rectangular area (64 pixels on the long side) that does not include the source events.

Finally, we describe data selection method of Timing mode (Fig. 5.3). The source event was extracted from a rectangle centered on the highest count line (600 pix on the long side for EPIC-MOS and 200 pix for EPIC-pn) and the width of the short side was expanded, stepped by 2 pixels to seek for the best S/N region. The background events of EPIC-MOS were extracted from a region out of CCD1 but within a circle centered at (DETX, DETY) = (0, 0) with a radius best for the S/N ratio for each source in the range of 480-600 arc seconds stepped by 5 arc seconds. The background event of EPIC-pn was extracted from two rectangles (200 $\times$ 17 pixels) sandwiching the source area.

We then produced the event file without the source area based on the best S/N background region thus obtained into `espfilt` (version 2.7.1) which is provided by SAS, and created a background light curve of 2.5–12.0 keV and a Good Time Interval file from the light

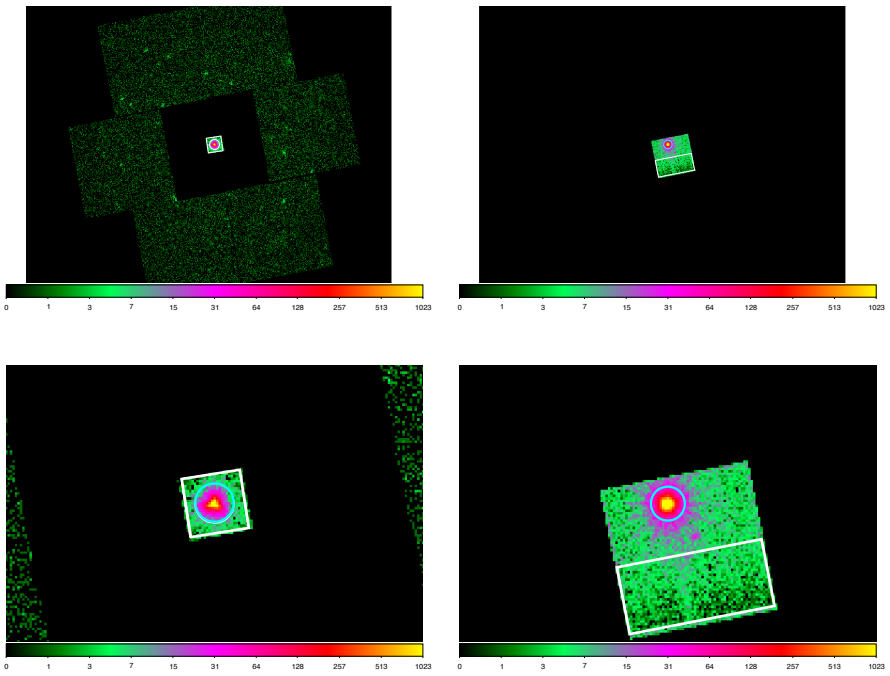

Fig. 5.2 Image of U Gem obtained with EPIC-MOS2 (left panel) and EPIC-pn (right panel) in Small Window mode. Upper panels show overall view, and lower panels show enlarged view centered on image brightness peak. Cyan circles show source area, and white rectangles show background area.

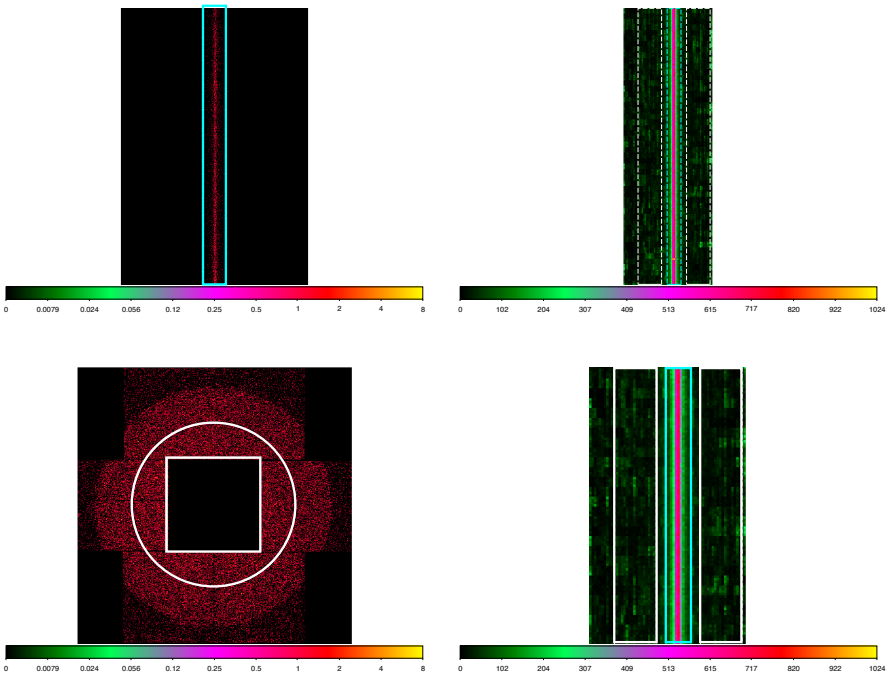

Fig. 5.3 Image of SS Cyg in 2001 obtained with EPIC-MOS1 (left panel) and EPIC-pn (right panel) in Timing mode. Upper left panel shows overall view of CCD1 in EPIC-MOS1, and lower left panel shows overall view of other CCDs. Upper right panel shows overall view of CCD4 in EPIC-pn, and lower right panel shows enlarged view of it. Cyan rectangles show source area, and areas surrounded by white line show background.

curve. To obtain spectra, we filtered PATTERN<=12 and #XMMEA_EM for EPIC-MOS and PATTERN<=4 and FLAG == 0 for EPIC-pn. Note that the out-of-time events has been subtracted for all EPIC-pn spectra. The operating mode of each observation and its exposure time are summarized in Table 5.2 and 5.3. AB Dra in June 2002 was not observed with EPIC-MOS. Due to a micrometeoritic impact, a hot column has appeared around RAWX = 318 in MOS1 Timing mode since March 2005. We did not use SS Cyg in 2018 for our analysis because the source event is at RAWX = 317. In addition, EPIC-pn data for SS Cyg in 2018 suffered significant pile up and therefore were not used.

In preparation for spectral analysis, we have made redistribution matrix files (RMFs) of the EPIC-MOS and pn with the software `rmfgen` (version 2.8.1). With the RMF thus made, we have created ancillary response files (ARFs) with `arfgen` (version 1.98.3). The information of the photon-integration region is taken into account here.

Table 5.2 Observation log of U Gem-type and Z Cam-type dwarf novae with *XMM-Newton*

Object	Sequence#	Observation date [UT]	Observation length (ks)	Detector	Operating† mode	Exposure (ks)	Intensity‡ (count s^{-1})§
U Gem type							
EY Cyg	400670101	2007-04-23 12:43:52	45.36	MOS1	Full	41.90	0.092 ± 0.002
				MOS2	Full	41.47	0.091 ± 0.002
				pn	Full	27.34	0.291 ± 0.004
RU Peg	551920101	2008-06-09 07:16:50	53.07	MOS1	Small	18.78	2.792 ± 0.013
				MOS2	Small	16.75	2.887 ± 0.014
				pn	Full	5.24	9.807 ± 0.044
SS Cyg	111310201	2001-06-05 07:38:23	14.21	MOS1	Timing	9.06	9.919 ± 0.033
				MOS2	Timing	9.60	10.37 ± 0.033
				pn	Timing	10.12	24.86 ± 0.050
	791000201	2016-05-16 07:18:26	30.00	MOS1	Small	27.78	2.513 ± 0.010
				MOS2	Small	27.74	2.497 ± 0.010
				pn	Small	19.91	8.859 ± 0.021
	820230101	2018-11-24 07:23:42	59.30	MOS2	Timing	47.81	11.07 ± 0.015
SS Aur	502640201	2008-04-07 08:17:45	50.87	MOS1	Small	36.93	0.182 ± 0.002
				MOS2	Small	37.01	0.193 ± 0.002
				pn	Full	30.64	0.610 ± 0.005
U Gem	110070401	2002-04-13 05:13:28	23.00	MOS1	Large	22.18	0.871 ± 0.006
				MOS2	Small	21.76	0.830 ± 0.006
				pn	Small	15.14	2.628 ± 0.013
AB Dra	111971401	2002-06-02 20:48:32	10.91	pn	Full	6.93	0.685 ± 0.010
	111971601	2002-10-06 05:55:40	11.92	MOS1	Full	9.36	0.613 ± 0.008
				MOS2	Small	8.89	0.624 ± 0.009
				pn	Full	6.61	2.127 ± 0.019
Z Cam type							
WW Cet	111970901	2001-12-06 17:28:25	12.71	MOS1	Large	11.99	1.302 ± 0.011
				MOS2	Small	11.76	1.134 ± 0.010
				pn	Full	8.56	3.872 ± 0.021

† Full = Full Frame, Large = Large Window, Small = Small Window, Timing = Timing.
‡ In the band 0.5-10.0 keV for operating mode with Full, Large and Small and 0.8-10.0 keV for operating mode with Timing.
§ After background subtraction.

Table 5.3 Observation log of SU UMa-type dwarf novae with *XMM-Newton*

Object	Sequence#	Observation date [UT]	Observation length (ks)	Detector	Operating[†] mode	Exposure (ks)	Intensity[‡] (count s^{-1})[§]
SU UMa type							
YZ Cnc	152530101	2002-10-05 07:02:40	36.91	MOS1	Full	13.08	0.840 ± 0.008
				MOS2	Small	12.25	0.846 ± 0.008
				pn	Full	9.00	2.835 ± 0.018
TY PsA	111970101	2001-11-28 19:05:24	13.21	MOS1	Full	12.49	0.373 ± 0.006
				MOS2	Full	13.44	0.348 ± 0.006
				pn	Full	8.96	1.120 ± 0.011
SU UMa	111970801	2002-05-05 17:18:34	14.50	MOS1	Small	7.67	1.767 ± 0.016
				MOS2	Small	7.18	1.915 ± 0.017
				pn	Full	5.41	5.987 ± 0.034
VW Hyi	111970301	2001-10-19 05:24:31	19.32	MOS1	Small	18.17	0.532 ± 0.006
				MOS2	Small	18.17	0.566 ± 0.006
				pn	Full	14.45	1.923 ± 0.012
V1504 Cyg	801100101	2017-09-26 15:58:01	97.00	MOS1	Full	66.15	0.012 ± 0.000
				MOS2	Full	66.92	0.012 ± 0.000
				pn	Full	53.59	0.036 ± 0.001
QZ Vir	801100101	2002-06-01 11:06:11	12.87	MOS1	Large	12.15	1.010 ± 0.009
				MOS2	Small	11.91	0.983 ± 0.009
				pn	Full	8.99	3.716 ± 0.019
WZ Sge	150100101	2003-05-16 14:52:07	9.92	MOS1	Large	4.72	0.871 ± 0.014
				MOS2	Large	4.82	0.898 ± 0.014
				pn	Full	2.52	2.661 ± 0.033
GW Lib	303180101	2005-08-25 21:46:30	21.85	MOS1	Full	21.33	0.007 ± 0.001
				MOS2	Full	21.35	0.006 ± 0.001
				pn	Full	17.40	0.026 ± 0.002
	801800201	2018-02-17 05:46:41	57.00	MOS1	Full	30.09	0.056 ± 0.001
				MOS2	Full	31.54	0.058 ± 0.001
				pn	Full	18.20	0.190 ± 0.003
V893 Sco	553720101	2009-02-05 21:41:31	54.92	MOS1	Large	53.94	0.840 ± 0.004
				MOS2	Large	53.95	0.857 ± 0.004
				pn	Full	19.25	2.189 ± 0.011
Z Cha	205770101	2003-12-19 20:45:52	101.42	MOS1	Large	93.68	0.330 ± 0.002
				MOS2	Large	95.17	0.328 ± 0.002
				pn	Full	74.74	1.027 ± 0.004
HT Cas	111310101	2002-08-20 09:23:50	49.85	MOS1	Large	25.44	0.302 ± 0.003
				MOS2	Large	27.42	0.307 ± 0.003
				pn	Full	20.32	0.877 ± 0.007
	152490201	2003-07-12 05:52:42	55.54	MOS1	Large	3.32	0.390 ± 0.011
				MOS2	Large	3.26	0.391 ± 0.011
				pn	Full	1.78	0.943 ± 0.023
OY Car	099020301	2000-06-29 22:37:25	61.43	MOS1	Full	43.69	0.381 ± 0.003
				MOS2	Full	42.74	0.378 ± 0.003
				pn	Full	29.35	1.103 ± 0.006
	128320301	2000-08-07 07:56:02	23.53	MOS1	Full	12.02	0.158 ± 0.004
				MOS2	Full	12.74	0.178 ± 0.004
				pn	Full	5.48	0.527 ± 0.010

[†] Full = Full Frame, Large = Large Window, Small = Small Window, Timing = Timing.
[‡] In the band 0.5-10.0 keV.
[§] After background subtraction.

5.2 *Suzaku* observations of VW Hyi and SS Cyg

To elucidate time variation of boundary layer behaviour in the optically-quiescent state, we have utilized series of VW Hyi data and SS Cyg taken with *Suzaku*. We have screened the data with `xselect` version 2.4e, which is included in the HEASOFT package provided by NASA's Goddard Space Flight Center (GSFC)[4]. We have mostly followed the standard data selection criteria. We have only used data while the telemetry rate is either high or medium.

For the XIS, we have removed bad pixels and flickering pixels, and have selected events of grade 0, 2, 3, 4 and 6. We have discarded data taken during spacecraft passages through the South Atlantic Anomaly (SAA) and when the pointing accuracy is low. Also discarded are data taken while the elevation of objects from the night earth limb is less than 5 deg. On the other hand, the standard data screening criteria recommend not to use the data when the object is within 20 deg from the bright earth limb. The number, however, depends upon attitude and orbit condition at the time of the observation. In addition to this, VW Hyi lies close to the south ecliptic pole, and hence the XIS field of view tends to be close to the earth limb. These facts suggest that significant amounts of data would be discarded with the standard day-earth elevation angle. Accordingly, we have drawn spectra with various trial day- earth elevation angles and, by closely inspecting the spectra in the band 0.3-0.7 keV, where the atmospheric Nitrogen and Oxygen lines appear, we have found that the cutoff day-earth elevation angle can be set as small as 7 deg. This process was also applied to the XIS data of SS Cyg. An observation image of XIS is shown in Fig. 5.4. In extracting spectra, we have collected X-ray photons arriving in a circular aperture with a radius of 3.'5 centered on the source. The background photons have been integrated over an annular region with inner and outer radii of 4' and 6.'5, respectively. For spectral analysis, we have made the RMFs of XIS with the software `xisrmfgen` (version 2012-04-21) and the ARFs with `xissimarfgen` (version 2010-11-05). The RMFs and the ARFs thus produced are merged with `marfrmf` (v3.2.6) for the XIS modules sepa rately, and the resultant response matrix files of the XIS0, XIS2 and XIS3 (FI CCDs) are coadded with `addrmf`.

For the HXD, on the other hand, we have screened the data with `aepipeline` (version 1.1.0). We did not use the HXD-GSO data because significant signals from objects were not detected. The background event used the "tuned" non-Xray background (NXB) event file published by the HXD team[5]. In addition to this, we considered the cosmic X-ray background (CXB). Following results based on HEAO–1 observation (Boldt 1987), we created the CXB spectrum from

$$f_{\mathrm{CXB}(E)} = 9.412 \times 10^{-3} \times \left(\frac{E}{1\ \mathrm{keV}}\right)^{-1.29} \times \exp\left(-\frac{E}{40\ \mathrm{keV}}\right) \quad [\mathrm{photons\ /\ cm^2\ /\ s\ /\ FOV\ /\ keV}] \tag{5.1}$$

[4] `https://heasarc.gsfc.nasa.gov/docs/software.html`
[5] `https://heasarc.gsfc.nasa.gov/docs/suzaku/analysis/pinbgd.html`

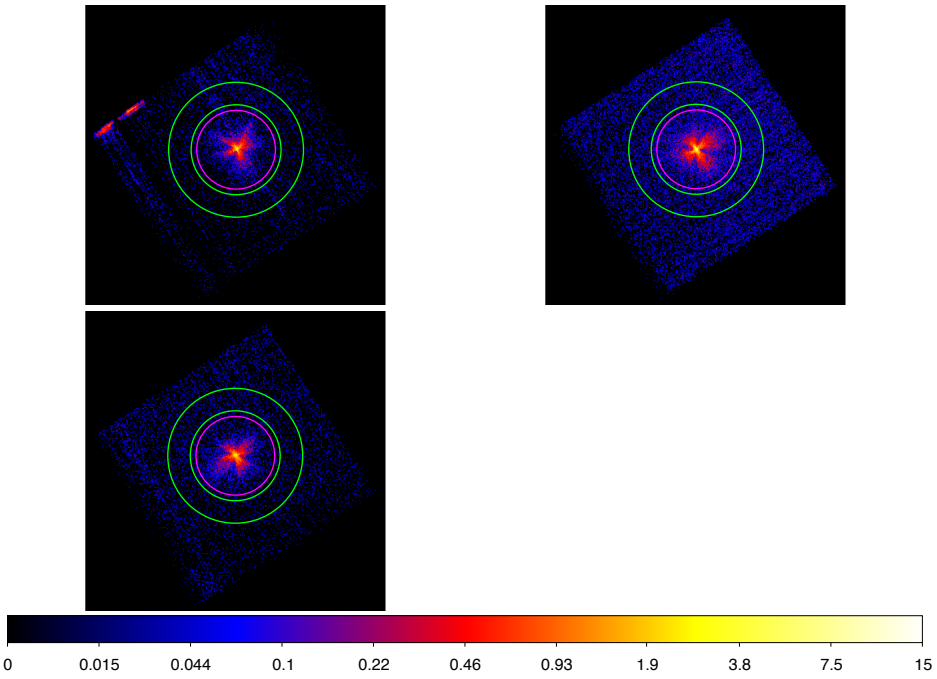

Fig. 5.4 Image of VW Hyi in December 2011 obtained with XIS0 (upper left), XIS1 (upper right) and XIS3 (lower left). Magenta circles show source area, and green annuli show background area.

by the `fakeit` command in the spectral fit software XSPEC with an exposure time of 10 Ms. In doing this, we adopted the PIN flat sky response that is provided by the HXD team according to the observation date. Details are listed in `https://heasarc.gsfc.nasa.gov/docs/suzaku/analysis/pinepochs.html`.

Table 5.4 summarizes the Suzaku observations of VW Hyi and SS Cyg in the quiescent state. Because VW Hyi was too faint for spectral analysis in the HXD band, and SS Cyg in 2014 was observed only in XIS, the HXD-PIN data were used only data of SS Cyg in 2005.

Table 5.4 Observation log of VW Hyi and SS Cyg with *Suzaku*.

Object	Sequence#	Observation date [UT]	Observation length (ks)	Detector	Mode	Exposure (ks)	Intensity[†] (count s^{-1})[§]
VW Hyi	406009020	2011-12-29 15:19:16	46.86	XIS-FI	Normal	18.35	1.08 ± 0.01
				XIS-BI	Normal	18.35	
	406009030	2012-02-29 13:39:04	58.87	XIS-FI	Normal	22.83	0.93 ± 0.01
				XIS-BI	Normal	22.83	
	406009040	2012-05-02 19:29:54	30.62	XIS-FI	Normal	18.08	0.99 ± 0.01
				XIS-BI	Normal	18.08	
SS Cyg	400006010	2005-11-02 01:12:32	80.81	XIS-FI	Normal	42.03	3.197 ± 0.005
				XIS-BI	Normal	42.24	4.319 ± 0.010
				HXD-PIN	Normal	30.02	0.098 ± 0.004
	109015010	2014-12-19 06:23:57	63.14	XIS-FI	Normal	48.91	1.422 ± 0.004
				XIS-BI	Normal	48.89	1.783 ± 0.006

[†] In the band 0.5–10.0 keV for the XIS and 15–40 keV for the HXD-PIN.
[§] After background subtraction.

5.3 *NICER* observations of SS Cyg

Suzaku and *XMM-Newton* have observed the dwarf nova during quiescence, but only once within the phase between one outburst and the next. To analyze in detail the temporal variation of the boundary layer, we used a series of *NICER* data taken observed 11 times within a single outburst phase of SS Cyg. Each observation data were screened with the filtering tool `nicerl2` (version 1.12) included in NICERDAS. The background events for each observation were estimated by `nibackgen3C50` (v6)[6]. RMFs and ARFs are given to all 52 FPM modules. We merged them together with `addrmf` and `addarf` included in the HEASOFT package. Note that the modules of DET_ID 14 and 34 were removed from the data reduction due to the high frequency of noise contamination. The observation log is summarized in Table 5.5.

Table 5.5 Observation log of SS Cyg with *NICER*.

Object	Sequence#	Observation date [UT]	Observation length (ks)	Exposure (ks)	Intensity[†] (count s^{-1})[§]
SS Cyg	3201600109	2020-05-21 11:03:02	45.22	2.52	217.50 ± 0.29
	3201600110	2020-05-22 10:16:06	17.53	2.56	280.50 ± 0.33
	3201600111	2020-05-23 11:02:45	17.62	2.45	238.20 ± 0.31
	3201600112	2020-05-24 11:49:24	17.43	2.15	204.40 ± 0.31
	3201600113	2020-05-25 03:19:04	73.15	1.38	113.20 ± 0.29
	3201600114	2020-05-26 04:33:00	0.11	0.11	109.20 ± 0.99
	3201600115	2020-05-27 04:52:09	28.09	1.38	132.60 ± 0.31
	3201600116	2020-05-28 02:33:08	34.15	2.94	143.50 ± 0.22
	3201600117	2020-05-29 06:26:29	6.35	1.55	195.90 ± 0.36
	3201600122	2020-06-09 23:35:06	0.92	0.79	130.70 ± 0.41
	3201600123	2020-06-12 01:10:20	1.30	1.29	95.44 ± 0.27

[†] In the band 0.5–10.0 keV.
[§] After background subtraction.

[6] `https://heasarc.gsfc.nasa.gov/docs/nicer/tools/nicer_bkg_est_tools.html`

CHAPTER 6

Spectral analysis

6.1 Evaluation of the DNe spectra observed by *XMM-Newton*

To evaluate the X-ray spectra of 19 dwarf novae in optical quiescence observed with *XMM-Newton*, we use the software XSPEC (Arnaud 1996) version 12.10.0 in the HEASOFT package provided by NASA's GSFC[1]. We have adopted the following two spectral models to represent the multi-temperature plasma emission from the boundary layer: the CEVMKL model and the VMCFLOW model. In CEVMKL, the differential emission measure (DEM) is represented with a power-law function of the temperature. In VMCFLOW, on the other hand, the temperature dependence of the DEM is subject to the temperature dependence of the volume emissivity of the plasma (so called "cooling function"; see § 3.7). VMCFLOW has been found to succeed in representing X-ray spectra of DNe in general (Pandel et al. 2005, Baskill et al. 2005, Wada et al. 2017).

Since the boundary layer plasma is formed in contact with the white dwarf surface, a significant fraction of its X-ray emission is intercepted by the white dwarf and a part of it is reflected off into space. The existence of such a reflected component is evidenced by an Fe Kα iron fluorescence line at 6.4 keV (George and Fabian 1991). To estimate the intensity of the reflected component by the white dwarf, we have added the xspec model REFLECT and the 6.4 keV Gaussian model. In addition, to account for the extinction by the interstellar medium (ISM), we adopted the photoelectric absorption (TBABS; Wilms et al. (2000)).

The spectral fitting was performed by restricting the energy range to 0.5–10 keV for most of the spectra. However, the spectrum of SS Cyg observed in 2001 in pn timing mode was limited to 0.8–10 keV because of a high background level at low energy. We tied model parameters between different instrumental spectra, except for the normalization of the multi-temperature model, and performed simultaneous fitting for each object. Note that the flux difference among the three XMM-Newton EPIC cameras is in general less than 10% (Tsujimoto et al. 2011). The solid angle $\Omega/2\pi$ of the reflector subtending over the boundary layer plasma is fixed at 1.5. This is based on the result of the spectral evaluation of SS Cyg in quiescence ($\Omega/2\pi$ = 1.7 ± 0.2; see Ishida et al. (2009)). If the boundary layer is small enough compared with the white dwarf ($R_{\rm BL} \ll 0.1 R_{\rm WD}$), the surface of the white dwarf is viewed from the plasma as

[1] http://heasarc.gsfc.nasa.gov

an infinite plane covering half of the sky ($\Omega/2\pi = 1$). The accretion disc is further thought to cover half of the remaining sky ($\Omega/2\pi = 0.5$). We have fixed the inclination of the reflector at the same value as the orbital inclination in table 5.1. Some of the objects (V893 Sco, Z Cha, HT Cas and OY Car) have low fluxes in the low energy band ($\sim$ 0.6–2.0 keV) and could not be fitted only by ISM absorption. V893 Sco was found to have a partial X-ray eclipse and high intrinsic absorption (Mukai et al. 2009). Other objects have a high orbital inclination angle, exceeding 80°, and hence, it is likely that some of the boundary layer emission is absorbed by the accretion disk. We therefore added a partial covering absorption model, PCFABS.

The best-fit continuum parameters with the CEVMKL and VMCFLOW models are summarized in table 6.1 and 6.2, respectively. The mass accretion rate ($\dot{M}$) determined by the VMCFLOW is derived from the EPIC-pn spectrum with the highest signal-to-noise ratio (S / N). $L_{\rm bol}$ is the bolometric luminosity of the source, which is evaluated, given the bolometric flux and the distance in table 5.1.

$$L_{\rm bol} = 4\pi D^2 f_{\rm bol} \tag{6.1}$$

From the χ^2 values, the CEVMKL model fits better to the observed spectra than the VMCFLOW model (Fig. 6.1). An $F-$test reveals, however, that the addition of the DEM slope parameter (α in eq.3.10) is significant at more than 99% confidence level. The advantage of the CEVMKL model over the VMCFLOW model is also suggested by Pandel et al. (2005). Figure 7.4 is the correlation diagram of the maximum temperature ($T_{\rm max}$) calculated from CEVMKL and VMCFLOW models. The $T_{\rm max}$ of the CEVMKL ranges from 5.74 keV in VW Hyi to 20.57 keV in 2001 SS Cyg, while that of the VMCFLOW covers a wide range from 3.58 keV in V1504 Cyg to 27.93 keV in RU Peg. From Fig. 7.4, the $T_{\rm max}$ tends to be larger in VMCFLOW than in CEVMKL. However, VMCFLOW temperatures of AB Dra in June 2002 and V1504 Cyg were calculated to be lower than CEVMKL. These two objects show a low $T_{\rm max}$ with the VMCFLOW model. At the same time, the α of CEVMKL is also low. These fact mean that the spectra of these two objects are softer than the others. The correlation of bolometric luminosity between CEVMKL and VMCFLOW is also shown in Fig 6.3. These were approximately consistent between the two models. Since the CEVMKL model provides better fit to the observed spectra in general, hereafter we basically adopt the physical parameters given by the CEVMKL model.

The result of the fit with the cevmkl model is shown in Fig. 6.4, 6.5, 6.6 and 6.7. Although some data have limited statistics, the spectra are characterized by helium-like and hydrogen-like Kα emission lines (here after referred to as Heα and Lyα, respectively) of Mg (1.34 keV and 1.47 keV), Si (1.86 keV and 2.01 keV), S (2.45 keV and 2.62 keV) and Fe (6.68 keV and 6.96 keV). This fact is the direct evidence that he X-ray emission from DN originates from a thermal plasma with multiple temperatures. The resultant elemental abundances with these models are listed in table 6.3 and 6.4. The equivalent widths of the 6.4 keV line for each object are summarized in table 6.5. The fluorescent iron emission lines at 6.4 keV are almost invisible in some spectra, such as SS Aur, SU UMa, GW Lib, and OY Car. Of them, $T_{\rm max}$ of GW Lib

and OY Car is less than 10 keV, which is not enough to generate X-rays that raise inner shell ionization of iron. SU UMa belongs to a group of having the smallest iron abundance (table 6.3 and 6.4).

Table 6.1 Best-fit continuum parameters with the CEVMKL model.

Object	$N_{\rm H}^{\dagger}$	CFrac†	$N_{\rm H}^{\rm ISM}$	$T_{\rm max}$	α	Flux§§		Luminosity§§	reduced χ^2
						0.2 - 12 keV	Bolometric$^{\|\|}$	Bolometric$^{\|\|}$	
	(10^{20} cm^{-2})		(10^{20} cm^{-2})	(keV)		(10^{-12} erg cm^{-2} s^{-1})		(10^{30} erg s^{-1})	(d.o.f.)
EY Cyg			$3.16^{+1.69}_{-1.57}$	$7.62^{+2.03}_{-1.55}$	$1.17^{+0.26}_{-0.29}$	1.02	1.10	55.42 ± 1.04	0.98 (207)
RU Peg			$4.83^{+0.59}_{-0.51}$	$16.64^{+1.59}_{-1.36}$	$1.15^{+0.07}_{-0.10}$	39.02	50.46	462.96 ± 8.06	1.06 (335)
SS Cyg_01			$2.36^{+0.52}_{-0.48}$	$20.57^{+1.14}_{-1.17}$	$0.73^{+0.04}_{-0.05}$	124.57	163.04	257.02 ± 2.04	1.51 (995)
SS Cyg_16			$2.63^{+0.48}_{-0.40}$	$19.98^{+1.37}_{-1.18}$	$0.69^{+0.02}_{-0.05}$	34.39	44.45	70.07 ± 0.56	
SS Cyg_18			$1.97^{+0.34}_{-0.42}$	$18.45^{+0.47}_{-1.24}$	$0.85^{+0.06}_{-0.04}$	154.65	199.07	313.82 ± 2.50	
SS Aur			$2.87^{+1.18}_{-1.21}$	$13.55^{+1.67}_{-1.65}$	$1.11^{+0.10}_{-0.10}$	2.50	3.01	24.39 ± 0.37	1.04 (298)
U Gem			$0.36^{+0.71}_{-0.36}$	$17.03^{+1.54}_{-1.58}$	$1.05^{+0.06}_{-0.07}$	11.03	14.07	14.72 ± 0.06	1.06 (374)
AB Dra_02/Jun			$4.92^{+4.54}_{-3.90}$	$9.90^{+4.54}_{-2.37}$	$0.41^{+0.22}_{-0.21}$	2.16	2.33	46.79 ± 0.72	1.07 (375)
AB Dra_02/Oct			$6.16^{+1.55}_{-1.58}$	$10.62^{+1.53}_{-1.33}$	$0.95^{+0.14}_{-0.13}$	7.19	8.17	164.45 ± 2.53	
WW Cet			$2.51^{+0.91}_{-0.81}$	$8.13^{+0.78}_{-0.70}$	$1.28^{+0.15}_{-0.15}$	12.84	14.03	79.97 ± 1.15	1.03 (369)
YZ Cnc			$0.33^{+0.98}_{-0.33}$	$10.44^{+0.80}_{-0.78}$	$1.28^{+0.07}_{-0.07}$	10.08	11.60	79.87 ± 1.26	1.06 (343)
TY PsA			$2.16^{+1.33}_{-1.22}$	$6.12^{+0.74}_{-0.72}$	$1.71^{+0.34}_{-0.24}$	3.66	3.87	15.72 ± 0.27	1.15 (269)
SU UMa			$1.65^{+0.87}_{-0.85}$	$9.53^{+1.02}_{-0.83}$	$1.15^{+0.13}_{-0.12}$	20.27	22.68	132.34 ± 1.18	1.10 (341)
VW Hyi			$0.00^{+0.28}_{-0.00}$	$5.74^{+0.17}_{-0.43}$	$1.32^{+0.10}_{-0.06}$	5.93	7.17	2.50 ± 0.00	1.11 (335)
V1504 Cyg			$13.45^{+5.62}_{-9.44}$	$9.27^{+14.10}_{-1.89}$	$0.21^{+0.35}_{-0.21}$	0.10	0.11	3.56 ± 0.13	1.19 (145)
QZ Vir			$0.00^{+0.37}_{-0.00}$	$6.21^{+0.30}_{-0.39}$	$1.67^{+0.12}_{-0.10}$	10.51	12.22	24.00 ± 0.26	1.14 (361)
WZ Sge			$5.71^{+2.17}_{-1.77}$	$10.08^{+1.91}_{-1.54}$	$1.35^{+0.31}_{-0.27}$	9.93	11.38	2.78 ± 0.01	0.95 (288)
GW Lib_05			$0.00^{+82.25}_{-0.0}$	$6.63^{+25.79}_{-3.68}$	$0.71^{+1.20}_{-0.55}$	0.08	0.11	0.17 ± 0.00	1.25 (262)
GW Lib_18			$6.02^{+6.73}_{-4.00}$	$7.08^{+2.23}_{-1.39}$	$0.66^{+0.34}_{-0.21}$	0.62	0.65	0.99 ± 0.01	
V893 Sco	$262.16^{+26.36}_{-25.32}$	$0.61^{+0.02}_{-0.02}$	$24.72^{+1.16}_{-1.16}$	$8.91^{+0.59}_{-0.61}$	$2.07^{+0.49}_{-0.30}$	12.91	15.59	28.81 ± 0.26	1.27 (399)
Z Cha	$321.01^{+82.10}_{-66.42}$	$0.30^{+0.04}_{-0.04}$	$12.25^{+0.73}_{-0.73}$	$6.58^{+0.37}_{-0.36}$	$2.03^{+0.19}_{-0.16}$	4.17	4.56	7.30 ± 0.15	1.07 (399)
HT Cas_02	$588.89^{+390.92}_{-242.68}$	$0.25^{+0.08}_{-0.08}$	$16.88^{+1.22}_{-1.38}$	$6.88^{+0.88}_{-0.67}$	$2.14^{+0.39}_{-0.28}$	3.93	4.36	10.45 ± 0.13	1.13 (593)
HT Cas_03	$294.46^{+914.78}_{-205.51}$	$0.27^{+0.22}_{-0.15}$	$34.87^{+8.23}_{-5.93}$	$10.64^{+7.32}_{-3.54}$	$1.51^{+4.40}_{-0.78}$	4.85	5.95	14.27 ± 0.18	
OY Car_00/Jun	$421.04^{+143.88}_{-99.80}$	$0.35^{+0.04}_{-0.04}$	$8.78^{+0.96}_{-0.93}$	$6.99^{+0.37}_{-0.37}$	$2.05^{+0.15}_{-0.14}$	4.98	5.51	5.45 ± 0.02	1.14 (479)
OY Car_00/Aug	$485.03^{+328.68}_{-168.83}$	$0.44^{+0.08}_{-0.08}$	$13.16^{+2.36}_{-2.21}$	$6.50^{+1.01}_{-0.85}$	$1.89^{+0.37}_{-0.29}$	2.53	2.78	2.75 ± 0.01	

NOTE: Errors of $N_{\rm H}$, CFrac, $N_{\rm H}^{\rm ISM}$, $T_{\rm max}$, α are single parameter 90% confidence level.
† Parameters of partial covering absorption model.
§§ The reflected component being excluded (Ω is set equal to zero after the fit converged).
|| Flux or luminosity in the band 0.04–100 keV.

Table 6.2 Best-fit continuum parameters with the VMCFLOW model.

Object	$N_{\rm H}^{\dagger}$	CFrac†	$N_{\rm H}^{\rm ISM}$	$T_{\rm max}$	$\dot{M}$	Flux§§		Luminosity§§	reduced χ^2
						0.2 - 12 keV	Bolometric$^{\|\|}$	Bolometric$^{\|\|}$	
	(10^{20} cm^{-2})		(10^{20} cm^{-2})	(keV)	($10^{-12} M_{\odot}$yr^{-1})	(10^{-12} erg cm^{-2} s^{-1})		(10^{30} erg s^{-1})	(d.o.f.)
EY Cyg			$4.02^{+0.84}_{-1.58}$	$9.97^{+2.81}_{-1.93}$	$27.82^{+4.78}_{-4.76}$	1.01	1.12	56.18 ± 1.05	0.98 (208)
RU Peg			$5.10^{+0.50}_{-0.24}$	$27.93^{+2.22}_{-2.43}$	$79.80^{+2.93}_{-3.89}$	39.48	55.60	510.08 ± 8.88	1.09 (336)
SS Cyg_01			$0.87^{+0.26}_{-0.26}$	$23.52^{+0.83}_{-0.84}$	$46.64^{+1.18}_{-1.10}$	125.70	166.36	262.25 ± 2.09	1.60 (998)
SS Cyg_16			$1.02^{+0.22}_{-0.23}$	$21.37^{+0.72}_{-0.69}$	$13.90^{+0.33}_{-0.33}$	34.57	44.60	70.30 ± 0.56	
SS Cyg_18			$1.47^{+0.21}_{-0.22}$	$23.83^{+0.92}_{-0.89}$	$57.72^{+1.51}_{-1.47}$	154.53	205.47	323.91 ± 2.58	
SS Aur			$1.88^{+0.93}_{-1.00}$	$17.58^{+2.35}_{-1.37}$	$6.20^{+0.40}_{-0.55}$	2.50	3.07	24.90 ± 0.38	1.06 (299)
U Gem			$0.00^{+0.29}_{-0.00}$	$21.64^{+1.45}_{-0.67}$	$2.81^{+0.09}_{-0.12}$	10.97	14.95	15.63 ± 0.06	1.10 (375)
AB Dra_02/Jun			$0.00^{+82.25}_{-0.00}$	$5.78^{+1.02}_{-0.40}$	$36.19^{+2.25}_{-4.47}$	2.16	2.58	51.95 ± 0.80	1.17 (377)
AB Dra_02/Oct			$5.27^{+0.88}_{-0.96}$	$12.07^{+1.13}_{-0.77}$	$65.11^{+4.09}_{-4.65}$	7.03	8.03	161.59 ± 2.48	
WW Cet			$3.89^{+0.66}_{-0.77}$	$11.81^{+1.13}_{-0.77}$	$33.74^{+1.89}_{-2.43}$	12.82	14.55	82.93 ± 1.19	1.08 (370)
YZ Cnc			$0.00^{+0.54}_{-0.00}$	$13.38^{+0.60}_{-0.48}$	$25.46^{+0.77}_{-0.77}$	9.67	11.02	75.89 ± 1.19	1.08 (344)
TY PsA			$5.12^{+0.99}_{-1.31}$	$9.54^{+0.93}_{-0.45}$	$8.56^{+0.67}_{-0.72}$	3.63	3.98	16.19 ± 0.28	1.23 (270)
SU UMa			$2.27^{+0.64}_{-0.80}$	$13.68^{+1.32}_{-1.07}$	$45.92^{+3.01}_{-3.23}$	20.29	23.63	137.88 ± 1.23	1.13 (342)
VW Hyi			$0.00^{+0.28}_{-0.00}$	$7.14^{+0.24}_{-0.26}$	$1.39^{+0.05}_{-0.04}$	5.93	7.06	2.47 ± 0.00	1.12 (336)
V1504 Cyg			$0.00^{+3.22}_{-0.00}$	$3.58^{+0.40}_{-0.91}$	$4.82^{+1.51}_{-1.01}$	0.10	0.13	4.22 ± 0.15	1.36 (146)
QZ Vir			$2.16^{+0.74}_{-0.81}$	$9.54^{+0.55}_{-0.23}$	$10.83^{+0.30}_{-0.55}$	10.18	11.11	21.82 ± 0.27	1.34 (362)
WZ Sge			$6.72^{+1.60}_{-1.58}$	$15.48^{+2.39}_{-1.79}$	$0.90^{+0.10}_{-0.10}$	9.98	12.08	2.95 ± 0.01	0.96 (289)
GW Lib_05			$0.00^{+82.25}_{-0.00}$	$5.65^{+2.73}_{-1.63}$	$0.10^{+0.03}_{-0.03}$	0.08	0.09	0.14 ± 0.00	1.26 (264)
GW Lib_18			$2.31^{+1.89}_{-2.16}$	$6.96^{+1.21}_{-1.05}$	$0.73^{+0.14}_{-0.12}$	0.63	0.66	1.01 ± 0.01	
V893 Sco	$154.68^{+10.49}_{-9.16}$	$0.74^{+0.02}_{-0.02}$	$18.69^{+1.55}_{-1.54}$	$15.44^{+0.97}_{-0.87}$	$12.18^{+0.81}_{-0.76}$	12.11	15.78	29.17 ± 0.27	1.44 (400)
Z Cha	$63.90^{+8.84}_{-8.33}$	$0.68^{+0.05}_{-0.05}$	$2.03^{+2.28}_{-2.03}$	$11.61^{+0.83}_{-0.69}$	$4.08^{+0.33}_{-0.44}$	4.33	5.05	8.08 ± 0.16	1.22 (400)
HT Cas_02	$109.01^{+0.0}_{-109.01}$	$0.00^{+0.00}_{-0.00}$	$21.45^{+1.42}_{-1.40}$	$20.45^{+1.80}_{-1.70}$	$3.27^{+0.26}_{-0.24}$	4.18	5.59	13.40 ± 0.17	1.27 (595)
HT Cas_03	$132.58^{+3922.18}_{-109.68}$	$0.24^{+0.40}_{-0.19}$	$36.66^{+7.31}_{-28.81}$	$23.17^{+10.95}_{-7.91}$	$4.04^{+2.26}_{-1.18}$	5.13	7.34	17.62 ± 0.22	
OY Car_00/Jun	$82.87^{+8.83}_{-11.89}$	$0.66^{+0.02}_{-0.02}$	$0.00^{+82.25}_{-0.00}$	$11.83^{+1.31}_{-0.77}$	$2.89^{+0.25}_{-0.34}$	5.20	6.35	6.28 ± 0.02	1.27 (481)
OY Car_00/Aug	$127.74^{+40.27}_{-40.58}$	$0.60^{+0.09}_{-0.12}$	$8.37^{+4.37}_{-5.19}$	$9.72^{+2.10}_{-1.45}$	$1.96^{+0.47}_{-0.43}$	2.56	2.91	2.88 ± 0.01	

NOTE: Errors of $N_{\rm H}$, CFrac, $N_{\rm H}^{\rm ISM}$, $T_{\rm max}$, $\dot{M}$ are single parameter 90% confidence level.
† Parameters of partial covering absorption model.
§§ The reflected component being excluded (Ω is set equal to zero after the fit converged).
|| Flux or luminosity in the band 0.04–100 keV.

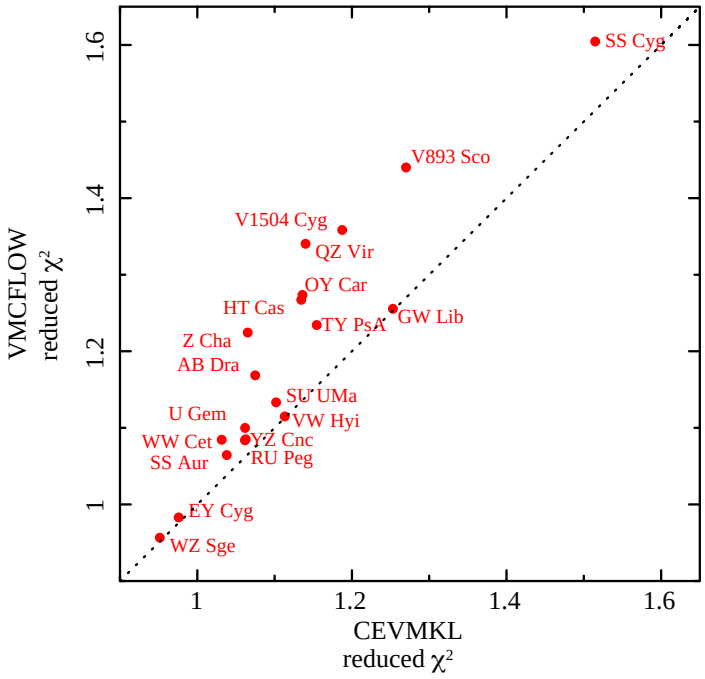

Fig. 6.1 Correlation diagram of reduced chi-squared (χ^2) obtained from CEVMKL and VMCFLOW models.

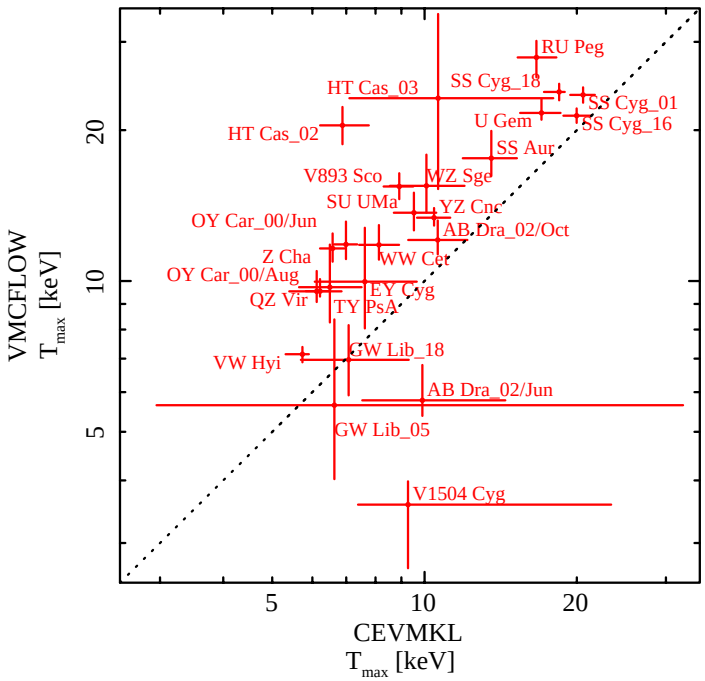

Fig. 6.2 Correlation diagram of maximum temperature ($T_{\rm max}$) calculated from CEVMKL and VMCFLOW models.

Table 6.3 Best-fit continuum parameters with the CEVMKL model.

Object	O	Ne	Mg	Si	S	Ar	Ca	Fe	Ni
EY Cyg	$0.15^{+0.20}_{-0.12}$	$0.34^{+0.51}_{-0.34}$	$0.47^{+0.54}_{-0.47}$	$0.69^{+0.38}_{-0.40}$	$0.83^{+0.63}_{-0.60}$	$1.27^{+1.86}_{-1.27}$	$2.99^{+2.60}_{-2.25}$	$0.33^{+0.11}_{-0.11}$	$1.51^{+1.67}_{-1.51}$
RU Peg	$0.34^{+0.10}_{-0.08}$	$0.29^{+0.27}_{-0.26}$	$0.57^{+0.30}_{-0.29}$	$0.90^{+0.23}_{-0.22}$	$1.30^{+0.34}_{-0.32}$	$2.81^{+0.98}_{-0.91}$	$0.60^{+1.11}_{-0.64}$	$0.52^{+0.06}_{-0.06}$	$2.33^{+0.82}_{-0.80}$
SS Cyg	$0.40^{+0.03}_{-0.04}$	$0.18^{+0.06}_{-0.06}$	$0.20^{+0.06}_{-0.06}$	$0.46^{+0.04}_{-0.04}$	$0.40^{+0.07}_{-0.07}$	$0.62^{+0.24}_{-0.24}$	$0.83^{+0.29}_{-0.28}$	$0.29^{+0.01}_{-0.02}$	$0.74^{+0.20}_{-0.19}$
SS Aur	$0.90^{+0.36}_{-0.30}$	$0.00^{+0.60}_{-0.00}$	$0.51^{+0.67}_{-0.51}$	$1.54^{+0.56}_{-0.49}$	$1.43^{+0.77}_{-0.71}$	$4.16^{+2.26}_{-2.11}$	$0.43^{+2.47}_{-0.43}$	$1.13^{+0.20}_{-0.17}$	$2.79^{+1.91}_{-1.77}$
U Gem	$0.47^{+0.17}_{-0.15}$	$0.06^{+0.40}_{-0.06}$	$1.13^{+0.49}_{-0.45}$	$1.44^{+0.36}_{-0.34}$	$1.11^{+0.49}_{-0.47}$	$1.00^{+1.38}_{-1.00}$	$2.17^{+1.70}_{-1.69}$	$1.05^{+0.12}_{-0.11}$	$4.41^{+1.30}_{-1.23}$
AB Dra	$0.23^{+0.19}_{-0.17}$	$0.03^{+0.39}_{-0.03}$	$0.53^{+0.47}_{-0.40}$	$0.79^{+0.37}_{-0.31}$	$1.32^{+0.58}_{-0.50}$	$1.64^{+1.56}_{-1.51}$	$3.22^{+2.01}_{-1.98}$	$0.59^{+0.12}_{-0.09}$	$1.95^{+0.64}_{-1.23}$
WW Cet	$0.29^{+0.13}_{-0.10}$	$0.34^{+0.28}_{-0.26}$	$0.39^{+0.29}_{-0.28}$	$0.55^{+0.21}_{-0.19}$	$0.44^{+0.28}_{-0.27}$	$0.85^{+0.83}_{-0.81}$	$0.86^{+0.99}_{-0.86}$	$0.31^{+0.05}_{-0.05}$	$0.71^{+0.74}_{-0.71}$
YZ Cnc	$1.22^{+0.31}_{-0.27}$	$0.15^{+0.58}_{-0.15}$	$1.57^{+0.65}_{-0.60}$	$2.88^{+0.54}_{-0.49}$	$2.43^{+0.66}_{-0.61}$	$3.69^{+1.72}_{-1.65}$	$1.36^{+1.90}_{-1.36}$	$1.61^{+0.18}_{-0.17}$	$5.99^{+1.70}_{-1.60}$
TY PsA	$0.34^{+0.27}_{-0.20}$	$0.74^{+0.63}_{-0.55}$	$0.59^{+0.56}_{-0.53}$	$0.40^{+0.35}_{-0.32}$	$0.81^{+0.52}_{-0.48}$	$1.59^{+1.48}_{-1.40}$	$0.55^{+1.62}_{-0.55}$	$0.47^{+0.10}_{-0.09}$	$0.09^{+1.30}_{-0.09}$
SU UMa	$0.34^{+0.13}_{-0.11}$	$0.38^{+0.30}_{-0.28}$	$0.52^{+0.34}_{-0.32}$	$0.44^{+0.23}_{-0.21}$	$0.72^{+0.34}_{-0.32}$	$1.05^{+0.99}_{-0.96}$	$0.85^{+1.21}_{-0.85}$	$0.38^{+0.06}_{-0.06}$	$0.01^{+0.81}_{-0.01}$
VW Hyi	$0.80^{+0.14}_{-0.18}$	$0.29^{+0.36}_{-0.29}$	$0.87^{+0.33}_{-0.34}$	$1.23^{+0.23}_{-0.23}$	$1.12^{+0.34}_{-0.31}$	$0.58^{+0.87}_{-0.58}$	$1.64^{+1.14}_{-0.58}$	$0.95^{+0.07}_{-0.12}$	$2.02^{+0.48}_{-0.93}$
V1504 Cyg	$1.24^{+1.49}_{-0.85}$	$0.00^{+1.13}_{-0.00}$	$1.87^{+2.33}_{-1.22}$	$2.04^{+2.14}_{-1.19}$	$2.10^{+2.66}_{-1.58}$	$6.60^{+5.48}_{-6.61}$	$0.04^{+7.96}_{-0.04}$	$1.16^{+0.83}_{-0.51}$	$3.99^{+5.70}_{-3.96}$
QZ Vir	$0.62^{+0.17}_{-0.14}$	$0.42^{+0.33}_{-0.29}$	$0.59^{+0.29}_{-0.30}$	$0.63^{+0.19}_{-0.19}$	$0.31^{+0.27}_{-0.27}$	$1.21^{+0.81}_{-0.82}$	$1.07^{+1.00}_{-0.97}$	$0.58^{+0.06}_{-0.06}$	$1.52^{+0.78}_{-0.77}$
WZ Sge	$0.88^{+0.52}_{-0.44}$	$2.65^{+1.20}_{-0.98}$	$0.54^{+0.84}_{-0.54}$	$1.79^{+0.71}_{-0.62}$	$2.18^{+0.99}_{-0.88}$	$1.95^{+2.42}_{-1.95}$	$1.05^{+2.70}_{-1.05}$	$0.47^{+0.14}_{-0.13}$	$1.84^{+2.28}_{-1.84}$
GW Lib	$0.65^{+0.43}_{-0.30}$	$0.35^{+0.60}_{-0.35}$	$0.20^{+0.61}_{-0.20}$	$0.57^{+0.53}_{-0.40}$	$0.17^{+0.66}_{-0.17}$	$2.70^{+2.45}_{-2.12}$	$0.80^{+2.75}_{-0.80}$	$0.30^{+0.15}_{-0.11}$	$1.29^{+2.09}_{-1.29}$
V893 Sco	$0.30^{+0.21}_{-0.14}$	$0.20^{+0.51}_{-0.20}$	$1.33^{+0.37}_{-0.36}$	$1.07^{+0.21}_{-0.20}$	$0.86^{+0.24}_{-0.22}$	$1.32^{+0.60}_{-0.58}$	$1.42^{+0.65}_{-0.62}$	$0.62^{+0.04}_{-0.04}$	$1.68^{+0.65}_{-0.64}$
Z Cha	$0.31^{+0.14}_{-0.13}$	$0.33^{+0.27}_{-0.25}$	$0.55^{+0.23}_{-0.23}$	$0.91^{+0.15}_{-0.15}$	$0.85^{+0.21}_{-0.19}$	$0.16^{+0.48}_{-0.16}$	$0.96^{+0.58}_{-0.56}$	$0.48^{+0.04}_{-0.04}$	$1.05^{+0.57}_{-0.57}$
HT Cas	$0.55^{+0.38}_{-0.32}$	$0.02^{+0.59}_{-0.02}$	$0.41^{+0.51}_{-0.41}$	$1.18^{+0.31}_{-0.29}$	$0.67^{+0.41}_{-0.39}$	$2.21^{+1.20}_{-1.08}$	$0.89^{+1.21}_{-0.89}$	$0.60^{+0.09}_{-0.08}$	$0.60^{+1.13}_{-0.60}$
OY Car	$0.41^{+0.22}_{-0.19}$	$0.73^{+0.45}_{-0.41}$	$1.07^{+0.39}_{-0.40}$	$1.79^{+0.27}_{-0.25}$	$1.82^{+0.39}_{-0.34}$	$0.99^{+0.80}_{-0.75}$	$1.02^{+0.93}_{-0.89}$	$1.12^{+0.09}_{-0.08}$	$1.48^{+1.01}_{-1.08}$

NOTE — Elemental abundances relative to those of the sun (Anders and Grevesse 1989) are tabulated. Abundances of He, C, N, Na and Al are fixed to unity.

Table 6.4 Best-fit continuum parameters with the VMCFLOW model.

Object	O	Ne	Mg	Si	S	Ar	Ca	Fe	Ni
EY Cyg	$0.15^{+0.21}_{-0.11}$	$0.15^{+0.47}_{-0.15}$	$0.48^{+0.50}_{-0.44}$	$0.64^{+0.45}_{-0.35}$	$0.81^{+0.66}_{-0.53}$	$1.38^{+1.84}_{-1.38}$	$3.28^{+2.49}_{-2.26}$	$0.29^{+0.08}_{-0.10}$	$1.07^{+1.69}_{-1.07}$
RU Peg	$0.36^{+0.09}_{-0.08}$	$0.00^{+0.15}_{-0.00}$	$0.70^{+0.14}_{-0.23}$	$0.99^{+0.19}_{-0.19}$	$1.46^{+0.31}_{-0.30}$	$3.32^{+0.94}_{-0.90}$	$1.06^{+1.04}_{-1.06}$	$0.52^{+0.04}_{-0.06}$	$2.19^{+0.74}_{-0.70}$
SS Cyg	$0.35^{+0.03}_{-0.03}$	$0.16^{+0.06}_{-0.05}$	$0.13^{+0.07}_{-0.06}$	$0.45^{+0.05}_{-0.05}$	$0.39^{+0.07}_{-0.07}$	$0.61^{+0.23}_{-0.23}$	$0.81^{+0.30}_{-0.30}$	$0.29^{+0.01}_{-0.01}$	$0.57^{+0.20}_{-0.19}$
SS Aur	$0.69^{+0.28}_{-0.22}$	$0.00^{+0.32}_{-0.00}$	$0.31^{+0.57}_{-0.31}$	$1.42^{+0.46}_{-0.41}$	$1.30^{+0.67}_{-0.61}$	$3.77^{+2.03}_{-1.92}$	$0.47^{+2.28}_{-0.46}$	$1.04^{+0.20}_{-0.15}$	$2.18^{+1.65}_{-1.62}$
U Gem	$0.35^{+0.08}_{-0.07}$	$0.00^{+0.29}_{-0.00}$	$0.71^{+0.36}_{-0.35}$	$1.20^{+0.25}_{-0.26}$	$0.86^{+0.38}_{-0.39}$	$0.75^{+1.15}_{-0.74}$	$1.82^{+1.46}_{-1.50}$	$0.97^{+0.09}_{-0.09}$	$3.51^{+1.00}_{-1.06}$
AB Dra	$0.07^{+0.12}_{-0.07}$	$0.00^{+0.24}_{-0.00}$	$0.27^{+0.36}_{-0.27}$	$0.59^{+0.26}_{-0.23}$	$0.99^{+0.43}_{-0.39}$	$1.15^{+1.20}_{-1.15}$	$2.33^{+1.61}_{-1.57}$	$0.56^{+0.08}_{-0.07}$	$0.76^{+0.96}_{-0.76}$
WW Cet	$0.32^{+0.13}_{-0.10}$	$0.11^{+0.20}_{-0.11}$	$0.49^{+0.27}_{-0.22}$	$0.57^{+0.21}_{-0.16}$	$0.56^{+0.26}_{-0.24}$	$1.20^{+0.76}_{-0.75}$	$1.38^{+0.92}_{-0.91}$	$0.27^{+0.06}_{-0.04}$	$0.53^{+0.64}_{-0.53}$
YZ Cnc	$1.05^{+0.23}_{-0.20}$	$0.00^{+0.42}_{-0.00}$	$1.22^{+0.49}_{-0.48}$	$2.64^{+0.19}_{-0.39}$	$2.25^{+0.55}_{-0.52}$	$3.55^{+1.50}_{-1.52}$	$1.67^{+1.71}_{-1.67}$	$1.52^{+0.14}_{-0.14}$	$5.46^{+1.40}_{-1.39}$
TY PsA	$0.46^{+0.26}_{-0.18}$	$0.09^{+0.41}_{-0.09}$	$0.72^{+0.48}_{-0.43}$	$0.48^{+0.32}_{-0.29}$	$0.92^{+0.50}_{-0.46}$	$2.02^{+1.51}_{-1.43}$	$1.20^{+1.78}_{-1.20}$	$0.42^{+0.10}_{-0.08}$	$0.12^{+1.17}_{-0.12}$
SU UMa	$0.35^{+0.11}_{-0.10}$	$0.22^{+0.21}_{-0.22}$	$0.60^{+0.31}_{-0.26}$	$0.50^{+0.22}_{-0.18}$	$0.83^{+0.31}_{-0.29}$	$1.46^{+0.90}_{-0.94}$	$1.28^{+1.11}_{-1.11}$	$0.36^{+0.07}_{-0.05}$	$0.00^{+0.69}_{-0.00}$
VW Hyi	$0.78^{+0.15}_{-0.14}$	$0.17^{+0.31}_{-0.17}$	$0.93^{+0.29}_{-0.29}$	$1.27^{+0.21}_{-0.21}$	$1.18^{+0.30}_{-0.30}$	$0.72^{+0.83}_{-0.72}$	$1.92^{+1.13}_{-1.11}$	$0.94^{+0.09}_{-0.08}$	$2.16^{+0.77}_{-0.81}$
V1504 Cyg	$0.12^{+0.35}_{-0.12}$	$0.00^{+0.40}_{-0.00}$	$0.63^{+0.73}_{-0.63}$	$0.93^{+0.61}_{-0.50}$	$0.77^{+0.90}_{-0.39}$	$2.46^{+2.95}_{-2.44}$	$1.46^{+3.74}_{-1.46}$	$0.59^{+0.17}_{-0.23}$	$0.38^{+1.70}_{-0.38}$
QZ Vir	$0.74^{+0.21}_{-0.17}$	$0.00^{+0.14}_{-0.00}$	$0.89^{+0.32}_{-0.31}$	$0.77^{+0.21}_{-0.21}$	$0.57^{+0.29}_{-0.29}$	$1.89^{+0.91}_{-0.90}$	$1.88^{+1.13}_{-0.57}$	$0.53^{+0.07}_{-0.07}$	$1.67^{+0.80}_{-0.82}$
WZ Sge	$0.94^{+0.50}_{-0.41}$	$1.96^{+0.87}_{-0.73}$	$0.65^{+0.77}_{-0.65}$	$1.75^{+0.71}_{-0.60}$	$2.25^{+0.98}_{-0.86}$	$2.37^{+2.44}_{-2.35}$	$1.74^{+2.86}_{-1.74}$	$0.46^{+0.16}_{-0.14}$	$1.72^{+2.25}_{-1.72}$
GW Lib	$0.60^{+0.42}_{-0.28}$	$0.49^{+0.60}_{-0.49}$	$0.00^{+0.56}_{-0.00}$	$0.44^{+0.47}_{-0.35}$	$0.10^{+0.62}_{-0.10}$	$2.29^{+2.24}_{-1.92}$	$0.88^{+2.57}_{-0.88}$	$0.29^{+0.14}_{-0.10}$	$0.95^{+2.09}_{-0.96}$
V893 Sco	$0.00^{+0.05}_{-0.00}$	$0.00^{0.82}_{-0.00}$	$1.02^{+0.29}_{-0.28}$	$0.68^{+0.15}_{-0.14}$	$0.77^{+0.19}_{-0.19}$	$1.52^{+0.54}_{-0.52}$	$1.91^{+0.64}_{-0.63}$	$0.72^{+0.04}_{-0.06}$	$3.68^{+0.67}_{-0.66}$
Z Cha	$0.38^{+0.13}_{-0.12}$	$0.00^{0.82}_{-0.00}$	$0.29^{+0.19}_{-0.18}$	$0.61^{+0.13}_{-0.12}$	$0.79^{+0.19}_{-0.18}$	$0.71^{+0.51}_{-0.50}$	$2.08^{+0.66}_{-0.64}$	$0.62^{+0.04}_{-0.04}$	$1.44^{+0.60}_{-0.59}$
HT Cas	$1.85^{+0.66}_{-0.57}$	$0.00^{0.82}_{-0.00}$	$0.75^{+0.58}_{-0.55}$	$1.46^{+0.44}_{-0.41}$	$1.28^{+0.57}_{-0.54}$	$5.03^{+1.86}_{-1.77}$	$3.67^{+2.10}_{-1.03}$	$0.90^{+0.13}_{-0.13}$	$0.00^{+1.38}_{-0.00}$
OY Car	$0.64^{+0.24}_{-0.21}$	$0.08^{+0.49}_{-0.08}$	$0.73^{+0.39}_{-0.38}$	$1.21^{+0.29}_{-0.23}$	$1.56^{+0.43}_{-0.33}$	$1.55^{+1.03}_{-0.85}$	$2.88^{+1.22}_{-1.11}$	$1.52^{+0.12}_{-0.10}$	$3.35^{+1.11}_{-1.26}$

NOTE — Elemental abundances relative to those of the sun (Anders and Grevesse 1989) are tabulated. Abundances of He, C, N, Na and Al are fixed to unity.

Table 6.5 Equivalent widths of Fe 6.4 keV line

Object	EW (CEVMKL) (eV)	EW (VMCFLOW) (eV)
EY Cyg	30^{+6}_{-4}	34^{+9}_{-2}
RU Peg	28^{+1}_{-1}	26^{+1}_{-1}
SS Cyg_01	41^{+1}_{-0}	40^{+1}_{-1}
SS Cyg_16	54^{+1}_{-0}	55^{+1}_{-1}
SS Cyg_18	24^{+1}_{-1}	20^{+1}_{-1}
SS Aur	2^{+2}_{-2}	2^{+2}_{-2}
U Gem	49^{+2}_{-1}	48^{+14}_{-11}
AB Dra_02/Jun	$175.02^{+19.16}_{-5.56}$	$202.46^{+2.76}_{-12.50}$
AB Dra_02/Oct	$76.47^{+6.67}_{-3.16}$	$60.67^{+6.51}_{-0.56}$
WW Cet	21^{+5}_{-1}	30^{+5}_{-1}
YZ Cnc	15^{+1}_{-2}	22^{+1}_{-1}
TY PsA	53^{+3}_{-4}	17^{+1}_{-2}
SU UMa	4^{+3}_{-2}	8^{+5}_{-1}
VW Hyi	17^{+2}_{-2}	16^{+17}_{-16}
V1504 Cyg	227^{+41}_{-10}	511^{+65}_{-20}
QZ Vir	13^{+1}_{-2}	19^{+4}_{-2}
WZ Sge	34^{+5}_{-6}	36^{+35}_{-22}
GW Lib_05	0^{+39}_{-0}	0^{+0}_{-0}
GW Lib_18	0^{+11}_{-0}	0^{+10}_{-0}
V893 Sco	29^{+1}_{-1}	30^{+1}_{-1}
Z Cha	24^{+1}_{-2}	32^{+2}_{-3}
HT Cas_02	20^{+1}_{-3}	35^{+3}_{-2}
HT Cas_03	89^{+6}_{-19}	97^{+4}_{-14}
OY Car_00/Jun	13^{+2}_{-2}	27^{+1}_{-2}
OY Car_00/Aug	0^{+5}_{-0}	9^{+5}_{-2}

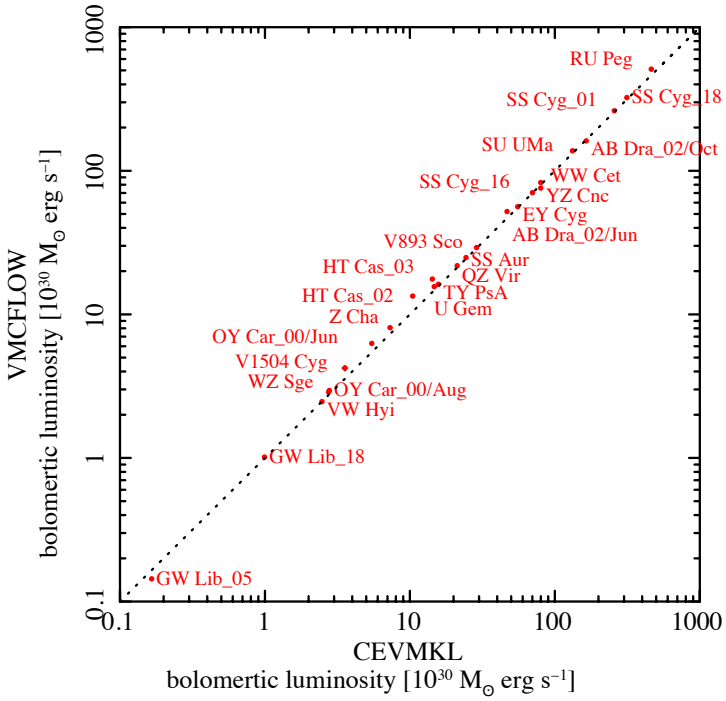

Fig. 6.3 Correlation diagram of bolometric luminosity ($L_{\rm bol}$) calculated from CEVMKL and VMCFLOW models.

6.2 Evaluation of a series of VW Hyi data

To observe the variation of the boundary layer, we have analysed one dataset of *XMM-Newton* and a series of *Suzaku* data of the SU UMa type dwarf nova VW Hyi in optical quiescence. This section is based on the result in Nakaniwa et al. (2019).

The spectra obtained by *Suzaku* are shown in Fig. 6.8. The insets are blow-ups of the iron Kα emission line energy band. As recognized from the insets, the iron Kα emission is dominated by the Heα component, whereas Lyα is detected only marginally. This implies that the maximum temperature of the plasma is lower than $\sim$10 keV as observed by *XMM-Newton*. It is also remarkable from the insets that the neutral iron Kα line (6.40 keV) seems absent. In evaluating the spectra, we adopt $N_{\rm H} = 6 \times 10^{17}$ cm^{-2} (Polidan et al. 1990) as the interstellar absorption hydrogen column density to VW Hyi. To make abundances of the major metals as model parameters common among all the spectra, we have tried to fit the four sets of data (three from Suzaku and one from XMM-Newton) simultaneously with the metal abundances being set free to vary but constrained to have common values.

The best-fit continuum parameters with the CEVMKL and VMCFLOW models are summarized in table 6.6 and 6.7, respectively. The resultant elemental abundances with these models are listed in table 6.8. The result of the fit with the VMCFLOW model is shown in Fig. 6.9. In the case of using the CEVMKL model, the maximum temperature of the plasma is nearly

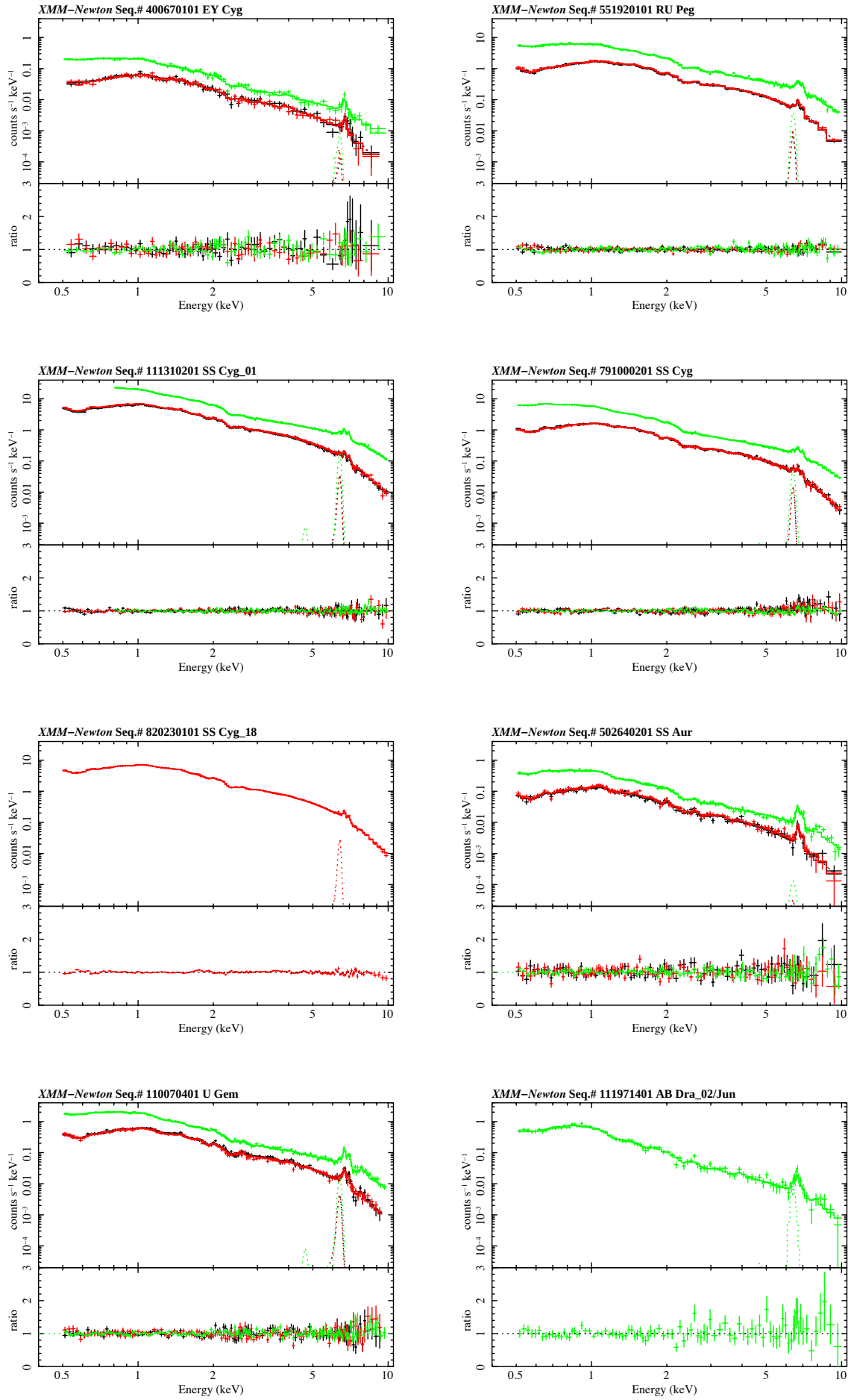

Fig. 6.4 Simultaneous fit of CEVMKL model to *XMM-Newton* spectra of MOS1 (black), MOS2 (red) and pn (green).

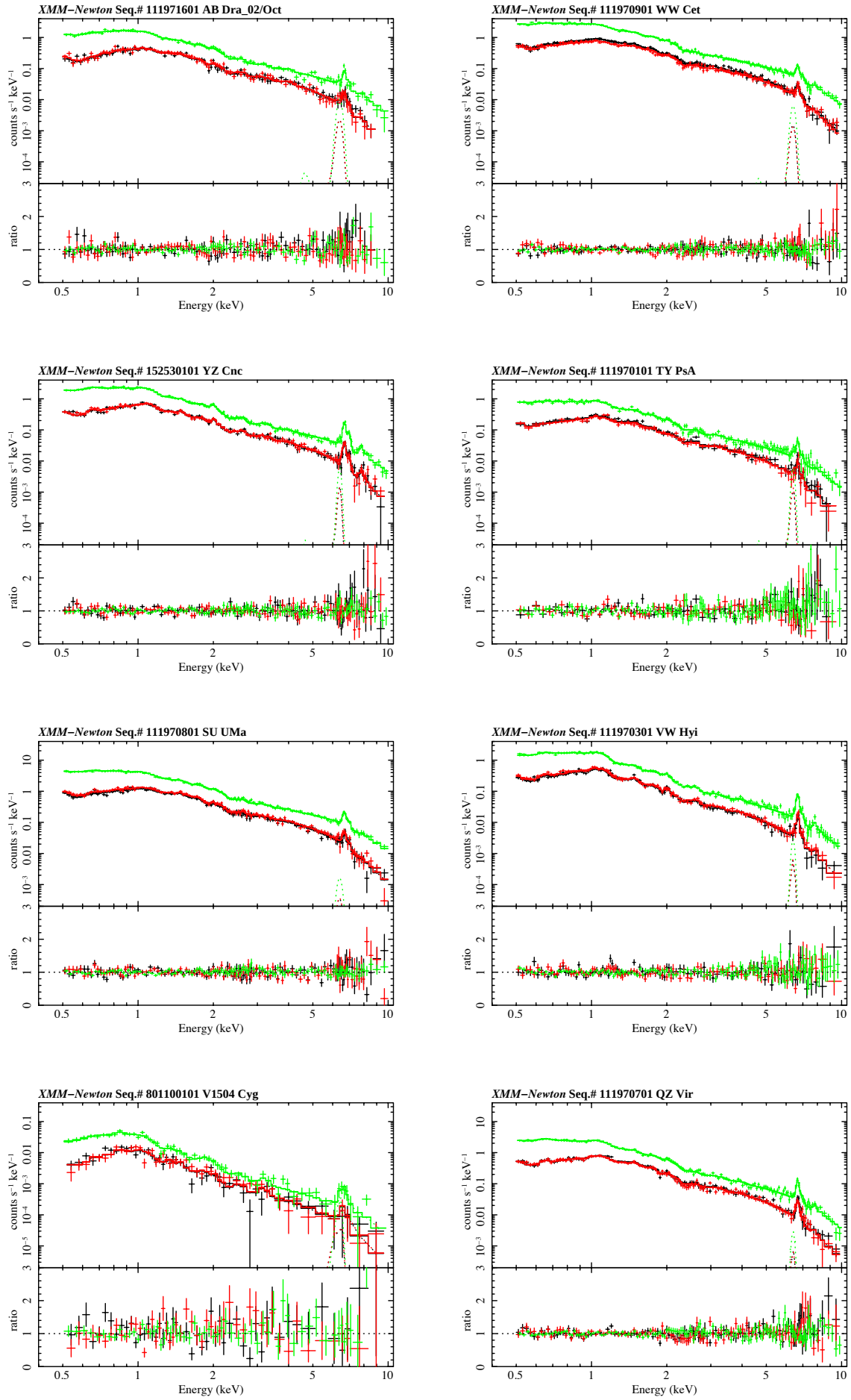

Fig. 6.5 Simultaneous fit of CEVMKL model to *XMM-Newton* spectra of MOS1 (black), MOS2 (red) and pn (green).

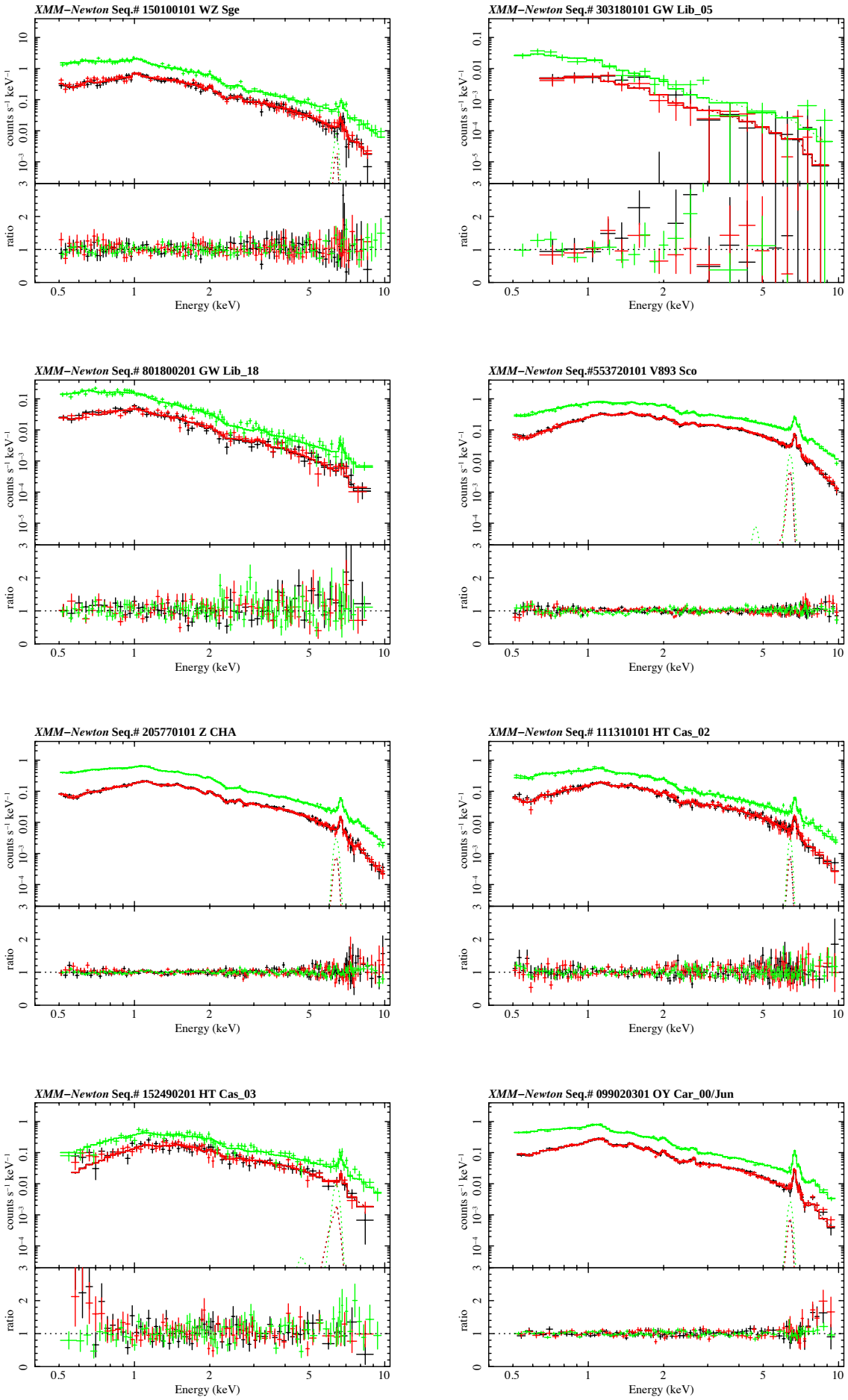

Fig. 6.6 Simultaneous fit of CEVMKL model to *XMM-Newton* spectra of MOS1 (black), MOS2 (red) and pn (green).

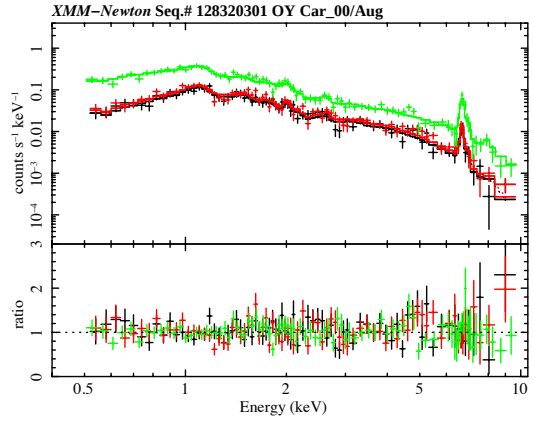

Fig. 6.7 Simultaneous fit of CEVMKL model to *XMM-Newton* spectra of MOS1 (black), MOS2 (red) and pn (green).

constant, being confined in the narrow range 5–6 keV (table 6.6). The DEM slope α of the first Suzaku observation (seq. #40609020) is, on the other hand, slightly larger than the other three observations. This means that the spectrum of the first *Suzaku* observation is slightly harder than the others. Based on the similarity of $T_{\rm max}$ and α, the spectral shapes of the other three observations resemble one another, although the flux of the *XMM-Newton* observation (seq. #0111970301) is roughly half of the second and third *Suzaku* observations (seq. #406009030 and #406009040). Note that the flux difference between the *Suzaku* and *XMM-Newton* detectors is in general less than 10% (Tsujimoto et al. 2011, Ishida et al. 2011). Hence, the smaller flux obtained with *XMM-Newton* by a factor of two is significant. The resultant abundances from the VMCFLOW model are in general greater than those from the CEVMKL model. This is because $T_{\rm max}$ is larger in the VMCFLOW model; a higher temperature in the keV range reduces the volume emissivity of the Kα emission lines from abundant elements in helium-like and hydrogen-like ionization states, and hence requires a larger abundance to explain the observed intensities of those emission lines. The spectral fits with the CEVMKL model result in abundances fairly close to solar values table 6.8), which is consistent with the results of Pandel et al. (2005).

To confirm the mass accretion rates, as well as to estimate their systematic errors, we have attempted to calculate them from the observed bolometric fluxes which are listed in tables 6.7 and 6.6 for the VMCFLOW and CEVMKL models, respectively. Its best-fit values are listed in table 6.9 (the same as in table 6.7). For the conversion to the mass accretion rate, we need the mass and the radius of the white dwarf. The mass of the white dwarf has been estimated as $M_{\rm WD} = 0.63 \pm 0.15 M_{\odot}$ in table 5.1. With this mass, the radius can be obtained from the mass-radius relation of Nauenberg (1972) as $R_{\rm WD} = (8.4^{+1.5}_{-1.2}) \times 10^8$ cm. As a result, the mass

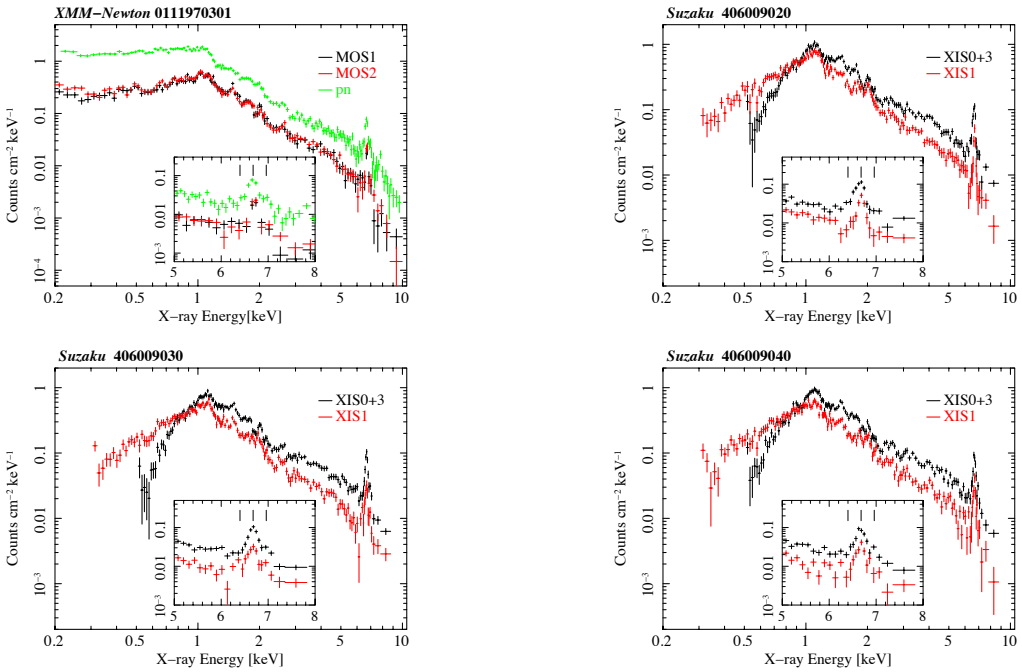

Fig. 6.8 VW Hyi spectra of *XMM-Newton* (seq. #0111979301) and *Suzaku* (seq. #406009020, 406009030, 406009040). Tick marks of insets indicate energies of iron Kα emission lines from neutral, He-like, and hydrogen-like ionization states. Note that ordinate range of *XMM-Newton* main frame is different from that of *Suzaku*.

Table 6.6 Best-fit continuum parameters with the CEVMKL model

Seq. #	406009020	406009030	406009040	0111970301
$N_{\rm H}$ (10^{17} cm^{-2})		6.0† (fixed)		
$\Omega/2\pi$		1.5‡ (fixed)		
i		60°§ (fixed)		
$T_{\rm max}$ (keV)	$5.06^{+0.24}_{-0.23}$	$5.88^{+0.39}_{-0.17}$	$5.77^{+0.16}_{-0.38}$	$5.32^{+0.23}_{-0.22}$
α	$1.90^{+0.12}_{-0.11}$	$1.59^{+0.07}_{-0.10}$	$1.58^{+0.16}_{-0.06}$	$1.45^{+0.07}_{-0.07}$
Flux§§ (10^{-12} erg cm^{-2} s^{-1})				
0.2-12 keV	12.36	10.07	10.35	5.76
Bolometric‖	14.16	11.69	12.01	6.78
Luminosity§§ (10^{30} erg s^{-1})				
Bolometric‖	4.94	4.07	4.19	2.36
χ^2 (d.o.f.)		1623.98 (1283)		

NOTE: All errors are single parameter 90% confidence level.
† Hydrogen column density to VW Hyi (Polidan et al. 1990).
‡ Solid angle of cold matter surrounding the boundary layer (Ishida et al. 2009).
§ Inclination angle of the reflector (primarily accretion disc), which is regarded as identical with the orbital inclination angle (Ritter and Kolb 2003).
§§ The reflected component being excluded (Ω is set equal to zero after the fit converged).
‖ Flux or luminosity in the band 0.04–100 keV.

Table 6.7 Best-fit continuum parameters with the VMCFLOW model

Seq. #	406009020	406009030	406009040	0111970301
$N_{\rm H}$ (10^{17} cm^{-2})		6.0† (fixed)		
$\Omega/2\pi$		1.5‡ (fixed)		
i		60°§ (fixed)		
$T_{\rm max}$ (keV)	$8.61^{+0.17}_{-0.26}$	$8.86^{+0.31}_{-0.22}$	$8.67^{+0.20}_{-0.22}$	$6.95^{+0.20}_{-0.19}$
$\dot{M}$ ($10^{-12} M_{\odot}$yr^{-1})	$2.45^{+0.07}_{-0.05}$	$1.92^{+0.05}_{-0.06}$	$2.02^{+0.05}_{-0.05}$	$1.40^{+0.03}_{-0.03}$
Flux§§ (10^{-12} erg cm^{-2} s^{-1})				
0.2-12 keV	12.63	10.18	10.49	5.81
Bolometric||	14.95	12.07	12.41	6.81
Luminosity§§ (10^{30} erg s^{-1})				
Bolometric||	5.21	4.21	4.33	2.37
χ^2 (d.o.f.)		1818.57 (1287)		

NOTE: All errors are single parameter 90% confidence level.
† Hydrogen column density to VW Hyi (Polidan et al. 1990).
‡ Solid angle of cold matter surrounding the boundary layer (Ishida et al. 2009).
§ Inclination angle of the reflector (primarily accretion disc), which is regarded as identical with the orbital inclination angle (Ritter and Kolb 2003).
§§ The reflected component being excluded (Ω is set equal to zero after the fit converged).
|| Flux or luminosity in the band 0.04–100 keV.

Table 6.8 Best-fit elemental abundances with the VMCFLOW and CEVMKL models

	VMCFLOW	CEVMKL
O	$1.02^{+0.10}_{-0.10}$	$0.93^{+0.10}_{-0.10}$
Mg	$1.56^{+0.18}_{-0.18}$	$1.02^{+0.19}_{-0.18}$
Si	$1.53^{+0.13}_{-0.13}$	$1.18^{+0.13}_{-0.13}$
S	$1.52^{+0.19}_{-0.19}$	$1.12^{+0.17}_{-0.17}$
Ar	$1.71^{+0.53}_{-0.53}$	$1.14^{+0.46}_{-0.45}$
Ca	$1.63^{+0.66}_{-0.67}$	$1.35^{+0.55}_{-0.55}$
Fe	$0.95^{+0.04}_{-0.04}$	$0.90^{+0.04}_{-0.04}$
Ni	$2.49^{+0.53}_{-0.52}$	$1.92^{+0.50}_{-0.49}$

NOTE — Elemental abundances relative to those of the sun (Anders and Grevesse 1989) are tabulated. Abundances of He, C, N, Ne, Na and Al are fixed to unity.

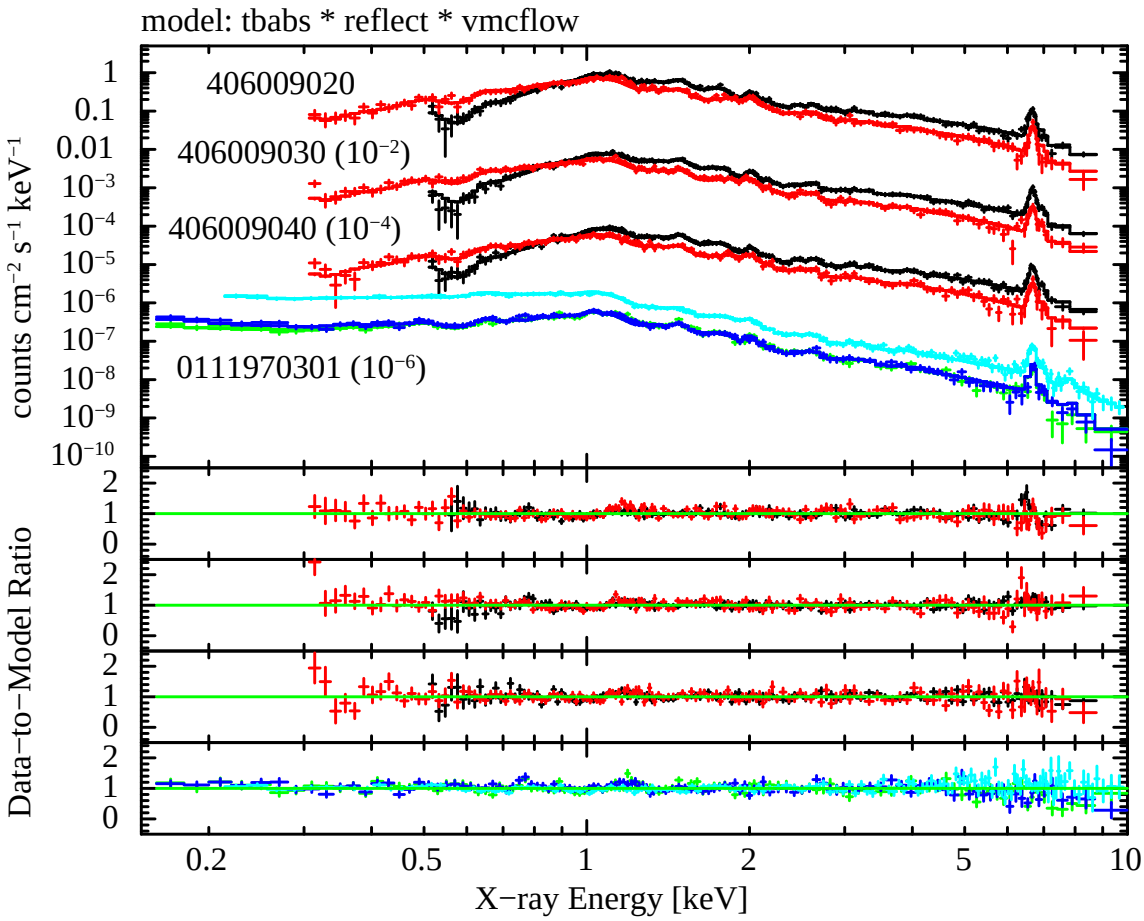

Fig. 6.9 Simultaneous fit of the VMCFLOW model to the *Suzaku* and *XMM-Newton* spectra. Interstellar absorption and the reflection are considered with the models TBABS (($N_{\rm H}$ fixed at 6×10^{17} cm^{-2}; see Polidan et al. 1990) and REFLECT.

Table 6.9 Mass accretion rates in the unit of $10^{-12} M_\odot$ yr^{-1} obtained from the spectral fits.

Model	Source	406009020	406009030	406009040	0111970301
VMCFLOW	model parameter	$2.45^{+0.07}_{-0.05}$	$1.92^{+0.05}_{-0.06}$	$2.02^{+0.05}_{-0.05}$	$1.40^{+0.03}_{-0.03}$
	bolometric flux	$1.67^{+0.03}_{-0.05}$	$1.35^{+0.04}_{-0.03}$	$1.39^{+0.03}_{-0.03}$	$0.86^{+0.03}_{-0.02}$
CEVMKL	bolometric flux	$1.58^{+0.03}_{-0.05}$	$1.30^{+0.04}_{-0.03}$	$1.34^{+0.03}_{-0.03}$	$0.76^{+0.03}_{-0.02}$

accretion rate can be calculated with the following equation.

$$4\pi D^2 f_{\rm bol} \;=\; \frac{1}{2}\,\frac{GM_{\rm WD}\dot{M}}{R_{\rm WD}}, \tag{6.2}$$

where $D = 54$ pc is the distance to the source (table 6.7), $f_{\rm bol}$ is the bolometric flux listed in table 6.7 and 6.6. The factor 1/2 on the right-hand side reflects the fact that half of the accretion energy is lost in the disc before the accreting matter enters the boundary layer. The mass accretion rates thus obtained are listed in table 6.9. They are in the range 54-70% of the best-fit $\dot{M}$ of the VMCFLOW model. Possible reasons for this inconsistency are as follows. First, the model parameter $\dot{M}$ in VMCFLOW, which is based on eq.6.2 assumes a 3D cooling flow geometry whereas the boundary layer is rather close to 2D. As a matter of fact, the CEVMKL model, which can adjust the temperature dependence of DEM, provides a better fit to the spectra. Second, there remains a significant uncertainty in the estimated white dwarf mass. This can, together with the associated $R_{\rm WD}$ uncertainty, result in some 50% uncertainty for $\dot{M}$ calculated from the fluxes. Finally, it is possible that the white dwarf rotates at a non-negligibly high speed compared to the Keplerian velocity at the white dwarf surface. When the accreting matter arrives at the boundary layer, it retains kinetic energy of $(R_{\rm WD}\Omega_{\rm K})^2/2$ per unit mass, where $\Omega_{\rm K}$ is the Keplerian angular velocity on the white dwarf surface in the equatorial plane. Here we neglect the geometrical extent of the boundary layer for simplicity. If the white dwarf does not rotate at all, all this energy should be released in the boundary layer for the matter to settle onto the white dwarf. If, on the other hand, the white dwarf rotates at a finite angular velocity $\Omega_{\rm WD}$, the matter is able to accrete onto the white dwarf by releasing the energy

$$\frac{1}{2}R_{\rm WD}^2\left(\Omega_{\rm K}^2 - \Omega_{\rm WD}^2\right) = \frac{1}{2}\frac{GM_{\rm WD}}{R_{\rm WD}}\left[1 - \left(\frac{\Omega_{\rm WD}}{\Omega_{\rm K}}\right)^2\right]$$

per unit mass. Consequently, the factor $1/2$ in eq.6.2 should be replaced by $(1/2)[1 - (\Omega_{\rm WD}/\Omega_{\rm K})^2]$. The systematic differences apparent in table 6.9 can probably be attributed to these uncertainties and errors.

6.3 Evaluation of a series of SS Cyg data

We have analyzed a series of *XMM-Newton*, *Suzaku* and *NICER* data of the U Gem type dwarf nova SS Cyg in optical quiescence. Example of the spectra obtained by *XMM-Newton*, *Suzaku* and *NICER* are shown in Fig. 6.10. From the inset, Lyα, Heα and the neutral iron Kα lines are recognized in SS Cyg. Accordingly, when evaluating the multi-temperature plasma emission model, we added a reflect model and a 6.4 keV gaussian as the reflection component. The parameters of the REFLECT model were fixed with the solid angle at 1.5 and the inclination angle at 51° (see Table 5.1). We have fitted all 16 sets of data (three from *XMM-Newton*, two from *Suzaku* and eleven from *NICER*) simultaneously. In doing this, we set the metal abundances free to vary but constrained to have common values. In the 2005 *Suzaku* observations, the normalization of HXD-PIN was fixed to be 1.16 times larger than that of XIS0. The best-fit continuum parameters with the VMCFLOW and CEVMKL models are summarized in table 6.10 and 6.11, respectively. The result of the fit with the VMCFLOW model is shown in Fig 6.11 and 6.12. Evaluation with the CEVMKL model shows a wide range of maximum temperatures from 13.93 keV to 23.82 keV (Table 6.11). In addition, the fluxes of the data observed by *NICER* in 2020 are about one order of magnitude higher than those observed by the other satellites at the other moments in 2014, 2016, and 2018. The flux difference between *NICER* and *XMM-Newton* at 3C273 has been found to be less than 1 % (private communication with Dr. Enoto and *NICER* team members). Thus, we consider that the difference in the flux of SS Cyg in quiescence is intrinsic to the source. The resultant elemental abundances with the VMCFLOW model and the CEVMKL model are listed in table 6.12. The abundances of oxygen, magnesium, silicon, sulfur, and iron were almost identical between the two models.

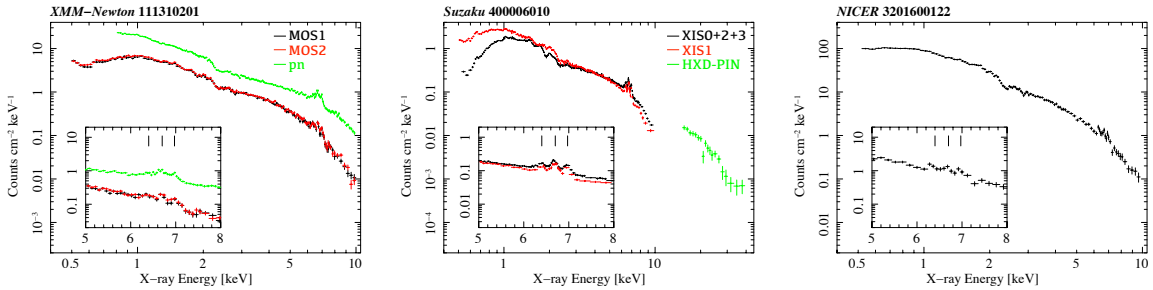

Fig. 6.10 Examples of SS Cyg spectra of *XMM-Newton*, *Suzaku* and *NICER*. Tick marks of insets indicate energies of iron Kα emission lines from neutral, He-like, and hydrogen-like ionization states.

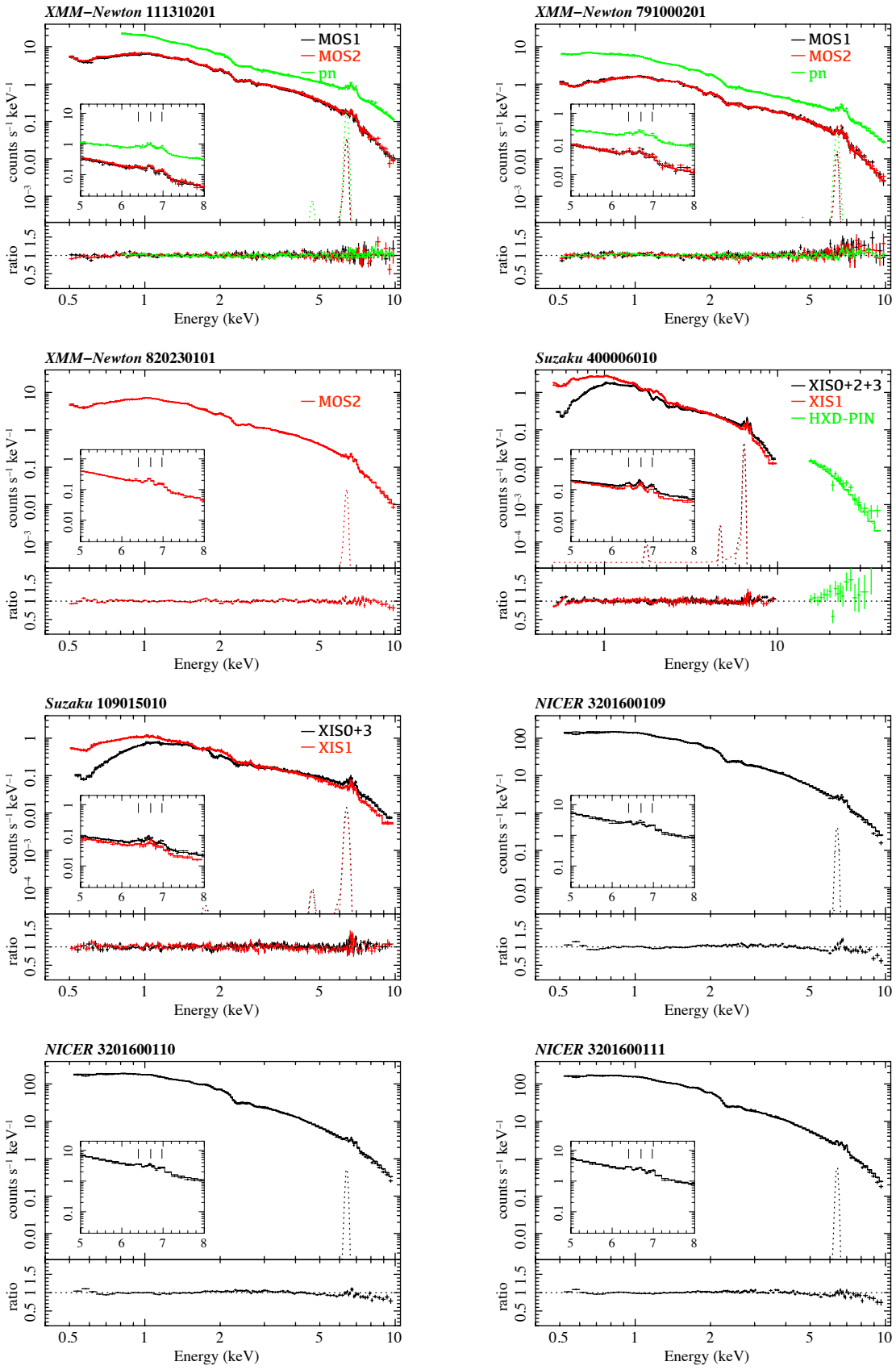

Fig. 6.11 Simultaneous fit of VMCFLOW model to SS Cyg spectra of *XMM-Newton*, *Suzaku* and *NICER*. Tick marks of insets indicate energies of iron Kα emission lines from neutral, He-like, and hydrogen-like ionization states.

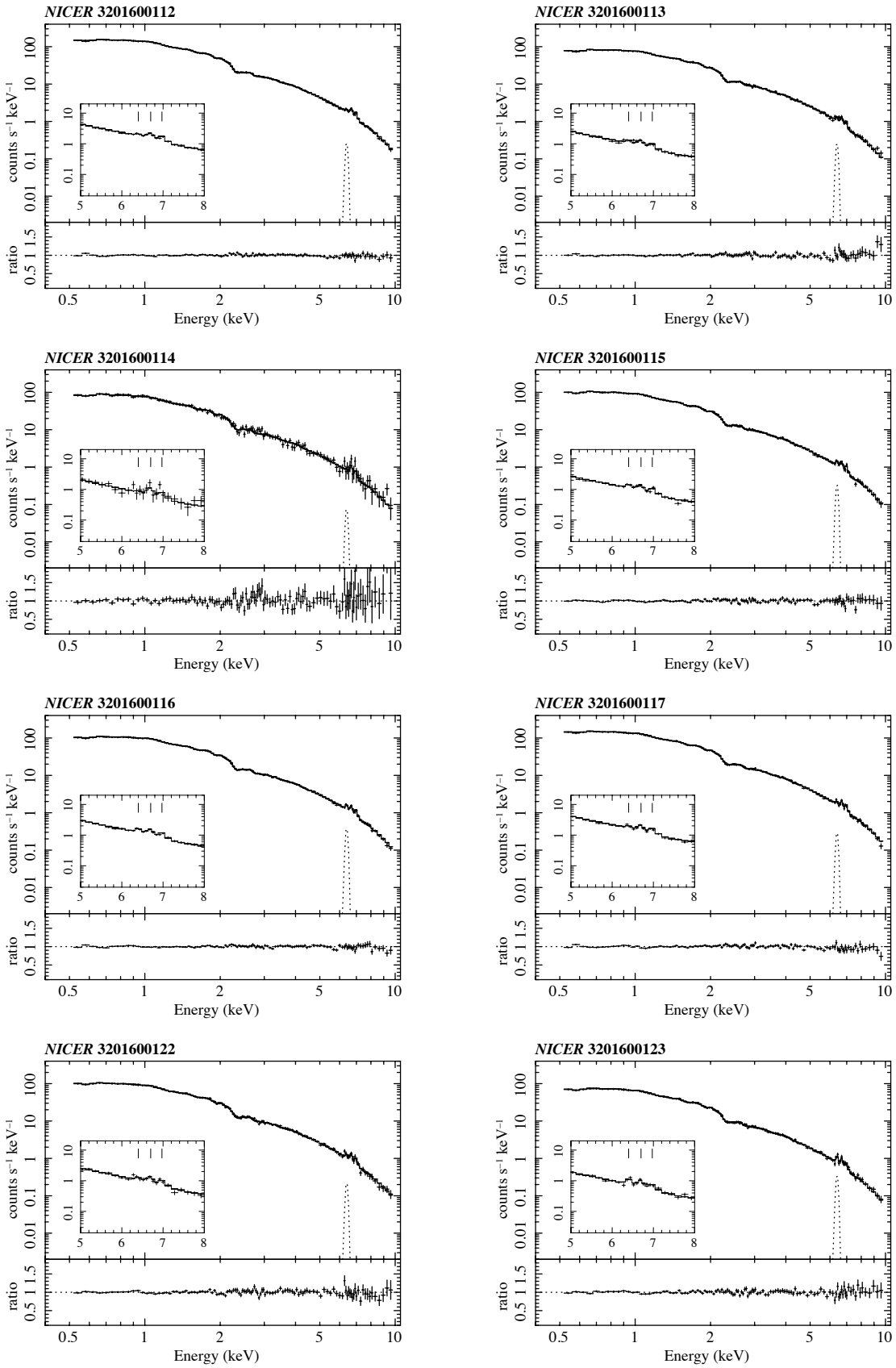

Fig. 6.12 Simultaneous fit of VMCFLOW model to SS Cyg spectra of *NICER*. Tick marks of insets indicate energies of iron Kα emission lines from neutral, He-like, and hydrogen-like ionization states.

Table 6.10 Best-fit continuum parameters with the VMCFLOW model.

Instrument	Seq. #	$N_{\rm H}^{\rm ISM}$ (10^{20} cm^{-2})	$T_{\rm max}$ (keV)	$\dot{M}$ ($10^{-12} M_{\odot}$yr^{-1})	EW (eV)	Flux[§§] 0.2 - 12 keV (10^{-12} erg cm^{-2} s^{-1})	Flux[§§] Bolometric[||] (10^{-12} erg cm^{-2} s^{-1})	Luminosity[§§] Bolometric[||] (10^{30} erg s^{-1})	χ^2 (d.o.f.)
									7263.54 (3193)
XMM-Newton									
	111310201	$0.51^{+0.23}_{-0.23}$	$22.80^{+0.62}_{-0.53}$	$47.39^{+0.84}_{-9.32}$	$43.07^{+0.62}_{-0.55}$	126.04	165.81	261.39 ± 2.08	
	791000201	$0.91^{+0.20}_{-0.20}$	$20.47^{+0.57}_{-0.50}$	$14.28^{+0.28}_{-0.29}$	$59.62^{+0.88}_{-0.89}$	34.40	43.90	69.20 ± 0.55	
	820230101	$1.31^{+0.19}_{-0.19}$	$22.74^{+0.64}_{-0.57}$	$59.30^{+1.10}_{-1.17}$	$23.54^{+0.64}_{-0.87}$	153.65	201.62	317.84 ± 2.53	
Suzaku									
	400006010	$3.09^{+0.20}_{-0.20}$	$21.31^{+0.43}_{-0.42}$	$27.69^{+0.44}_{-0.42}$	$54.27^{+0.68}_{-0.45}$	65.65	85.13	134.19 ± 1.07	
	109015010	$2.32^{+0.35}_{-0.36}$	$19.29^{+0.61}_{-0.56}$	$14.32^{+0.35}_{-0.37}$	$51.41^{+1.10}_{-0.56}$	31.67	39.93	62.95 ± 0.50	
NICER									
	3201600109	$6.23^{+0.16}_{-0.16}$	$53.18^{+2.09}_{-1.88}$	$169.12^{+4.16}_{-4.28}$	$30.77^{+52.07}_{-26.61}$	793.93	1362.40	2147.72 ± 17.08	
	3201600110	$6.37^{+0.13}_{-0.14}$	$53.47^{+1.94}_{-1.52}$	$218.18^{+4.24}_{-5.04}$	$30.16^{+35.02}_{-17.25}$	1027.20	1766.50	2784.75 ± 22.15	
	3201600111	$5.24^{+0.15}_{-0.15}$	$42.19^{+1.50}_{-1.49}$	$208.01^{+5.01}_{-4.71}$	$42.72^{+52.48}_{-3.73}$	825.51	1315.40	2073.63 ± 16.50	
	3201600112	$4.21^{+0.17}_{-0.17}$	$34.76^{+1.21}_{-1.11}$	$195.61^{+4.28}_{-4.33}$	$23.83^{+19.42}_{-23.83}$	674.79	1010.60	1593.13 ± 12.67	
	3201600113	$5.12^{+0.27}_{-0.27}$	$36.54^{+2.22}_{-1.82}$	$107.40^{+3.70}_{-4.03}$	$40.57^{+86.22}_{-40.57}$	381.45	581.85	917.24 ± 7.30	
	3201600114	$3.55^{+0.96}_{-0.92}$	$23.21^{+4.23}_{-3.56}$	$129.96^{+16.54}_{-14.53}$	$14.67^{+283.11}_{-14.67}$	326.76	434.81	685.45 ± 5.45	
	3201600115	$3.95^{+0.26}_{-0.25}$	$28.76^{+1.42}_{-1.33}$	$141.12^{+4.64}_{-4.51}$	$49.97^{+84.69}_{-49.97}$	421.25	595.84	939.30 ± 7.47	
	3201600116	$4.61^{+0.18}_{-0.17}$	$30.19^{+1.59}_{-1.00}$	$150.73^{+3.44}_{-6.67}$	$50.42^{+47.44}_{-46.71}$	463.31	666.76	1051.10 ± 8.36	
	3201600117	$4.03^{+0.19}_{-0.19}$	$32.75^{+1.27}_{-1.29}$	$193.38^{+5.37}_{-4.93}$	$28.36^{+31.88}_{-28.36}$	637.98	938.23	1479.05 ± 11.77	
	3201600122	$3.55^{+0.30}_{-0.32}$	$27.69^{+1.71}_{-1.40}$	$140.78^{+5.17}_{-5.60}$	$33.47^{+74.97}_{-33.47}$	409.62	572.22	902.06 ± 7.18	
	3201600123	$4.28^{+0.27}_{-0.28}$	$27.27^{+1.39}_{-1.23}$	$105.48^{+3.46}_{-3.53}$	$71.76^{+119.11}_{-25.75}$	300.96	419.45	661.23 ± 5.26	

NOTE: Errors of $N_{\rm H}^{\rm ISM}$, $T_{\rm max}$, $\dot{M}$ are single parameter 90% confidence level.
† Parameters of partial covering absorption model.
§§ The reflected component being excluded (Ω is set equal to zero after the fit converged).
|| Flux or luminosity in the band 0.04–100 keV.

Table 6.11 Best-fit continuum parameters with the CEVMKL model.

Instrument	Seq. #	$N_{\rm H}^{\rm ISM}$ (10^{20} cm^{-2})	$T_{\rm max}$ (keV)	α	EW (eV)	Flux[§§] 0.2 - 12 keV (10^{-12} erg cm^{-2} s^{-1})	Flux[§§] Bolometric[||] (10^{-12} erg cm^{-2} s^{-1})	Luminosity[§§] Bolometric[||] (10^{30} erg s^{-1})	χ^2 (d.o.f.)
									6225.59 (3193)
XMM-Newton									
	111310201	2.25 ± 0.27	20.68 ± 0.68	0.70 ± 0.03	40.86	144.30	213.93	337.24 ± 2.68	
	791000201	2.61 ± 0.24	20.23 ± 0.81	0.65 ± 0.03	53.85	39.73	58.01	91.44 ± 0.73	
	820230101	1.74 ± 0.19	17.74 ± 0.53	0.85 ± 0.03	23.97	178.54	255.37	402.57 ± 3.20	
Suzaku									
	400006010	3.96 ± 0.21	17.62 ± 0.38	0.80 ± 0.02	53.61	76.58	109.33	172.35 ± 1.37	
	109015010	1.98 ± 0.35	13.93 ± 0.45	0.99 ± 0.05	52.25	36.78	48.86	77.03 ± 0.61	
NICER									
	3201600109	5.58 ± 0.11	23.58 ± 0.78	1.26 ± 0.04	40.70	937.99	1622.80	2558.22 ± 20.35	
	3201600110	5.62 ± 0.09	22.48 ± 0.91	1.34 ± 0.06	39.97	1210.70	2069.60	3262.57 ± 25.95	
	3201600111	4.75 ± 0.11	20.92 ± 0.81	1.18 ± 0.04	52.57	968.96	1569.90	2474.83 ± 19.69	
	3201600112	4.31 ± 0.14	23.28 ± 0.73	0.92 ± 0.03	27.29	799.00	1304.30	2056.13 ± 16.36	
	3201600113	5.15 ± 0.22	23.82 ± 1.31	0.94 ± 0.04	44.39	452.89	750.99	1183.88 ± 9.42	
	3201600114	4.32 ± 0.84	19.86 ± 4.75	0.77 ± 0.14	12.68	385.61	576.30	908.49 ± 7.23	
	3201600115	4.19 ± 0.21	21.65 ± 1.31	0.87 ± 0.04	49.96	499.15	782.74	1233.93 ± 9.82	
	3201600116	4.93 ± 0.15	23.40 ± 0.73	0.84 ± 0.02	49.40	552.15	892.17	1406.44 ± 11.19	
	3201600117	4.21 ± 0.16	21.88 ± 1.01	0.92 ± 0.04	32.49	751.33	1194.50	1883.04 ± 14.98	
	3201600122	3.91 ± 0.29	22.31 ± 1.96	0.82 ± 0.06	31.77	486.86	766.68	1208.61 ± 9.61	
	3201600123	4.72 ± 0.26	22.26 ± 1.72	0.81 ± 0.05	69.39	357.95	563.42	888.19 ± 7.07	

NOTE: Errors of $N_{\rm H}^{\rm ISM}$, α, $T_{\rm max}$ are single parameter 68% confidence level.
† Parameters of partial covering absorption model.
§§ The reflected component being excluded (Ω is set equal to zero after the fit converged).
|| Flux or luminosity in the band 0.04–100 keV.

Table 6.12 Best-fit elemental abundances with the VMCFLOW and CEVMKL models

	VMCFLOW	CEVMKL
O	$0.34^{+0.01}_{-0.01}$	0.35 ± 0.01
Ne	$0.18^{+0.03}_{-0.03}$	0.26 ± 0.02
Mg	$0.29^{+0.04}_{-0.04}$	0.29 ± 0.02
Si	$0.62^{+0.03}_{-0.03}$	0.60 ± 0.02
S	$0.66^{+0.04}_{-0.04}$	0.61 ± 0.03
Ar	$1.19^{+0.13}_{-0.13}$	1.02 ± 0.09
Ca	$1.11^{+0.17}_{-0.17}$	0.86 ± 0.11
Fe	$0.26^{+0.01}_{-0.01}$	0.28 ± 0.01
Ni	$0.27^{+0.11}_{-0.11}$	0.39 ± 0.07

NOTE — Elemental abundances relative to those of the sun (Anders and Grevesse 1989) are tabulated. Abundances of He, C, N, Na and Al are fixed to unity.

CHAPTER 7

Disccusion

7.1 Correlation between the results of X-ray spectra evaluation and parameters of dwarf nova systems

To understand the physical mechanism at work in the boundary layer, we examined the correlation between its physical parameters obtained from our analysis and those of the DNe listed in table 5.1.

7.1.1 X-ray luminosity

Given the distances from the Gaia Collaboration data release 2 and the bolometric flux estimated from the spectral evaluation, we calculated the bolometric luminosity for each object with eq. 6.1. Figure 7.1 shows the bolometric luminosity evaluated with the CEVMKL model versus the orbital period. There appears to be a correlation between the luminosity and the orbital period. Byckling et al. (2010) analyzed 12 DNe observed by *Suzaku*, *XMM-Newton*, and *ASCA* satellites with cooling flow model and found similar correlations to our results, although they did not take into account the reflection spectral component. From § 6.1, the bolometric luminosity obtained by CEVMKL and VMCFLOW are consistent (Fig. 6.3), and hence, we assume that there is no difference between the models. In the Fig. 7.1, it appears that GW Lib in 2005 is way off compared to GW Lib in 2018. From tables 6.1 and 6.2 in § 6.1, although the spectral parameters are not well constrained, the $T_{\max}$ between the two data agree within 90 % error between 5.6 and 7.1 keV. Also, α, the index of the power law emissivity function of CEVMKL, is almost identical at $\sim$0.7. However, GW Lib in 2005 had a mass accretion rate 1/7 times lower than in 2018. The same applies to SS Cyg and OY Car. On the other hand, the two observations of AB Dra observed in 2002 results in the different α, and the spectrum in June is softer than that in October. According to the optical light curve of AB Dra in the AAVSO, the outburst continued until 6 days before the *XMM-Newton* observation time in October, while in June the outburst continues until 2 days before. This indicates that the boundary layer may not have reached a steady state.

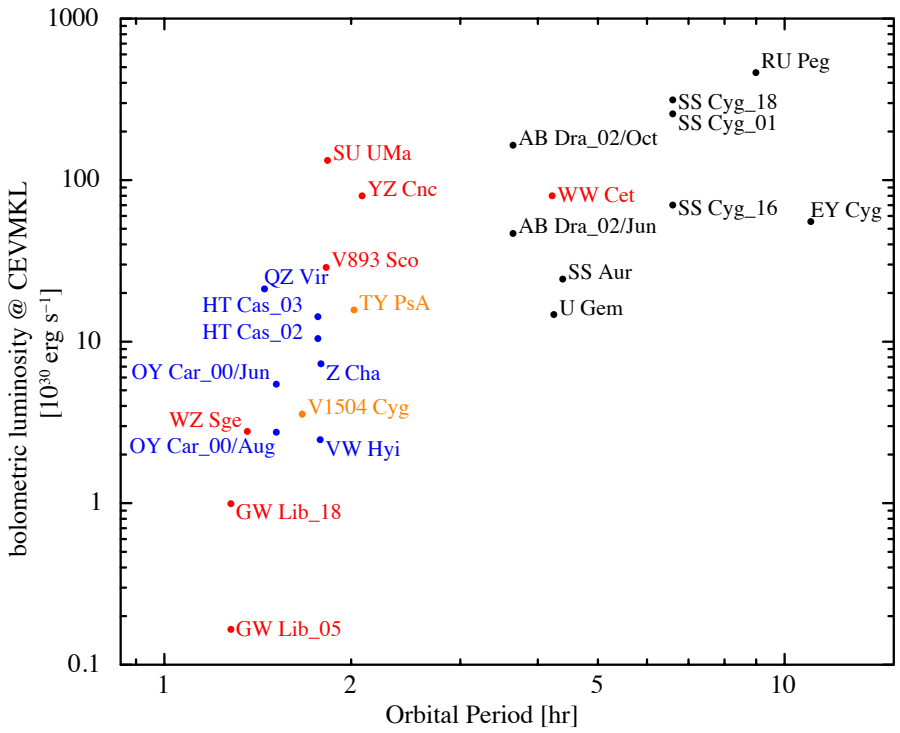

Fig. 7.1 X-ray bolometric luminosities evaluated with CEVMKL model versus orbital period of our sample. Data points are displayed in different colors sorted by white dwarf mass ($M_{\rm WD}$) in table 5.1; black is $M_{\rm WD} \geq 1.0 M_{\odot}$, red is $1.0 M_{\odot} > M_{\rm WD} \geq 0.8 M_{\odot}$, blue is $0.8 M_{\odot} > M_{\rm WD}$, orange represents objects with no white dwarf mass data.

7.1.2 Mass accretion rate in optical quiescent state

Figure 7.2 shows the boundary layer mass accretion rate by VMCFLOW model versus the orbital period. The data points are classified into different colors by the white dwarf mass in table 5.1. In the 19 DNe we analyzed, the mass accretion rates cover the range of $1 \times 10^{-13} M_{\odot}$ yr^{-1} to $8 \times 10^{-11} M_{\odot}$ yr^{-1}. There are at least two studies that have estimated the mass accretion rate in the boundary layer by evaluating the spectra of DNe at quiescence with different cooling flow models. Pandel et al. (2005) analyzed 10 DNe observed with *XMM-Newton* and showed that the mass accretion rates cover almost two orders of magnitude, from $3 \times 10^{-12} M_{\odot}$ yr^{-1} to $1 \times 10^{-10} M_{\odot}$ yr^{-1} although they were not able to show any clear trend between the mass accretion rate and the orbital period. Wada et al. (2017) reported that the mass accretion rates of 15 DNs observed with *Suzaku* cover the range from $5 \times 10^{-13} M_{\odot}$ yr^{-1} to $9 \times 10^{-11} M_{\odot}$ yr^{-1}. However, these results did not take into account the reflection spectral component. In addition, now we are able to utilize distance estimates from the Gaia Collaboration data release 2, released in December 2018, which is of essential importance to enhance the accuracy of our mass accretion rate estimates. We therefore believe that our mass accretion rate estimates are much more reliable that those from the previous works.

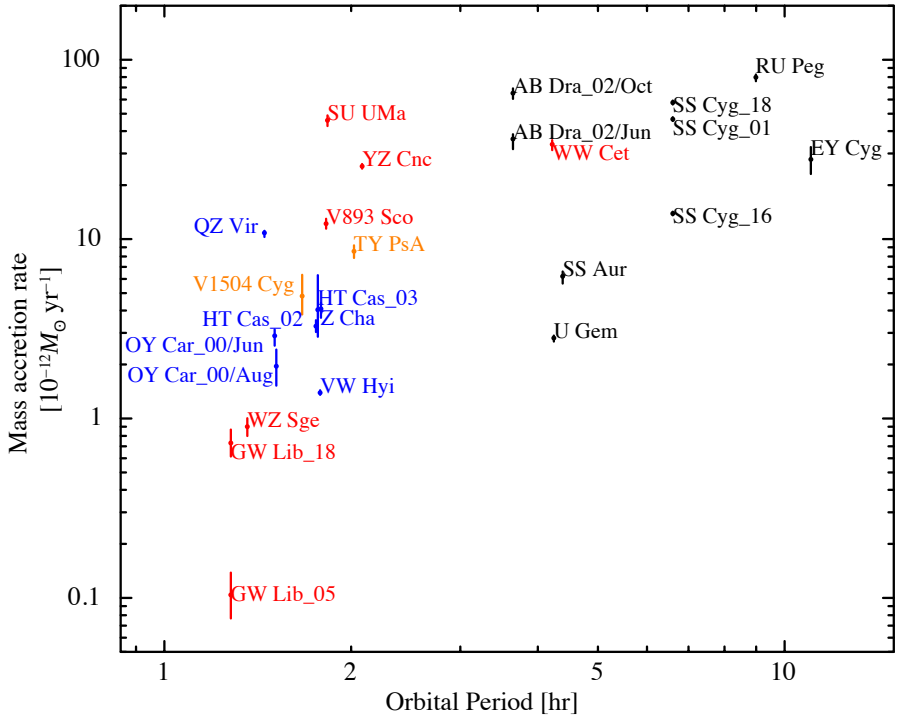

Fig. 7.2 Orbital period versus mass accretion rate ($\dot{M}$) of boundary layer observed with *XMM-Newton*. Source sample with 90 percent uncertainties for $\dot{M}$. Data is classified by white dwarf mass ($M_{\rm WD}$) in table 5.1, black is $M_{\rm WD} \geq 1.0 M_{\odot}$, red is $1.0 M_{\odot} > M_{\rm WD} \geq 0.8 M_{\odot}$, blue is $0.8 M_{\odot} > M_{\rm WD}$, orange is no data.

From Fig. 7.2, it is shown that the mass accretion rate of the boundary layer decreases

with the orbital period. This correlation is reminiscent of that found by Warner (1987) for the absolute visual magnitudes of the DN disks at minimum light. We have compared the mass accretion rates of the boundary layer and the accretion disk. As a theoretical model for the mass accretion rate in the disk, we utilized the following equation for the accretion rate during outburst (Cannizzo 1993),

$$\dot{M} = 1.1 \times 10^{-8} M_{\odot} \mathrm{yr}^{-1} \left(\frac{\alpha_{\mathrm{H}}}{0.1}\right)^{1.14} \left(\frac{\alpha_{\mathrm{C}}}{0.02}\right)^{-1.23} \left(\frac{f}{0.4}\right)^{1.43} \left(\frac{r_d}{4 \times 10^{10}}\right)^{2.57}. \quad (7.1)$$

The equation is derived based on the standard disk model and their parameters are adjusted with the limit cycle of the dwarf star SS Cyg, where α_{H} and α_{C} are the viscosity during outburst and quiescence, respectively, f is the scale factor of the disk mass, and r_d is the maximum radius of the quiescent disk just before the onset of an outburst. Based on the observations of SS Cyg, we set $\alpha_{\mathrm{H}} = 0.1$, $\alpha_{\mathrm{C}} = 0.02$, $f = 0.4$. Since the quiescent disk radius was determined as r_d/a = 0.29 for U Gem (Smak 1984*b*), 0.31 for WZ Sge (Smak 1993), and 0.313 for OY Car (Wood et al. 1989), we adopted r_d/a = 0.30 based on the empirical results. Substituting eq.2.1, 2.5 and 2.6 into eq.7.1, we can express $\dot{M}$ in terms of white dwarf mass and orbital period. In quiescence, on the other hand, it is known from observations that dwarf novae are in general fainter than in outburst with a V-magnitude of 2 to 5. We therefore draw a model accretion rate curve in quiescence by scaling eq. 7.1 with this factor. Figure 7.3 shows the accretion rate during outburst as a pair of dashed lines. Magenta and green curves represent $M_{\mathrm{WD}} = 0.6 M_{\odot}$ and $= 1.2 M_{\odot}$ cases, respectively. The dashed-dotted lines and dotted lines show the mass accretion rate in quiescence, which correspond to $\Delta m_{\mathrm{V}} = 2$ (a factor of 6.3) and $= 5$ (a factor of 100), respectively. The figure shows that the observed accretion rate of the boundary layer at quiescence is about one order of magnitude lower than that of the disk.

One possible reason for this is that the white dwarf has a large rotation velocity and the accreting matter settles onto the white dwarf before releasing all remaining energy. The reduction factor is $[1 - (\Omega_{\mathrm{WD}}/\Omega_{\mathrm{K}}(R_{\mathrm{WD}})]^2$. To verify this hypothesis, we have corrected the mass accretion rate of the boundary layer for objects with known rotation velocities, which are listed in the table 7.1. The apparent V magnitude during the quiescence was referred to from the optical light curve taken from the homepage of the American Association of Variable Star Observers (AAVSO)[1]. For the apparent V magnitude in outburst, we adopted the maximum brightness of the normal outburst in the cataclysmic star catalog Ritter and Kolb (2003). With these parameters and the rotational velocity of the white dwarf, we corrected the theoretical mass accretion rate of the boundary layer, by multiplying $[1 - (\Omega_{\mathrm{WD}}/\Omega_{\mathrm{K}}(R_{\mathrm{WD}})]^2$, to obtain $\dot{M}_{\mathrm{BL}}$ in table 7.1, which is in general much smaller than the observed mass accretion rate determined with the VMCFLOW model. As a result, the effect of the rotation velocity of the white dwarf is not enough to confirm the observed results. We suggest that there is a mechanism that causes the

[1] https://www.aavso.org

gas to be released during accretion from the disk to the white dwarf.

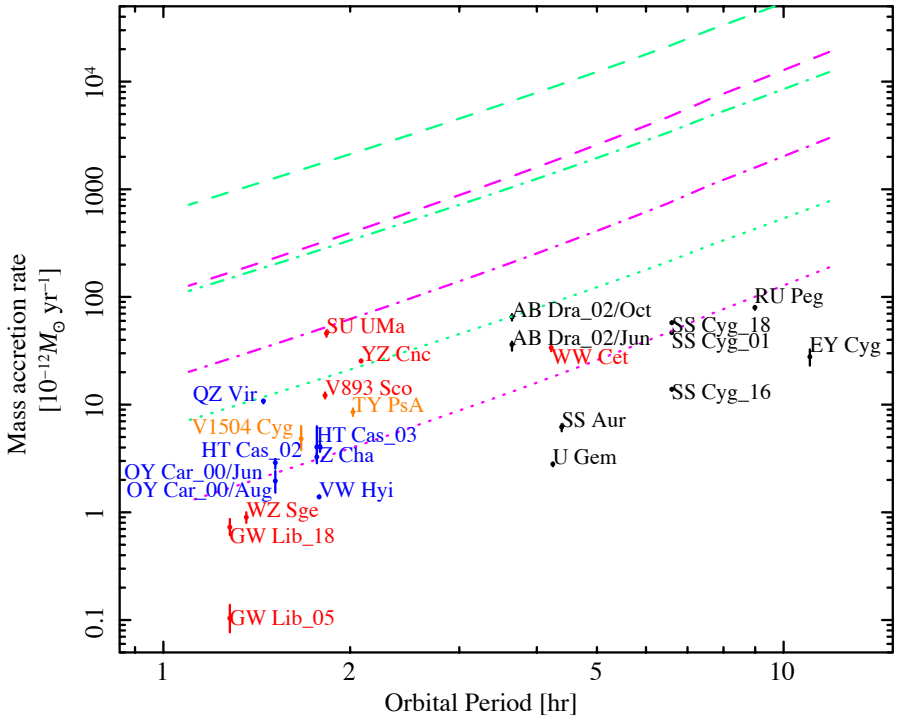

Fig. 7.3 Dashed lines are mass accretion rate model of disk at outburst phase (eq. 7.1). Dashed-dotted lines and dotted lines show mass accretion rate at quiescence, which is 2 orders and 5 orders of magnitude darker than outburst, respectively. (Magenta : $M_{\rm WD} = 0.6M_\odot$, Green : $M_{\rm WD} = 1.2M_\odot$). Data points are displayed in different colors with the white dwarf mass, which is the same was as in Fig.7.2.

7.1.3 Plasma temperature of the boundary layer.

We have plotted the maximum plasma temperature ($T_{\rm max}$) estimated from the spectral analysis versus the orbital period of the object in Fig 7.4. There seems to be a correlation between the $T_{\rm max}$ and the orbital period. In particular, the objects with a larger mass white dwarf seem to have higher $T_{\rm max}$. We therefore plotted the maximum temperature of the boundary layer versus the mass of the white dwarf in Fig. 7.5, and compared them with the theoretical temperature of the post-shock gas (eq. 2.40) that has experienced a strong shock. TY PsA and V1504 Cyg, for which no white dwarf mass data are available, are omitted. Figure 7.5 shows a clear correlation between $T_{\rm max}$ estimated from the CEVMKL model and the white dwarf mass. $T_{\rm max}$ is also observed to be about 40 % lower than the theoretical temperature after the shock. This suggests that strong shock does not necessarily occur in the boundary layer of DN because the mass flow in the disc is probably highly oblique to the shock front. On the other hand, $T_{\rm max}$ estimated from the VMCFLOW model shows a large scatter among objects with similar white dwarf masses. In the VMCFLOW model, the temperature dependence

Table 7.1 Calculated mass accretion rate at quiescent phase boundary layer

Object	$M_{\rm WD}$	$P_{\rm orb}$	$V^{\rm q\dagger}$	$V^{\rm OB\ddagger}_{\rm min}$	$\dot{M}^q_{\rm disk}$	$\Omega_{\rm WD}$	$\Omega_{\rm K}(R_{\rm WD})$	$\dot{M}^q_{\rm BL}$	$\dot{M}^q_{\rm BL}$ (VMCFLOW)
	($M_\odot$)	(hr)	(mag)		($10^{-12}M_\odot$ yr^{-1})	(km s^{-1})		($10^{-12}M_\odot$ yr^{-1})	($10^{-12}M_\odot$ yr^{-1})
RU Peg	1.06 ± 0.04	8.99	12.5	9.5	2068.40	40^{+30}_{-15} [a]	4538.85	2032.13	$79.80^{+2.93}_{-3.89}$
SS Cyg_01	1.19 ± 0.02	6.60	12.0	8.2	647.57	200 [b]	4902.76	595.82	$46.64^{+1.18}_{-1.10}$
SS Cyg_16	–	–	12.1	–	590.59	–	–	543.39	$13.90^{+0.33}_{-0.33}$
SS Cyg_18	–	–	12.0	–	647.57	–	–	595.82	$57.72^{+1.51}_{-1.47}$
SS Aur	1.08 ± 0.40	4.39	15.2	10.5	97.63	400 ± 100 [a]	4595.77	81.37	$6.20^{+0.40}_{-0.55}$
U Gem	1.20 ± 0.05	4.25	14.1	8.6	55.99	100 ± 30 [c]	4930.18	53.74	$2.81^{+0.09}_{-0.12}$
WW Cet	0.83 ± 0.16	4.22	14.7	10.5	57.88	600 ± 100 [d]	3855.92	41.27	$33.74^{+1.89}_{-2.43}$
VW Hyi	0.63 ± 0.15	1.78	13.8	9.5	7.11	400 ± 100 [a]	3208.51	5.45	$1.39^{+0.05}_{-0.04}$
WZ Sge	0.85 ± 0.04	1.36	15.0	11.2	22.13	1200^{+300}_{-400} [e]	3917.61	10.65	$0.90^{+0.10}_{-0.10}$

† Obtained from the homepage of the American Association of Variable Star Observers (AAVSO).
‡ The parameters are from "Catalogue of Cataclysmic Binaries, Low-Mass X-Ray Binaries, and Related Objects Edition 7.24" (Ritter and Kolb 2003).
[a] From Godon et al. (2008)
[b] From Sion et al. (2010)
[c] From Sion et al. (1998)
[d] From Godon et al. (2006)
[e] From Cheng et al. (1997)

of the emission measure is automatically determined by the plasma cooling function. Since the CEVMKL model, which represents the DEM as a power law function of temperature, fits the spectra better with smaller χ^2 values, we consider that the VMCFLOW model developed for galaxy clusters does not necessarily reproduce the temperature dependence of DNe.

7.2 Variation of mass accretion rate onto the white dwarf

7.2.1 VW Hyi

7.2.1.1 Evolution of $\dot{M}$ with supercycle phase

In Fig. 7.6 we show a time history of the mass accretion rate evaluated in § 6.2 with the V-magnitude light curves drawn since the onset of the last superoutburst before the *Suzaku* and *XMM-Newton* observations. Here we plot the best-fit parameter $\dot{M}$ of VMCFLOW listed in Table 6.7. We have added a few more data points from past observations. Of the two *ASCA* points, the first one comes from the observation carried out in 1993 November, which is presented in Baskill et al. (2005). We have reanalysed the data to find that our bolometric flux coincides with theirs within 10%. The other is taken from the observation in 1995 March, which has never been published. We have processed the data in the same way as the first *ASCA* observation, and have found that VW Hyi was extremely faint. We plot the best-fit $\dot{M}$ of the VMCFLOW model for both *ASCA* datasets. The third data point originates from the *Ginga* and *ROSAT* observation which is published by Wheatley et al. (1996). The authors of this paper fitted the contemporaneous *Ginga* and *ROSAT* spectra with a two component thermal bremsstrahlung model. We

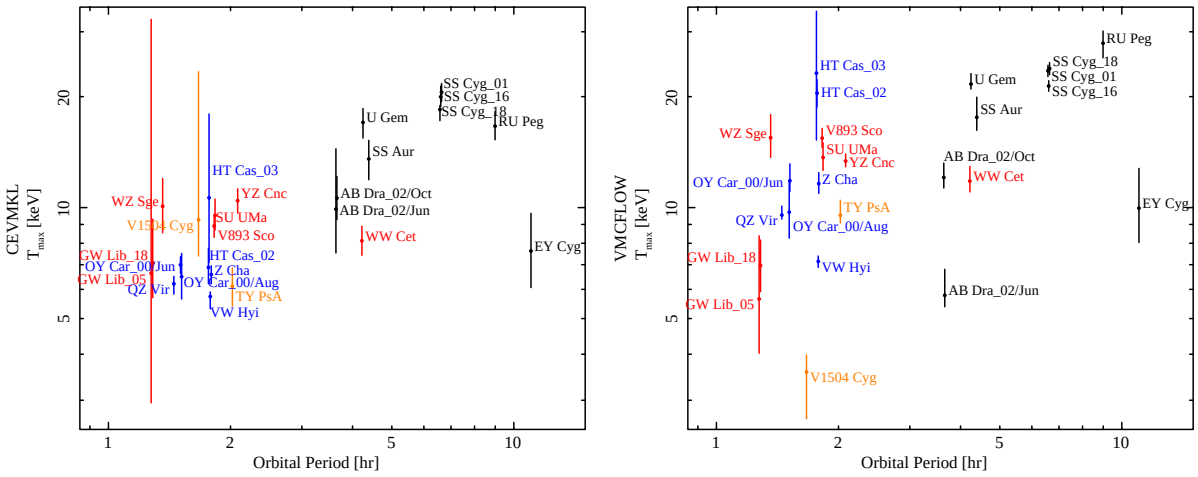

Fig. 7.4 Orbital period versus maximum temperature of plasma ($T_{\rm max}$) obtained by (left panel) CEVMKL model and (right panel) VMCFLOW model. Source sample with 90 percent uncertainties for $T_{\rm max}$. Data is classified by white dwarf mass ($M_{\rm WD}$) in table 5.1, black is $M_{\rm WD} \geq 1.0 M_{\odot}$, red is $1.0 M_{\odot} > M_{\rm WD} \geq 0.8 M_{\odot}$, blue is $0.8 M_{\odot} > M_{\rm WD}$, orange is no data.

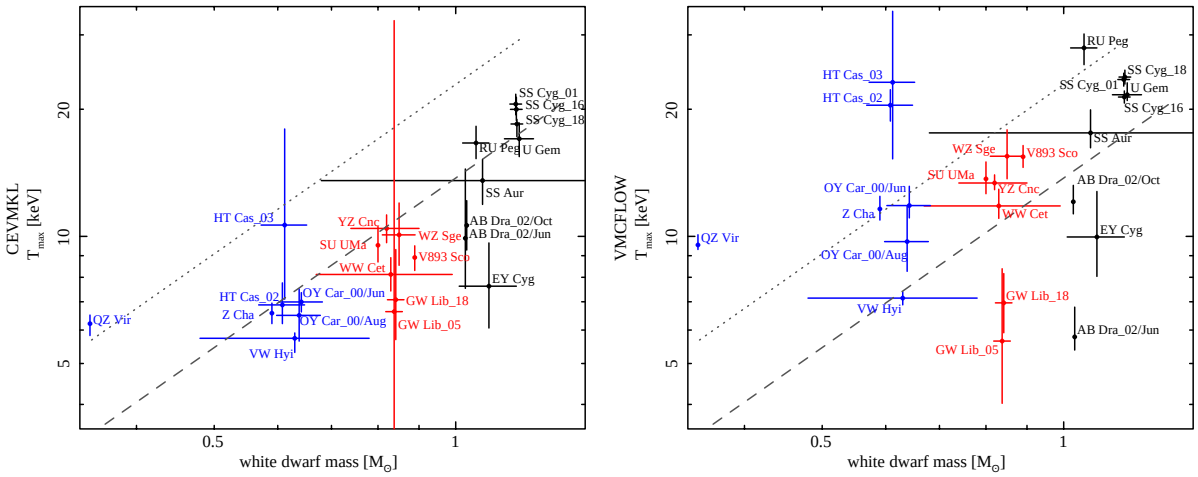

Fig. 7.5 Maximum temperature of plasma ($T_{\rm max}$) obtained by (left panel) CEVMKL model and (right panel) VMCFLOW model versus white dwarf mass. Source sample with 90 percent uncertainties for $T_{\rm max}$. Gray dotted and dashed lines are theoretical temperature of the post-shock gas having experienced the strong shock and its reduction by 40 %, respectively.

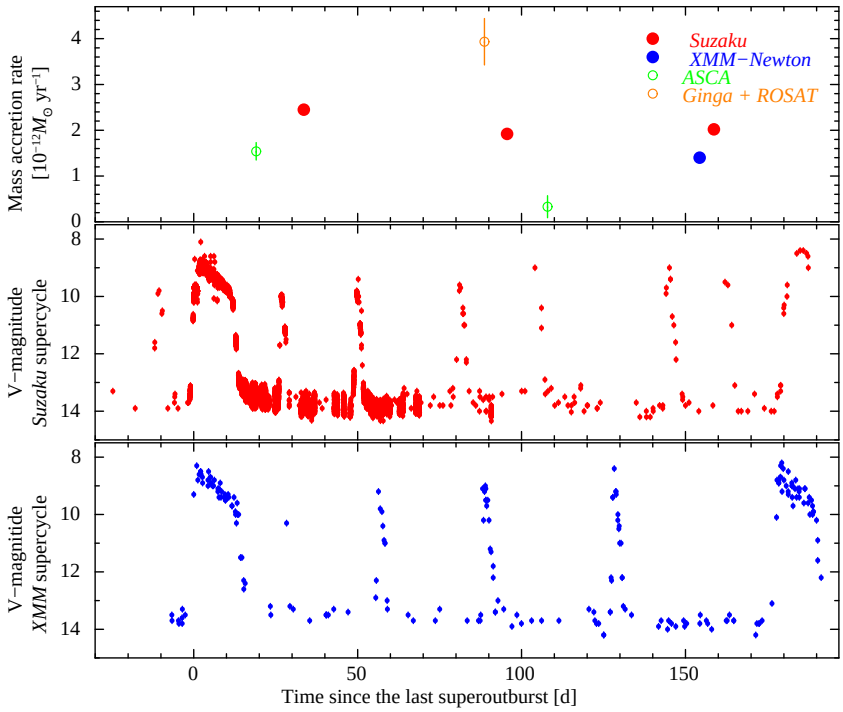

Fig. 7.6 Time history of mass accretion rate, VMCFLOW parameter $\dot{M}$, since last superoutburst. Filled circles coloured with red and blue in top panel are from *Suzaku* and *XMM-Newton*, respectively. Open circles coloured with green and orange are from *ASCA* observations (Baskill et al. 2005) and contemporaneous *Ginga+ROSAT* observations (Wheatley et al. 1996), respectively. Middle and bottom panels show V-magnitude light curve corresponding to same supercycles of the *Suzaku* and *XMM-Newton* observations.

have calculated the bolometric flux from their best-fit model parameters, and derived the mass accretion rate through eq. (6.2). In converting this to the VMCFLOW parameter $\dot{M}$, we refer to the conversion factor 54%-70% from the VMCFLOW parameter $\dot{M}$ to the flux-based $\dot{M}$ (§ 6.2). We would like to remark, however, that this *Ginga+ROSAT* observation was carried out only a few days after the onset of an outburst, and the hard X-ray counting rate had been increasing systematically (see Fig. 1 of Wheatley et al. 1996). This implies that the boundary layer had not reached a steady state.

At first sight of the four data points from the *Suzaku* and *XMM-Newton* observations, there seems a steady decline of the mass accretion rate as time passes. Although the first *Suzaku* observation has the highest mass accretion rate of the four, the second *Suzaku* observation gives a similar mass accretion rate as the third observation, which was carried out some 60 days after the second. Moreover, the mass accretion rate from the *XMM-Newton* observation, which was performed at nearly the same epoch as the third *Suzaku* observation, is smaller than that of the third *Suzaku* observation by $\sim$30%. As noted in § 6.2, disagreement of fluxes measured with *Suzaku* and *XMM-Newton* detectors is less than 10% (Tsujimoto et al. 2011, Ishida et al. 2011). Hence this flux disagreement is real. Although the three *Suzaku* observations and the *XMM-Newton* observation belong to different supercycles, we conclude that there is no clear trend in the mass accretion rate as a function of the time since the eruption of a superoutburst.

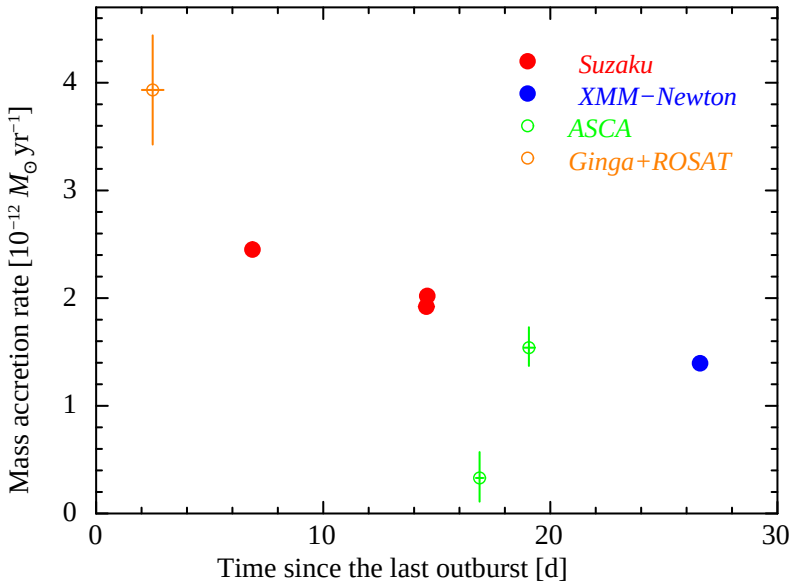

Fig. 7.7 Evolution of mass accretion rate as function of time since last outburst. Symbols of data points are same as those in Fig. 7.6.

This conclusion holds, or is even reinforced, with the *ASCA* and *Ginga* + *ROSAT* data points being included.

We remark that, in SU UMa type DNe, the total mass of the accretion disc increases between two superoutbursts (Osaki 1996). As the disc accumulates mass, its surface density is expected to increase as time passes, and hence the mass accretion rate also increases. Such a systematic increase of the mass accretion rate is not evident from the current *Suzaku* and *XMM-Newton* observations.

7.2.1.2 Evolution of $\dot{M}$ in the outburst cycle

In Fig. 7.7, we have plotted the mass accretion rate as a function of the time since the last outburst (including the superoutburst). In contrast to Fig. 7.6, this shows a clear decreasing trend of the mass accretion rate, except for the extremely low mass accretion rate in the second *ASCA* observation.

There are at least a couple of previous works that suggest decline of the hard X-ray flux during optical quiescence. McGowan et al. (2004) analysed four sets of *RXTE* PCA data of SS Cyg, each of which encompass $\sim$2 weeks to a few months. They found that the X-ray counting rate in the band 1.3–12.2 keV declines at a rate of 1.3% d^{-1}, accumulating 40% decrease in 31 days since the instance when SS Cyg gets fainter than $m_{\rm V} = 11.7$ mag. Collins and Wheatley (2010) found that the X-ray counting rate of SU UMa in quiescence in the band 2.0-18.5 keV observed with the *RXTE* PCA decreases at a rate of 0.09 counts s^{-1} d^{-1} from 5.8 counts s^{-1}, which implies -1.6% d^{-1}, similar to SS Cyg. The decline of the mass accretion rate in the current dataset of VW Hyi is 43% in $\sim$20 d, implying the rate of -2.2% d^{-1}. This is of the same order as the previous two works, although our method differs from these

previous works in that we directly derived the accretion rate from the X-ray spectra obtained by spectroscopic observations. This is the first study to establish that the accretion rate to a white dwarf is directly measured and verified to be decreasing in time during optical quiescence.

The authors of these two previous works mentioned that the global decline of the mass accretion rate within the boundary layer during the quiescent phase (inter-outburst period) conflicts with the expectation of the disc instability model, which predicts increasing accretion rate during quiescence (e.g. Lasota 2001). One may invoke retardation of mass transfer through the disc. Mineshige and Osaki (1985) showed in their disk instability simulation that the outburst is triggered by a heating wave that is initiated in the outer part of the disc and travels inward. The expected delay of an outburst in the EUV band is really detected in SS Cyg; Wheatley et al. (2003) found that the rise of the EUV flux is retarded from the onset of the optical outburst by 1.5-2 d. Collins and Wheatley (2010) found that in SU UMa the hard X-ray suppression, which is expected to occur simultaneously with the EUV outburst, is retarded by 0.57 d on the average from the onset of the optical outburst. These results indicated that it takes $\sim$1 day for the heating wave to reach the boundary layer from the optically bright part of the disk. Since the quiescent disc is expected to have much lower density, the time necessary for physical quantities to propagate through the disc should be much longer.

Finally, we briefly mention the extremely faint state of VW Hyi observed with *ASCA* in March 1995. VW Hyi was so faint and the mass accretion rate at that time was much lower than the declining trend shown in Fig. 7.7. Although the spectral parameters are not constrained very well, the *ASCA* spectrum in 1995 is fitted with the CEVMKL model with $T_{\rm max} = 8.13^{+3.71}_{-2.20}$ keV. The spectrum seems much harder than the other quiescence spectra presented in this paper. This can be attributed to a lower mass accretion rate, resulting in lower cooling efficiency of the plasma. The reason for VW Hyi to fall into such a low state should be pursued in the future.

7.2.2 SS Cyg

As a result of analyzing multiple data sets from VW Hyi, we confirmed that the accretion rate to the white dwarf tends to decrease with time since the onset of the last outburst. Accordingly, we carried out the same analysis to multiple data sets of SS Cyg, a U Gem-type dwarf nova. The left panel of Fig. 7.9 shows the mass accretion rate from *XMM-Newton*, *Suzaku* and *NICER* observations as a function of the time since the onset of last outburst as in Fig. 7.7. The V-magnitude light curves drawn since the onset of the last outburst before the each observation are shown in the right panel of Fig. 7.9 . Although there is a large scatter, the mass accretion rate of SS Cyg shows on the whole an exponential decreasing trend. On the other hand, the V-magnitude at the time of the *XMM-Newton* and *Suzaku* observations was about 12, while that of *NICER*'s was different, at about 11. Hence, the volume of gas accreted in the disk is probably different.

We first evaluated the mass accretion rate obtained from the *XMM-Newton* and *Suzaku*

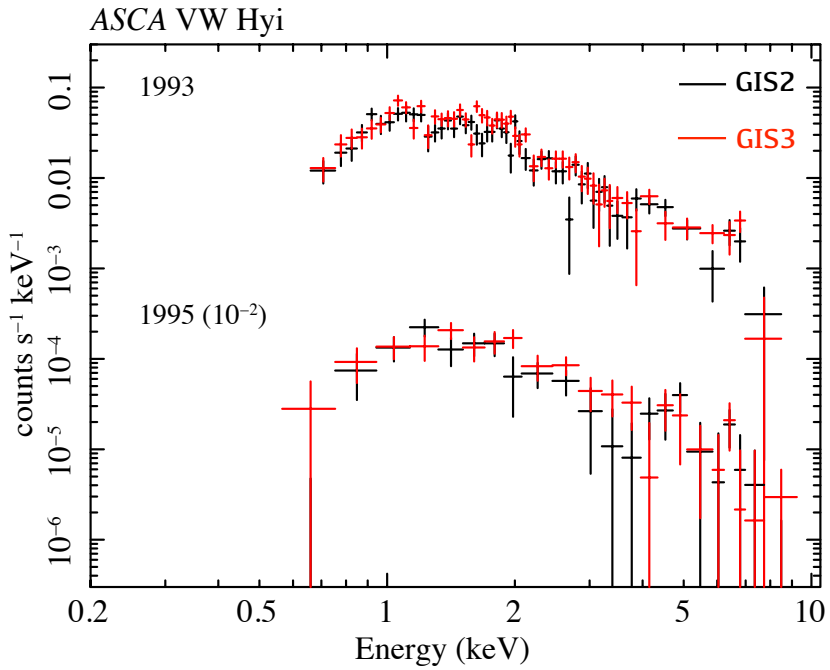

Fig. 7.8 VW Hyi spectra of *ASCA* in 1993 and 1995.

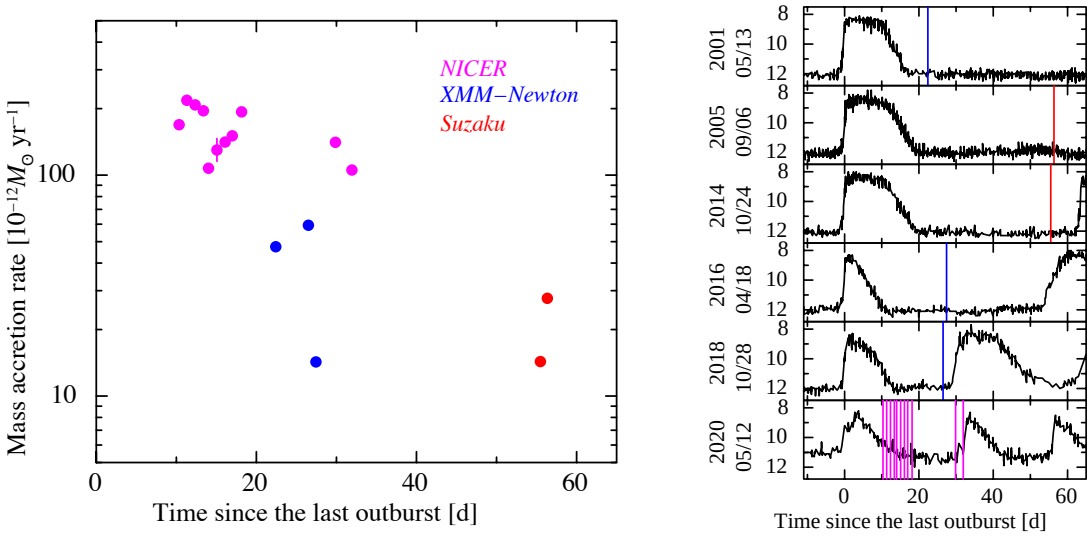

Fig. 7.9 Time history of mass accretion rate, VMCFLOW parameter $\dot{M}$, since last outburst. Filled circles colored with red, blue and magenta in left panel are from *Suzaku*, *XMM-Newton* and *NICER*, respectively. Right panel show V-magnitude light curves corresponding to same cycles of the *Suzaku*, *XMM-Newton* and *NICER* observations.

observations. In Fig. 7.10, we have plotted the mass accretion rate as a function of the time since the last outburst. Except for the low mass accretion rate in the 2016 *XMM-Newton* observation, the mass accretion rate shows a clear declining trend at a rate of -2.6 to -1.2 % d^{-1}. This result confirms the decrease rate of 1.3 % d^{-1} calculated from the 1.3–12.2 keV count rate of SS Cyg in McGowan et al. (2004). Next, we plotted the mass accretion rate and the bolometric luminosity derived with the *NICER* observation as a function of the time since the last outburst. The bottom panel in Fig.7.11 shows the V-magnitude light curve at the time of the *NICER* observations. Figure 7.11 shows that the mass accretion rate has halved in one day at around the 14 th day since the last outburst. During the same period, the bolometric luminosity also decreased significantly. In Figure 7.8, the V-magnitude light curve shows that it takes more time to increase from quiescence to the maximum magnitude when observed with *NICER* than when observed with *XMM-Newton* and *Suzaku*. This is a characteristic of the inside-out outburst. In the inside-out outburst, the disk starts thermal instability radially from inside to outside, so the transition is slower than in the outside-in outburst, and the light curve has a rounded shape. In addition, the inside-out outburst is predicted to return to the quiescent state while re-flaring repeatedly (Menou et al. 2000, Lasota 2001). We argue that the luminosity plunge seen in the Fig.7.11 is due to re-flaring. Using only the data with the highest mass accretion rate (sequence # 3201600110) and the last two data (sequence # 3201600122 and 3201600123), we evaluated the mass accretion rate obtained from the *NICER* observations. The mass accretion rate shows a decreasing trend at a rate of -2.5 to -1.9 % d^{-1}. This result is within the range of decreasing rates calculated using *XMM-Newton* and *Suzaku* data.

7.3 Structure of the boundary layer in quiescence

Our analysis shows that the mass accretion rate observed at the boundary layer declines during optical quiescence, which seems in contradiction to the prediction of the theoretical model of the accretion disk. Theoretical models of the boundary layer are complicated because of the strong shear and turbulence of the accretion flow. Meyer and Meyer-Hofmeister (1994) suggests that the gas is spread out like a corona at the inner edge of the disk in quiescent dwarf novae, and evaporates in siphon flow by heating through thermal conduction. They assume that the observed X-rays radiate from the boundary layer and the corona that stays above the accretion disk. The gas in the forming corona is partially accreted onto the white dwarf and partially lost in a flow. Progressively, the inner radius of the disk moves outward with time, and the coronal flow decreases accordingly. This model seems to represent the decrease in UV flux after the outburst of VW Hyi observed by *International Ultraviolet Explorer*.

On the other hand, in order to reconcile the mass accretion rate decline in quiescence with the standard disc instability model, one may presume that the optically thick disc survives close to the orbital plane even in the optically-quiescent state, being covered with an optically thin boundary layer. Since there must be some density gradient in the disc in the direction

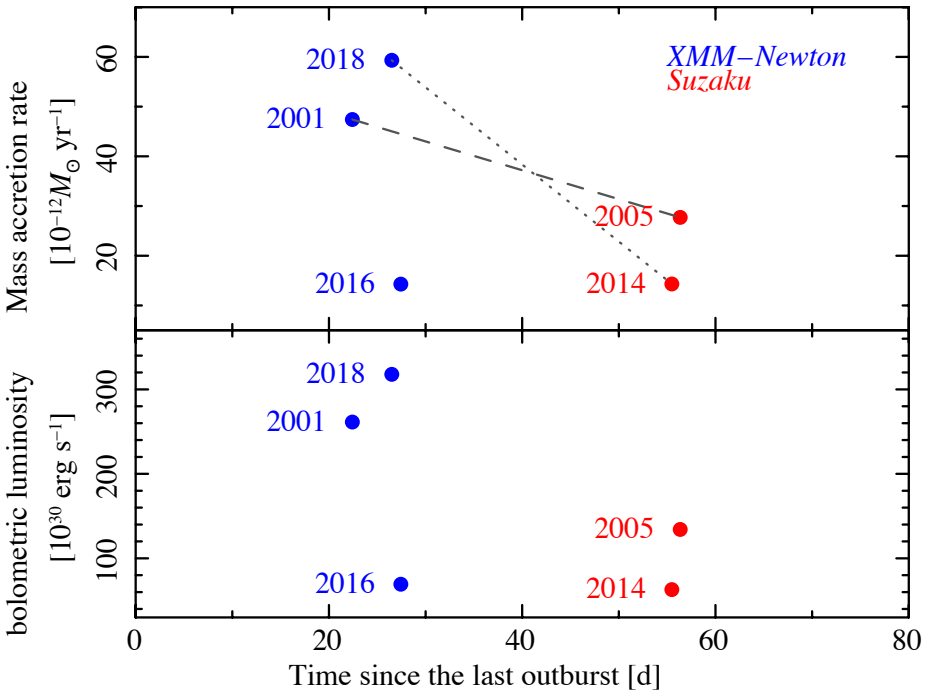

Fig. 7.10 Evolution of mass accretion rate and bolometric luminosity of SS Cyg observed by *XMM-Newton* and *Suzaku* as function of time since last outburst. Gray dotted and dashed lines are decrease rate of -2.6 % d^{-1} and -1.2 % d^{-1}, respectively.

perpendicular to the orbital plane, such a geometry may be possible. As the mass accretion rate increases, this optically thick boundary layer grows and consumes a larger fraction of the accretion energy, resulting in the apparent decline of $\dot{M}$ in the hard X-ray band. The emission from such a disc is expected to appear in the EUV band, being somewhat Comptonized by the overlying optically thin hot plasma. Such a spectral component, however, has not been detected so far; we should confess that such an optically thick component of the boundary layer in quiescence is just speculation at this moment.

Finally, the standard disk instability model (e.g. Lasota (2001)) may need to be modified. Although the model predicts an increase of the mass accretion rate through the disk in quiescence, the optical magnitude seems fairly constant throughout the quiescence phase (see Fig. 7.6 and 7.9). The optical flux originates not only from the accretion disc but also from the white dwarf and the secondary star. Of them, the emission from the white dwarf may decline during quiescence due to cooling after the outburst. It is, however, difficult to imagine that the increase of the disc emission and the decrease of the white dwarf emission just compensate each other. We also believe there is no DN that shows a steady decline of the V-magnitude (flux increase) during optical quiescence.

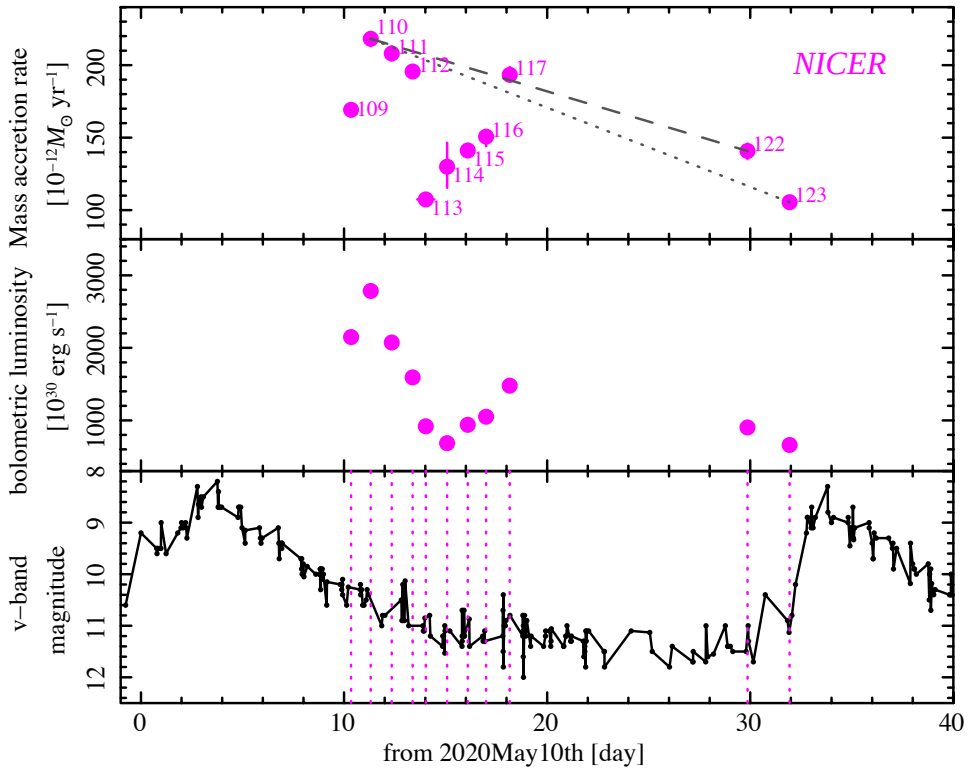

Fig. 7.11 Evolution of mass accretion rate and bolometric luminosity of SS Cyg observed by *NICER* as function of time since last outburst. Label number next to data point in top panel indicates last three digits of sequence number. Gray dotted and dashed lines are decrease rate of -2.5 % d^{-1} and -1.9 % d^{-1}, respectively. Dotted magenta line on bottom panel indicates times of *NICER* observations.

CHAPTER 8

Conclusion and Future Prospect

8.1 Conclusion

In this thesis, we have investigated the nature of the boundary layer that forms between the inner edge of the accretion disk and the white dwarf in order to understand the mass accretion process of dwarf novae. The temperature of the boundary layer in optical quiescence is 10^8 K and X-ray observation is suitable for this study. We have analyzed a series of dwarf novae data taken with *XMM-Newton*, *Suzaku* and *NICER*.

We have performed X-ray spectral analysis of *XMM-Newton* data for 19 quiescent dwarf novae. The observed spectra in the band 0.5–10 keV are moderately well represented by the multiple temperature thermal plasma emission models (the CEVMKL and VMCFLOW models in XSPEC) adding the reflection component of the plasma from the disk and white dwarf surface (the REFLECT model in XSPEC), and a fluorescent Fe emission line at 6.4 keV. With this updated X-ray spectral model and the reliable distance estimates to the observe DNe now available thanks to the *Gaia* Collaboration Data release 2 (Gaia Collaboration et al. 2018), the mass accretion rates at the boundary layer were obtained with an unprecedented accuracy, which cover the range from $1 \times 10^{-13} M_\odot$ yr^{-1} to $8 \times 10^{-11} M_\odot$ yr^{-1}. Owing to the high precision of the mass accretion rates, we confidently found that the mass accretion rate becomes smaller with decreasing orbital period. Quantitative analysis revealed that the observed accretion rate of the boundary layer in quiescence is about one order of magnitude smaller than that of the disk (§ 7.1.2). This reduction of the mass accretion rate is much more than that can be explained by the white dwarf rotation, and hence we need to invoke some other mechanism, such as the gas evaporation from the boundary layer (§ 7.3). In addition, we have measured the maximum plasma temperatures, which are in the range 5.7 to 20.6 keV. Thanks to these high precision measurements, we have found that the maximum temperature of the boundary layer shows a clear positive correlation with the white dwarf mass. They are approximately 40% of those predicted at the shock front in the radial free-fall flow on the white dwarf surface (§ 7.1.3).

In order to elucidate time evolution of the mass accretion rate of dwarf novae in the optically-quiescent phase, we have analyzed a series of VW Hyi data taken with *XMM-Newton* and *Suzaku*. From the evaluation of the spectra, we have derived the mass accretion rates. We plot the mass accretion rate against the elapsed time since the last outburst, and we have found a

systematic declining trend with a rate of -2.2 % d^{-1}. According to the standard disk instability model (e.g. Lasota (2001)), the mass accretion rate is predicted to increase throughout the quiescence phase. Therefore, we have performed the same evaluation using data from SS Cyg observed by *XMM-Newton*, *Suzaku*, and *NICER*. Consequently, the mass accretion rate of SS Cyg decreased by a rate of -2.6 to -1.2 % d^{-1}. The standard disk instability model may need to be modified.

8.2 Future prospect

After scrutinizing *XMM-Newton* data of DNe systematically, we found that the mass accretion rate through the boundary layer is much smaller than that in the optically thick accretion disk. The reason for this is still unclear. One possibility is outflow from the boundary layer, we obviously need observational evidence. For this to be done, we believe simultaneous observation with multiple wavelengths of V-band, EUV, and X-rays is preferable. As far as X-ray observations are concerned, the effect of the reflection component needs to be verified for each object. The reflection spectra produced have a broad "bump" structure centered at around 30 keV. On the other hand, the measurement energy range of *XMM-Newton* is limited to 0.1 - 15 keV. X-ray observations in higher energies up to, say $\sim$50 keV, is of essential importance in measuring the reflection component with higher precision. This will help enhancing reliability of the maximum temperature measurements. This will be able to be done with *NuSTAR* (Harrison et al. 2013) and *FORCE* (Mori et al. 2016) mission in the future. In order to investigate more detailed geometry of the boundary layer, it is necessary to increase the effective area while extending the measurable range to several tens of keV. We believe that an astronomical satellite that meets these requirements will be launched in the future.

REFERENCES

Allen, C. W. (1973), *Astrophysical quantities*.

Allen, C. W. (1976), *Astrophysical Quantities*.

Anders, E. and Grevesse, N. (1989), 'Abundances of the elements: Meteoritic and solar', Geochim. Cosmochim. Acta **53**(1), 197–214.

Arnaud, K. A. (1996), XSPEC: The First Ten Years, *in* G. H. Jacoby and J. Barnes, eds, 'Astronomical Data Analysis Software and Systems V', Vol. 101 of *Astronomical Society of the Pacific Conference Series*, p. 17.

Arnaud, M. and Raymond, J. (1992), 'Iron Ionization and Recombination Rates and Ionization Equilibrium', ApJ **398**, 394.

Arnaud, M. and Rothenflug, R. (1985), 'An updated evaluation of recombination and ionization rates.', AandAS **60**, 425–457.

Arzoumanian, Z., Gendreau, K. C., Baker, C. L., Cazeau, T., Hestnes, P., Kellogg, J. W., Kenyon, S. J., Kozon, R. P., Liu, K.-C., Manthripragada, S. S., Markwardt, C. B., Mitchell, A. L., Mitchell, J. W., Monroe, C. A., Okajima, T., Pollard, S. E., Powers, D. F., Savadkin, B. J., Winternitz, L. B., Chen, P. T., Wright, M. R., Foster, R., Prigozhin, G., Remillard, R. and Doty, J. (2014), The neutron star interior composition explorer (NICER): mission definition, *in* T. Takahashi, J.-W. A. den Herder and M. Bautz, eds, 'Space Telescopes and Instrumentation 2014: Ultraviolet to Gamma Ray', Vol. 9144, International Society for Optics and Photonics, SPIE, pp. 579 – 587.
URL: *https://doi.org/10.1117/12.2056811*

Baskill, D. S., Wheatley, P. J. and Osborne, J. P. (2005), 'The complete set of ASCA X-ray observations of non-magnetic cataclysmic variables', MNRAS **357**, 626–644.

Boldt, E. (1987), 'The cosmic X-ray background.', Phys. Rep. **146**(4), 215–257.

Bryans, P., Badnell, N. R., Gorczyca, T. W., Laming, J. M., Mitthumsiri, W. and Savin, D. W. (2006), 'Collisional Ionization Equilibrium for Optically Thin Plasmas. I. Updated Recombination Rate Coefficients for Bare through Sodium-like Ions', ApJS **167**(2), 343–356.

Byckling, K., Mukai, K., Thorstensen, J. R. and Osborne, J. P. (2010), 'Deriving an X-ray luminosity function of dwarf novae based on parallax measurements', MNRAS **408**(4), 2298–2311.

Cannizzo, J. K. (1993), 'The Accretion Disk Limit Cycle Model: Toward an Understanding of the Long-Term Behavior of SS Cygni', ApJ **419**, 318.

Cheng, F. H., Sion, E. M., Szkody, P. and Huang, M. (1997), 'Hubble Space Telescope Observations of the Dwarf Nova WZ Sagittae: A Very Rapidly Rotating White Dwarf', ApJ **484**(2), L149–L152.

Collins, D. J. and Wheatley, P. J. (2010), 'X-ray observations of SU UMa throughout six outbursts', MNRAS **402**, 1816–1823.

Cox, D. P. and Tucker, W. H. (1969), 'Ionization Equilibrium and Radiative Cooling of a Low-Density Plasma', ApJ **157**, 1157.

Dotani, T. and Suzaku Team (2008), Initial Results from the Suzaku Satellite, *in* 'The Eleventh Marcel Grossmann Meeting On Recent Developments in Theoretical and Experimental General Relativity, Gravitation and Relativistic Field Theories', pp. 1048–1050.

Duschl, W. J. and Tscharnuter, W. M. (1991), 'On the inner boundary condition of thin Keplerian accretion disks', AandA **241**(1), 153–158.

Eggleton, P. P. (1983), 'Aproximations to the radii of Roche lobes.', ApJ **268**, 368–369.

Fabian, A. C. (1994), 'Cooling Flows in Clusters of Galaxies', ARAandA **32**, 277–318.

Frank, J., King, A. and Raine, D. J. (2002), *Accretion Power in Astrophysics: Third Edition*.

Friend, M. T., Martin, J. S., Smith, R. C. and Jones, D. H. P. (1990), 'The 8190-A sodium doublet in cataclysmic variables III. Too cool for credibility.', MNRAS **246**, 654.

Gabriel, A. H. (1972), 'Dielectronic satellite spectra for highly-charged helium-like ionlines', MNRAS **160**, 99.

Gabriel, A. H. and Jordan, C. (1969), 'Long Wavelength Satellites to the He-like Ion Resonance Lines in the Laboratory and in the Sun', Nature **221**(5184), 947–949.

Gaetz, T. J. and Salpeter, E. E. (1983), 'Line radiation from a hot, optically thin plasma - Collision strengths and emissivities', ApJS **52**, 155–168.

Gaia Collaboration, Brown, A. G. A., Vallenari, A., Prusti, T., de Bruijne, J. H. J., Babusiaux, C., Bailer-Jones, C. A. L., Biermann, M., Evans, D. W., Eyer, L. and et al. (2018), 'Gaia Data Release 2. Summary of the contents and survey properties', AandA **616**, A1.

Gehrels, N. and Williams, E. D. (1993), 'Temperatures of Enhanced Stability in Hot Thin Plasmas', ApJ **418**, L25.

Gendreau, K. C., Arzoumanian, Z., Adkins, P. W., Albert, C. L., Anders, J. F., Aylward, A. T., Baker, C. L., Balsamo, E. R., Bamford, W. A., Benegalrao, S. S., Berry, D. L., Bhalwani, S., Black, J. K., Blaurock, C., Bronke, G. M., Brown, G. L., Budinoff, J. G., Cantwell, J. D., Cazeau, T., Chen, P. T., Clement, T. G., Colangelo, A. T., Coleman, J. S., Coopersmith, J. D., Dehaven, W. E., Doty, J. P., Egan, M. D., Enoto, T., Fan, T. W.-M., Ferro, D. M., Foster, R., Galassi, N. M., Gallo, L. D., Green, C. M., Grosh, D., Ha, K. Q., Hasouneh, M. A., Heefner, K. B., Hestnes, P., Hoge, L. J., Jacobs, T. M., Jørgensen, J. L., Kaiser, M. A., Kellogg, J. W., Kenyon, S. J., Koenecke, R. G., Kozon, R. P., LaMarr, B., Lambertson, M. D., Larson, A. M., Lentine, S., Lewis, J. H., Lilly, M. G., Liu, K. A., Malonis, A., Manthripragada, S. S., Markwardt, C. B., Matonak, B. D., Mcginnis, I. E., Miller, R. L., Mitchell, A. L., Mitchell, J. W., Mohammed, J. S., Monroe, C. A., de Garcia, K. M. M., Mul*é*, P. D., Nagao, L. T., Ngo, S. N., Norris, E. D., Norwood, D. A., Novotka, J., Okajima, T., Olsen, L. G., Onyeachu, C. O., Orosco, H. Y., Peterson, J. R., Pevear, K. N., Pham, K. K., Pollard, S. E., Pope, J. S., Powers, D. F., Powers, C. E., Price, S. R., Prigozhin, G. Y., Ramirez, J. B., Reid, W. J., Remillard, R. A., Rogstad, E. M., Rosecrans, G. P., Rowe, J. N., Sager, J. A., Sanders, C. A., Savadkin, B., Saylor, M. R., Schaeffer, A. F., Schweiss, N. S., Semper, S. R., Serlemitsos, P. J., Shackelford, L. V., Soong, Y., Struebel, J., Vezie, M. L., Villasenor, J. S., Winternitz, L. B., Wofford, G. I., Wright, M. R., Yang, M. Y. and Yu, W. H. (2016), The Neutron star Interior Composition Explorer (NICER): design and development, *in* J.-W. A. den Herder, T. Takahashi and M. Bautz, eds, 'Space Telescopes and Instrumentation 2016: Ultraviolet to Gamma Ray', Vol. 9905, International Society for Optics and Photonics, SPIE, pp. 420 – 435.
URL: *https://doi.org/10.1117/12.2231304*

George, I. M. and Fabian, A. C. (1991), 'X-ray reflection from cold matter in Active Galactic Nuclei and X-ray binaries.', MNRAS **249**, 352.

Godon, P., Seward, L., Sion, E. M. and Szkody, P. (2006), 'A Far-Ultraviolet Study of the Hot White Dwarf in the Dwarf Nova WW Ceti', AJ **131**(5), 2634–2642.

Godon, P., Sion, E. M., Barrett, P. E., Hubeny, I., Linnell, A. P. and Szkody, P. (2008), 'A Far Ultraviolet Archival Study of Cataclysmic Variables. I. FUSE and HST STIS Spectra of the Exposed White Dwarf in Dwarf Nova Systems', ApJ **679**(2), 1447–1466.

Gondoin, P., Aschenbach, B. R., Beijersbergen, M. W., Egger, R., Jansen, F. A., Stockman, Y. and Tock, J.-P. (1998*a*), Calibration of the first XMM flight mirror module: I. Image quality, *in* R. B. Hoover and A. B. Walker, eds, 'X-Ray Optics, Instruments, and Missions', Vol. 3444 of *Society of Photo-Optical Instrumentation Engineers (SPIE) Conference Series*, pp. 278–289.

Gondoin, P., Aschenbach, B. R., Beijersbergen, M. W., Egger, R., Jansen, F. A., Stockman, Y. and Tock, J.-P. (1998*b*), Calibration of the first XXM flight mirror module: II. Effective area, *in* R. B. Hoover and A. B. Walker, eds, 'X-Ray Optics, Instruments, and Missions', Vol. 3444 of *Society of Photo-Optical Instrumentation Engineers (SPIE) Conference Series*, pp. 290–301.

Gronenschild, E. H. B. M. and Mewe, R. (1978), 'Calculated X-radiation from optically thin plasmas. III. Abundance effects on continuum emission.', AandAS **32**, 283–305.

Hōshi, R. (1979), 'Accretion Model for Outbursts of Dwarf Nova', *Progress of Theoretical Physics* **61**, 1307–1319.

Hale, B. (2008), *Astrophysics processes : the physics of astronomical phenomena*, Cambridge University Press.
URL: *https://ci.nii.ac.jp/ncid/BA87192243*

Harrison, F. A., Craig, W. W., Christensen, F. E., Hailey, C. J., Zhang, W. W., Boggs, S. E., Stern, D., Cook, W. R., Forster, K., Giommi, P., Grefenstette, B. W., Kim, Y., Kitaguchi, T., Koglin, J. E., Madsen, K. K., Mao, P. H., Miyasaka, H., Mori, K., Perri, M., Pivovaroff, M. J., Puccetti, S., Rana, V. R., Westergaard, N. J., Willis, J., Zoglauer, A., An, H., Bachetti, M., Barrière, N. M., Bellm, E. C., Bhalerao, V., Brejnholt, N. F., Fuerst, F., Liebe, C. C., Markwardt, C. B., Nynka, M., Vogel, J. K., Walton, D. J., Wik, D. R., Alexander, D. M., Cominsky, L. R., Hornschemeier, A. E., Hornstrup, A., Kaspi, V. M., Madejski, G. M., Matt, G., Molendi, S., Smith, D. M., Tomsick, J. A., Ajello, M., Ballantyne, D. R., Baloković, M., Barret, D., Bauer, F. E., Blandford, R. D., Brandt, W. N., Brenneman, L. W., Chiang, J., Chakrabarty, D., Chenevez, J., Comastri, A., Dufour, F., Elvis, M., Fabian, A. C., Farrah, D., Fryer, C. L., Gotthelf, E. V., Grindlay, J. E., Helfand, D. J., Krivonos, R., Meier, D. L., Miller, J. M., Natalucci, L., Ogle, P., Ofek, E. O., Ptak, A., Reynolds, S. P., Rigby, J. R., Tagliaferri, G., Thorsett, S. E., Treister, E. and Urry, C. M. (2013), 'The Nuclear Spectroscopic Telescope Array (NuSTAR) High-energy X-Ray Mission', ApJ **770**(2), 103.

Hirose, M. and Osaki, Y. (1990), 'Hydrodynamic simulations of accretion disks in cataclysmic variables - Superhump phenomenon in SU UMa stars', PASJ **42**, 135–163.

Howell, S. B., Everett, M. E., Seebode, S. A., Szkody, P., Still, M., Wood, M., Ramsay, G., Cannizzo, J. and Smale, A. (2013), 'Spectroscopy of New and Poorly Known Cataclysmic Variables in the Kepler Field', AJ **145**(4), 109.

Ishida, M., Okada, S., Hayashi, T., Nakamura, R., Terada, Y., Mukai, K. and Hamaguchi, K. (2009), 'Suzaku Observations of SS Cygni in Quiescence and Outburst', PASJ **61**, S77–S91.

Ishida, M., Tsujimoto, M., Kohmura, T., Stuhlinger, M., Smith, M., Marshall, H. L., Guainazzi, M., Kawai, K. and Ogawa, T. (2011), 'Cross Spectral Calibration of Suzaku, XMM-Newton, and Chandra with PKS 2155-304 as an Activity of IACHEC', PASJ **63**, S657–S668.

Jansen, F., Lumb, D., Altieri, B., Clavel, J., Ehle, M., Erd, C., Gabriel, C., Guainazzi, M., Gondoin, P., Much, R., Munoz, R., Santos, M., Schartel, N., Texier, D. and Vacanti, G. (2001), 'XMM-Newton observatory. I. The spacecraft and operations', AandA **365**, L1–L6.

Jones, M. H. and Watson, M. G. (1992), 'The EXOSAT obseravtions of SS Cygni.', MNRAS **257**, 633–649.

Kaastra, J. S. (1992), 'An x-ray spectral code for optically thin plasma', *Internal SRON-Leiden Report* .
URL: *https://ci.nii.ac.jp/naid/10003942731/*

King, A. R. (1986), 'Accretion onto the white dwarf and X-ray production in nonmagnetic cataclysmic variables.', *Annals of the New York Academy of Sciences* **470**, 320–330.

King, A. R. and Shaviv, G. (1984), 'X-ray emission from non-magnetic cataclysmic variables', Nature **308**(5959), 519–521.

Kley, W. (1991), 'On the influence of the viscosity on the structure of the boundary layer of accretion disks.', AandA **247**, 95.

Koen, C. (1988), 'On the Hydrodynamics of Accretion Discs - Part One - an Examination of a Standard Boundary Condition', ApandSS **141**(2), 347–351.

Koyama, K., Tsunemi, H., Dotani, T., Bautz, M. W., Hayashida, K., Tsuru, T. G., Matsumoto, H., Ogawara, Y., Ricker, G. R., Doty, J., Kissel, S. E., Foster, R., Nakajima, H., Yamaguchi, H., Mori, H., Sakano, M., Hamaguchi, K., Nishiuchi, M., Miyata, E., Torii, K., Namiki, M., Katsuda, S., Matsuura, D., Miyauchi, T., Anabuki, N., Tawa, N., Ozaki, M., Murakami, H., Maeda, Y., Ichikawa, Y., Prigozhin, G. Y., Boughan, E. A., Lamarr, B., Miller, E. D., Burke, B. E., Gregory, J. A., Pillsbury, A., Bamba, A., Hiraga, J. S., Senda, A., Katayama, H., Kitamoto, S., Tsujimoto, M., Kohmura, T., Tsuboi, Y. and Awaki, H. (2007), 'X-Ray Imaging Spectrometer (XIS) on Board Suzaku', PASJ **59**, 23–33.

Kruszewski, A. (1966), 'Exchange of Matter and Period Changes in Close Binary Systems', *Advances in Astronomy and Astrophysics* **4**, 233–299.

Lasota, J.-P. (2001), 'The disc instability model of dwarf novae and low-mass X-ray binary transients', New A Rev. **45**, 449–508.

Liedahl, D. A., Osterheld, A. L. and Goldstein, W. H. (1995), 'New Calculations of Fe L-Shell X-Ray Spectra in High-Temperature Plasmas', ApJ **438**, L115.

Lightman, A. P. and White, T. R. (1988), 'Effects of Cold Matter in Active Galactic Nuclei: A Broad Hump in the X-Ray Spectra', ApJ **335**, 57.

Lubow, S. H. and Shu, F. H. (1975), 'Gas dynamics of semidetached binaries.', ApJ **198**, 383–405.

Magdziarz, P. and Zdziarski, A. A. (1995), 'Angle-dependent Compton reflection of X-rays and gamma-rays', MNRAS **273**, 837–848.

Masai, K. (1984), 'X-Ray Emission Spectra from Ionizing Plasmas', ApandSS **98**(2), 367–395.

Matt, G., Perola, G. C. and Piro, L. (1991), 'The iron line and high energy bump as X-ray signatures of cold matter in Seyfert 1 galaxies.', AandA **247**, 25.

Mazzotta, P., Mazzitelli, G., Colafrancesco, S. and Vittorio, N. (1998), 'Ionization balance for optically thin plasmas: Rate coefficients for all atoms and ions of the elements H to NI', AandAS **133**, 403–409.

McGowan, K. E., Priedhorsky, W. C. and Trudolyubov, S. P. (2004), 'On the Correlated X-Ray and Optical Evolution of SS Cygni', ApJ **601**, 1100–1108.

Menou, K., Hameury, J.-M., Lasota, J.-P. and Narayan, R. (2000), 'Disc instability models for X-ray transients: evidence for evaporation and low α-viscosity?', MNRAS **314**(3), 498–510.

Mewe, R., Gronenschild, E. H. B. M. and van den Oord, G. H. J. (1985), 'Calculated X-radiation from optically thin plasmas. V.', AandAS **62**, 197–254.

Mewe, R., Lemen, J. R. and van den Oord, G. H. J. (1986), 'Calculated X-radiation from optically thin plasmas. VI - Improved calculations for continuum emission and approximation formulae for nonrelativistic average Gaunt actors.', AandAS **65**, 511–536.

Meyer, F. and Meyer-Hofmeister, E. (1981), 'On the Elusive Cause of Cataclysmic Variable Outbursts', AandA **104**, L10.

Meyer, F. and Meyer-Hofmeister, E. (1994), 'Accretion disk evaporation by a coronal siphon flow.', AandA **288**, 175–182.

Mineshige, S. and Osaki, Y. (1985), 'Disk-instability model for outbursts of dwarf novae. II Full-disk calculations', PASJ **37**, 1–18.

Mitsuda, K., Bautz, M., Inoue, H., Kelley, R. L., Koyama, K., Kunieda, H., Makishima, K., Ogawara, Y., Petre, R., Takahashi, T., Tsunemi, H., White, N. E., Anabuki, N., Angelini, L., Arnaud, K., Awaki, H., Bamba, A., Boyce, K., Brown, G. V., Chan, K.-W., Cottam, J., Dotani, T., Doty, J., Ebisawa, K., Ezoe, Y., Fabian, A. C., Figueroa, E., Fujimoto, R., Fukazawa, Y., Furusho, T., Furuzawa, A., Gendreau, K., Griffiths, R. E., Haba, Y., Hamaguchi, K., Harrus, I., Hasinger, G., Hatsukade, I., Hayashida, K., Henry, P. J., Hiraga, J. S., Holt, S. S., Hornschemeier, A., Hughes, J. P., Hwang, U., Ishida, M., Ishisaki, Y., Isobe, N., Itoh, M., Iyomoto,

N., Kahn, S. M., Kamae, T., Katagiri, H., Kataoka, J., Katayama, H., Kawai, N., Kilbourne, C., Kinugasa, K., Kissel, S., Kitamoto, S., Kohama, M., Kohmura, T., Kokubun, M., Kotani, T., Kotoku, J., Kubota, A., Madejski, G. M., Maeda, Y., Makino, F., Markowitz, A., Matsumoto, C., Matsumoto, H., Matsuoka, M., Matsushita, K., McCammon, D., Mihara, T., Misaki, K., Miyata, E., Mizuno, T., Mori, K., Mori, H., Morii, M., Moseley, H., Mukai, K., Murakami, H., Murakami, T., Mushotzky, R., Nagase, F., Namiki, M., Negoro, H., Nakazawa, K., Nousek, J. A., Okajima, T., Ogasaka, Y., Ohashi, T., Oshima, T., Ota, N., Ozaki, M., Ozawa, H., Parmar, A. N., Pence, W. D., Porter, F. S., Reeves, J. N., Ricker, G. R., Sakurai, I., Sanders, W. T., Senda, A., Serlemitsos, P., Shibata, R., Soong, Y., Smith, R., Suzuki, M., Szymkowiak, A. E., Takahashi, H., Tamagawa, T., Tamura, K., Tamura, T., Tanaka, Y., Tashiro, M., Tawara, Y., Terada, Y., Terashima, Y., Tomida, H., Torii, K., Tsuboi, Y., Tsujimoto, M., Tsuru, T. G., Turner, M. J. L. ., Ueda, Y., Ueno, S., Ueno, M., Uno, S., Urata, Y., Watanabe, S., Yamamoto, N., Yamaoka, K., Yamasaki, N. Y., Yamashita, K., Yamauchi, M., Yamauchi, S., Yaqoob, T., Yonetoku, D. and Yoshida, A. (2007), 'The X-Ray Observatory Suzaku', PASJ **59**, S1–S7.

Mori, K., Tsuru, T. G., Nakazawa, K., Ueda, Y., Okajima, T., Murakami, H., Awaki, H., Matsumoto, H., Fukazawa, Y., Tsunemi, H., Takahashi, T. and Zhang, W. W. (2016), A broadband x-ray imaging spectroscopy with high-angular resolution: the FORCE mission, *in* J.-W. A. den Herder, T. Takahashi and M. Bautz, eds, 'Space Telescopes and Instrumentation 2016: Ultraviolet to Gamma Ray', Vol. 9905 of *Society of Photo-Optical Instrumentation Engineers (SPIE) Conference Series*, p. 99051O.

Mukai, K., Zietsman, E. and Still, M. (2009), 'Suzaku Observations of the Dwarf Nova V893 Scorpii: The Discovery of a Partial X-ray Eclipse', ApJ **707**(1), 652–661.

Mushotzky, R. F. and Szymkowiak, A. E. (1988), Einstein Observatory solid state detector observations of cooling flows in clusters of galaxies, *in* A. C. Fabian, ed., 'NATO Advanced Science Institutes (ASI) Series C', Vol. 229 of *NATO Advanced Science Institutes (ASI) Series C*, pp. 53–62.

Nakaniwa, N., Hayashi, T., Takeo, M. and Ishida, M. (2019), 'Variation of mass accretion rate on to the white dwarf in the dwarf nova VW Hyi in quiescence', MNRAS **488**(4), 5104–5113.

Narayan, R. and Popham, R. (1993), 'Hard X-rays from accretion disk boundary layers', Nature **362**(6423), 820–822.

Nauenberg, M. (1972), 'Analytic Approximations to the Mass-Radius Relation and Energy of Zero-Temperature Stars', ApJ **175**, 417.

Okajima, T., Soong, Y., Balsamo, E. R., Enoto, T., Olsen, L., Koenecke, R., Lozipone, L., Kearney, J., Fitzsimmons, S., Numata, A., Kenyon, S. J., Arzoumanian, Z. and Gendreau, K. (2016), Performance of NICER flight x-ray concentrator, *in* J.-W. A. den Herder, T. Takahashi

and M. Bautz, eds, 'Space Telescopes and Instrumentation 2016: Ultraviolet to Gamma Ray', Vol. 9905 of *Society of Photo-Optical Instrumentation Engineers (SPIE) Conference Series*, p. 99054X.

Osaki, Y. (1974), 'An accretion model for the outbursts of U Geminorum stars', PASJ **26**, 429–436.

Osaki, Y. (1989), 'A model for the superoutburst phenomenon of SU Ursae Majoris stars', PASJ **41**, 1005–1033.

Osaki, Y. (1996), 'Dwarf-Nova Outbursts', PASP **108**, 39.

Osaki, Y. (2005), 'The disk instability model for dwarf nova outbursts', *Proceeding of the Japan Academy, Series B* **81**, 291–305.

Pandel, D., Córdova, F. A., Mason, K. O. and Priedhorsky, W. C. (2005), 'X-Ray Observations of the Boundary Layer in Dwarf Novae at Low Accretion Rates', ApJ **626**, 396–410.

Patterson, J. (1984), 'The evolution of cataclysmic and low-mass X-ray binaries.', ApJS **54**, 443–493.

Polidan, R. S., Mauche, C. W. and Wade, R. A. (1990), 'A study of extreme-ultraviolet emission from cataclysmic variables', ApJ **356**, 211–222.

Porquet, D., Mewe, R., Dubau, J., Raassen, A. J. J. and Kaastra, J. S. (2001), 'Line ratios for helium-like ions: Applications to collision-dominated plasmas', AandA **376**, 1113–1122.

Prigozhin, G., Gendreau, K., Foster, R., Ricker, G., Villaseñor, J., Doty, J., Kenyon, S., Arzoumanian, Z., Redus, R. and Huber, A. (2012), Characterization of the silicon drift detector for NICER instrument, *in* A. D. Holland and J. W. Beletic, eds, 'High Energy, Optical, and Infrared Detectors for Astronomy V', Vol. 8453 of *Society of Photo-Optical Instrumentation Engineers (SPIE) Conference Series*, p. 845318.

Pringle, J. E. (1977), 'Soft X-ray emission from dwarf novae.', MNRAS **178**, 195–202.

Pringle, J. E. (1981), 'Accretion discs in astrophysics', ARAandA **19**, 137–162.

Pringle, J. E. J. E. and Wade, R. A. R. A. (1985), *Interacting binary stars*, number 6 *in* 'Cambridge astrophysics series', Cambridge University Press.
URL: *https://ci.nii.ac.jp/ncid/BA01317312*

Pringle, J. E. and Savonije, G. J. (1979), 'X-ray emission from dwarf novae.', MNRAS **187**, 777–783.

Raymond, J. C., Cox, D. P. and Smith, B. W. (1976), 'Radiative cooling of a low-density plasma.', ApJ **204**, 290–292.

Raymond, J. C. and Smith, B. W. (1977), 'Soft X-ray spectrum of a hot plasma.', ApJS **35**, 419–439.

Ritter, H. and Kolb, U. (2003), 'Catalogue of cataclysmic binaries, low-mass X-ray binaries and related objects (Seventh edition)', AandA **404**, 301–303.

Schoembs, R. and Vogt, N. (1981), 'High-time resolution spectroscopy of VW Hydri and WX Hydri', AandA **97**, 185–191.

Serlemitsos, P. J., Soong, Y., Chan, K.-W., Okajima, T., Lehan, J. P., Maeda, Y., Itoh, K., Mori, H., Iizuka, R., Itoh, A., Inoue, H., Okada, S., Yokoyama, Y., Itoh, Y., Ebara, M., Nakamura, R., Suzuki, K., Ishida, M., Hayakawa, A., Inoue, C., Okuma, S., Kubota, R., Suzuki, M., Osawa, T., Yamashita, K., Kunieda, H., Tawara, Y., Ogasaka, Y., Furuzawa, A., Tamura, K., Shibata, R., Haba, Y., Naitou, M. and Misaki, K. (2007), 'The X-Ray Telescope onboard Suzaku', PASJ **59**, S9–S21.

Shakura, N. I. and Sunyaev, R. A. (1973), 'Reprint of 1973AandA....24..337S. Black holes in binary systems. Observational appearance.', AandA **500**, 33–51.

Sion, E. M., Cheng, F. H., Szkody, P., Sparks, W., Gänsicke, B., Huang, M. and Mattei, J. (1998), 'Anomalous Cooling of the Massive White Dwarf in U Geminorum Following a Narrow Dwarf Nova Outburst', ApJ **496**(1), 449–453.

Sion, E. M., Godon, P., Myzcka, J. and Blair, W. P. (2010), 'The Accreting White Dwarf in SS Cygni Revealed', ApJ **716**(2), L157–L160.

Smak, J. (1984*a*), 'Accretion in cataclysmic binaries. IV. Accretion disks in dwarf novae.', Acta Astron. **34**, 161–189.

Smak, J. (1984*b*), 'Eruptive binaries. XI. Disk-radius variations un U Gem.', Acta Astron. **34**, 93–96.

Smak, J. (1984*c*), 'Outbursts of dwarf novae.', PASP **96**, 5–18.

Smak, J. (1992), 'Structure of Accretion Disks and the Visibility of White Dwarfs in Cataclysmic Binaries', Acta Astron. **42**, 323–333.

Smak, J. (1993), 'WZ SGE as a Dwarf Nova', Acta Astron. **43**, 101–119.

SOC, E. X.-N. (2020), 'XMM-Newton Users Handbook: Issue 2.18'.

Strüder, L., Briel, U., Dennerl, K., Hartmann, R., Kendziorra, E., Meidinger, N., Pfeffermann, E., Reppin, C., Aschenbach, B., Bornemann, W., Bräuninger, H., Burkert, W., Elender, M., Freyberg, M., Haberl, F., Hartner, G., Heuschmann, F., Hippmann, H., Kastelic, E., Kemmer, S., Kettenring, G., Kink, W., Krause, N., Müller, S., Oppitz, A., Pietsch, W., Popp, M., Predehl,

P., Read, A., Stephan, K. H., Stötter, D., Trümper, J., Holl, P., Kemmer, J., Soltau, H., Stötter, R., Weber, U., Weichert, U., von Zanthier, C., Carathanassis, D., Lutz, G., Richter, R. H., Solc, P., Böttcher, H., Kuster, M., Staubert, R., Abbey, A., Holland, A., Turner, M., Balasini, M., Bignami, G. F., La Palombara, N., Villa, G., Buttler, W., Gianini, F., Lainé, R., Lumb, D. and Dhez, P. (2001), 'The European Photon Imaging Camera on XMM-Newton: The pn-CCD camera', AandA **365**, L18–L26.

Summers, H. P. and McWhirter, R. W. P. (1979), 'Radiative power loss from laboratory and astrophysical plasmas. I. Power loss from plasmas in steady-state ionisation balance', *Journal of Physics B Atomic Molecular Physics* **12**(14), 2387–2412.

Takahashi, T., Abe, K., Endo, M., Endo, Y., Ezoe, Y., Fukazawa, Y., Hamaya, M., Hirakuri, S., Hong, S., Horii, M., Inoue, H., Isobe, N., Itoh, T., Iyomoto, N., Kamae, T., Kasama, D., Kataoka, J., Kato, H., Kawaharada, M., Kawano, N., Kawashima, K., Kawasoe, S., Kishishita, T., Kitaguchi, T., Kobayashi, Y., Kokubun, M., Kotoku, J., Kouda, M., Kubota, A., Kuroda, Y., Madejski, G., Makishima, K., Masukawa, K., Matsumoto, Y., Mitani, T., Miyawaki, R., Mizuno, T., Mori, K., Mori, M., Murashima, M., Murakami, T., Nakazawa, K., Niko, H., Nomachi, M., Okada, Y., Ohno, M., Oonuki, K., Ota, N., Ozawa, H., Sato, G., Shinoda, S., Sugiho, M., Suzuki, M., Taguchi, K., Takahashi, H., Takahashi, I., Takeda, S., Tamura, K.-I., Tamura, T., Tanaka, T., Tanihata, C., Tashiro, M., Terada, Y., Tominaga, S., Uchiyama, Y., Watanabe, S., Yamaoka, K., Yanagida, T. and Yonetoku, D. (2007), 'Hard X-Ray Detector (HXD) on Board Suzaku', PASJ **59**, 35–51.

Tsujimoto, M., Guainazzi, M., Plucinsky, P. P., Beardmore, A. P., Ishida, M., Natalucci, L., Posson-Brown, J. L. L., Read, A. M., Saxton, R. D. and Shaposhnikov, N. V. (2011), 'Cross-calibration of the X-ray instruments onboard the Chandra, INTEGRAL, RXTE, Suzaku, Swift, and XMM-Newton observatories using G21.5-0.9', AandA **525**, A25.

Tucker, W. H. and Koren, M. (1971), 'Erratum: Radiation from a High-Temperature Low-Density Plasma: the X-Ray Spectrum of the Solar Corona', ApJ **170**, 621.

Turner, M. J. L., Abbey, A., Arnaud, M., Balasini, M., Barbera, M., Belsole, E., Bennie, P. J., Bernard, J. P., Bignami, G. F., Boer, M., Briel, U., Butler, I., Cara, C., Chabaud, C., Cole, R., Collura, A., Conte, M., Cros, A., Denby, M., Dhez, P., Di Coco, G., Dowson, J., Ferrando, P., Ghizzardi, S., Gianotti, F., Goodall, C. V., Gretton, L., Griffiths, R. G., Hainaut, O., Hochedez, J. F., Holland, A. D., Jourdain, E., Kendziorra, E., Lagostina, A., Laine, R., La Palombara, N., Lortholary, M., Lumb, D., Marty, P., Molendi, S., Pigot, C., Poindron, E., Pounds, K. A., Reeves, J. N., Reppin, C., Rothenflug, R., Salvetat, P., Sauvageot, J. L., Schmitt, D., Sembay, S., Short, A. D. T., Spragg, J., Stephen, J., Strüder, L., Tiengo, A., Trifoglio, M., Trümper, J., Vercellone, S., Vigroux, L., Villa, G., Ward, M. J., Whitehead, S. and Zonca, E. (2001), 'The European Photon Imaging Camera on XMM-Newton: The MOS cameras', AandA **365**, L27–L35.

Tylenda, R. (1981), 'Radiation from Optically Thin Accretion Discs', Acta Astron. **31**, 127.

Urban, J. A. and Sion, E. M. (2006), 'The Dwarf Novae during Quiescence', ApJ **642**(2), 1029–1041.

Verbunt, F. (1982), 'Accretion Disks in Stellar X-Ray Sources', Space Sci. Rev. **32**(4), 379–404.

Wada, Q., Tsujimoto, M., Ebisawa, K. and Hayashi, T. (2017), 'A systematic X-ray study of the dwarf novae observed with Suzaku', PASJ **69**, 10.

Warner, B. (1987), 'Absolute magnitudes of cataclysmic variables.', MNRAS **227**, 23–73.

Warner, B. (2003), *Cataclysmic Variable Stars*.

Wheatley, P. J., Mauche, C. W. and Mattei, J. A. (2003), 'The X-ray and extreme-ultraviolet flux evolution of SS Cygni throughout outburst', MNRAS **345**, 49–61.

Wheatley, P. J., Verbunt, F., Belloni, T., Watson, M. G., Naylor, T., Ishida, M., Duck, S. R. and Pfeffermann, E. (1996), 'The X-ray and EUV spectrum of the dwarf nova VW Hydri in outburst and quiescence.', AandA **307**, 137.

Whitehurst, R. (1988), 'Numerical simulations of accretion disks. I - Superhumps - A tidal phenomenon of accretion disks', MNRAS **232**, 35–51.

Wilms, J., Allen, A. and McCray, R. (2000), 'On the Absorption of X-Rays in the Interstellar Medium', ApJ **542**(2), 914–924.

Wolter, H. (1952), 'Spiegelsysteme streifenden Einfalls als abbildende Optiken für Röntgenstrahlen', *Annalen der Physik* **445**(1), 94–114.

Wood, J. H., Horne, K., Berriman, G. and Wade, R. A. (1989), 'Eclipse Studies of the Dwarf Nova OY Carinae in Quiescence', ApJ **341**, 974.

野本, 憲., 定金, 晃. and 佐藤, 勝. (2009), 恒星, number 7 *in* 'シリーズ現代の天文学', 日本評論社.
URL: *https://ci.nii.ac.jp/ncid/BA90711972*

ACKNOWLEDGEMENT

First of all, I would like to express my deepest gratitude to Prof. Manabu Ishida (ISAS / JAXA) who has guided me through my graduate course. He gave me a opportunity to study on the dwarf novae and the X-ray mirror. Also, I am grateful to Takayuki Hayashi (NASA / GSFC) for teaching me the method of astronomical analysis. And I would like to thank Yoshitomo Maeda (ISAS / JAXA), Ryo Iizuka and Toshiki Sato for their help and advice on my research. I feel very privileged to have spent my days studying astrophysics in the Ishida group at ISAS/JAXA.

I am grateful to Yoshitaka Ishisaki (Tokyo Metropolitan University : TMU), Yuichiro Ezoe and Prof. Yutaka Fujita for helpful discussions and suggestions in preparing this thesis. I would like to thank Shinya Yamada (Rikkyo University), Teruaki Enoto (RIKEN) and Mariko Kimura for giving me the opportunity to analyze the *NICER* data. Also, I would like to thank all my seniors and juniors in the Experimental Astrophysics Group and Theoretical Astrophysics Group in TMU. I want to name and express my gratitude to each and every one of them who overcame various problems together, and the days I spent with these colleagues are invaluable to me. And above all, I am very grateful to Prof. Takaya Ohashi and Prof. Kuniaki Masai who helped me a lot during my graduate course as a student at TMU.

Finally, I appreciate my parents for their understanding of my research and for supporting me without any inconvenience. I think that the things that I have now is thanks to my parents.